

TABLE OF CONTENTS

	Page
INTRODUCTION	1
CHAPTER 1 GENERAL CONCEPTS AND LITTERATURE REVIEW	5
1.1 The biomechanics of the femur at the hip joint	5
1.1.1 Anatomy.....	5
1.1.2 Forces.....	7
1.1.3 Mechanical properties.....	8
1.1.3.1 Elastic modulus.....	10
1.1.3.2 Strength.....	10
1.1.3.3 Interfacial strength	10
1.2 Total hip arthroplasty	11
1.2.1 Epidemiology and future perspectives.....	13
1.2.2 Main related problems	14
1.3 Numerical analysis of hip implants.....	15
1.3.1 Mechanical causes of implant failure	15
1.3.1.1 Stress shielding	15
1.3.1.2 Interfacial failure.....	17
1.3.2 Improvement of stem performance.....	18
1.3.2.1 Optimization of implant shape.....	18
1.3.2.2 Functionally graded stems	20
1.4 Porous materials.....	22
1.4.1 Well-ordered porous materials.....	23
1.4.2 Main geometrical parameters of porous materials.....	24
1.4.3 Additive manufacturing of porous materials	25
1.4.3.1 Irregularities of additively manufactured porous materials.....	27
1.4.3.1.1 Contribution related to this thesis	28
1.4.4 Mechanical properties of porous materials.....	28
1.4.4.1 Experimental testing of porous materials	29
1.4.4.2 Numerical modeling.....	32
1.4.4.2.1 Effect of manufacturing irregularities.....	35
1.5 Summary.....	36
CHAPTER 2 HYPOTHESIS, OBJECTIVES AND STRUCTURE OF THE THESIS.....	37
2.1 Problem statement.....	37
2.2 Hypothesis and objectives.....	38
CHAPTER 3 ARTICLE 1. FINITE ELEMENT MODELLING APPROACHES FOR WELL-ORDERED POROUS METALLIC MATERIALS FOR ORTHOPAEDIC APPLICATIONS: COST EFFECTIVENESS AND GEOMETRICAL CONSIDERATIONS.....	43
3.1 Abstract.....	43
3.2 Introduction.....	44

3.3	Materials and Methods.....	46
3.3.1	Geometrical parameters at mesoscale.....	47
3.3.2	Finite element (FE) modelling approaches.....	48
3.3.2.1	Finite size solid FE model.....	49
3.3.2.2	Finite size beam FE model.....	50
3.3.2.3	Infinite media model.....	51
3.3.3	Performed FE analyses.....	52
3.3.3.1	Determination of the cost-effective model approach.....	52
3.3.3.2	Unit cell geometry comparison: cubic and diamond.....	53
3.3.3.3	Criteria 1: similar bending and compressive behaviours.....	53
3.3.3.4	Criteria 2: mechanical properties close to bone.....	54
3.3.3.5	Criteria 3: Stress distribution uniformity within struts.....	54
3.4	Results.....	54
3.4.1	Determination of the cost-effective model approach.....	54
3.4.2	Unit cell geometry comparison: cubic and diamond.....	57
3.4.2.1	Criteria 1: similar bending and compressive behaviours.....	57
3.4.2.2	Criteria 2: mechanical properties close to bone.....	58
3.4.2.3	Criteria 3: stress distribution uniformity within struts.....	59
3.5	Discussion.....	60
3.6	Conclusion.....	62
3.7	Acknowledgements.....	63

CHAPTER 4 ARTICLE 2. FINITE ELEMENT MODELING OF MANUFACTURING IRREGULARITIES OF POROUS MATERIALS.....		65
4.1	Abstract.....	65
4.2	Introduction.....	66
4.3	Materials and Methods.....	68
4.3.1	Experimental data.....	68
4.3.2	FE modeling.....	69
4.3.3	Characterization and implementation of manufacturing irregularities in the FE model.....	71
4.3.3.1	Strut diameter variation.....	71
4.3.3.2	Strut inclination.....	72
4.3.3.3	Fractured struts.....	73
4.3.4	Finite Element Analyses.....	73
4.4	Results.....	74
4.4.1	Characterization of manufacturing irregularities.....	74
4.4.2	Finite element analyses.....	75
4.4.3	Influence of the three geometrical irregularities for set S450P700.....	75
4.4.4	Simulation of the other sample sets.....	78
4.5	Discussion.....	80
4.6	Conclusions.....	82
4.7	Acknowledgements.....	82

CHAPTER 5	ARTICLE 3. NUMERICAL DESIGN OF HIP STEMS WITH OPTIMIZED SHAPE AND FUNCTIONALLY GRADED MATERIAL PROPERTIES BY MEANS OF ADDITIVE MANUFACTURED POROUS MATERIALS	83
5.1	Abstract.....	83
5.2	Introduction.....	84
5.3	Materials and Methods.....	86
5.3.1	Optimization strategy.....	86
5.3.1.1	Stem optimization at the macroscale	87
5.3.1.2	Porous material tailoring at the mesoscale.....	90
5.3.2	Finite element modeling	91
5.3.2.1	Stem and bone at the macroscale	91
5.3.2.2	Porous material at the mesoscale	92
5.4	Results.....	93
5.5	Discussion.....	97
5.6	Conclusion	100
5.7	Acknowledgements.....	100
CHAPTER 6	GENERAL DISCUSSION.....	101
6.1	Synthesis of the articles	102
6.2	Limitations	103
6.2.1	Limitations related to the porous material model	103
6.2.1.1	Unit cell geometry.....	103
6.2.1.2	Beam model	104
6.2.1.3	Manufacturing irregularities	105
6.2.2	Limitations related to the optimization of the hip stem	105
6.2.2.1	Dimensionality of the bone-implant model	106
6.2.2.2	Interfacial conditions	106
6.2.2.3	Evaluation of implant performance	107
6.2.2.4	Tailoring of the porous material	107
6.3	Future work.....	108
CONCLUSION	111
APPENDIX I	EXPERIMENTAL TESTS OF POROUS MATERIALS	113
APPENDIX II	BRENT'S METHOD FOR ROOT FINDING	115
APPENDIX III	NSGA-II GENETIC ALGORITHM, SIMULATED BINARY CROSSOVER AND POLYNOMIAL MUTATION	117
AIII.1	The evolution process	118
AIII.2	Tournament selection.....	119
AIII.3	Genetic operators	119
AIII.3.1	Simulated binary crossover	119
AIII.3.2	Polynomial mutation	120

LIST OF REFERENCES123

LIST OF TABLES

	Page
Table 1.1 Muscle forces (in % of the bodyweight) and their representation for stair climbing.....	8
Table 1.2 Differences between EBM and DSLM technologies.....	27
Table 1.3 Relationship between the elastic modulus and the relative density for different unit cells. Analytical relationships are indicated by *.....	32
Table 3.1 Performed analyses.....	46
Table 3.2 Geometrical parameters at the mesoscale used in the FE analyses.	52
Table 3.3 Comparison between $E_{ap,comp}$ and $E_{ap,bend}$ for the two unit cell geometries and different S_R using $n_p=8$	58
Table 3.4 Comparison of v_{ap} for the two unit cell geometries and different S_R using $n_p=8$	59
Table 4.1 Design and experimental strut and pore sizes.....	69
Table 4.2 Measured strut inclination ($Sinc$) and fractured struts (Sfr) manufacturing irregularities of non-tested sample S450P700.....	74
Table 5.1 Initial, minimum and maximum values for the 8 shape variables.....	89
Table 5.2 Values for the distributions of manufacturing irregularities.....	92
Table AI.1 Mechanical properties of experimental testing of porous materials	113

LIST OF FIGURES

	Page
Figure 0.1 General schema of the thesis	3
Figure 1.1 The femur.	6
Figure 1.2 (a) The hip joint and its movements (adapted from (Tortora 2012)); (b) reference system of the femur	7
Figure 1.3 Cortical and cancellous bone.....	9
Figure 1.4 Total hip replacement components.....	12
Figure 1.5 (a) Anatomical, (b) cylindrical and (c) tapered cementless stems. The hatched represents the porous coated zone for bone ingrowth.	13
Figure 1.6 Causes for revision of the arthroplasty in Canada.....	15
Figure 1.7 Interfacial failure index for (a) solid titanium and (b) flexible stems.	17
Figure 1.8 (a) Bone density after remodeling and (b) interfacial failure around a stem with optimized shape.....	19
Figure 1.9 (a) Porous material density distribution; (b) bone resorption; (c) interfacial shear stresses for a functionally graded hip stem; (d) bone resorption; (e) interfacial shear stresses for a solid Ti6Al4V stem. Adapted from Arabnejad Khanoki and Pasini (2013c)	21
Figure 1.10 Macroscale, mesoscale and microscale of a porous material	23
Figure 1.11 (a) Simple cubic and (b) diamond unit cells.....	24
Figure 1.12 The process of additive manufacturing. Taken from (Heinl, et al. 2008)	26
Figure 1.13 Computation of apparent mechanical behavior from the results of an experimental compression test. Apparent linear zone stands in red	29
Figure 1.14 Reported values of E_{ap} of Ti6Al4V porous materials	30
Figure 1.15 Reported values of $S_{Y,ap}$ and S_{MAX} of Ti6Al4V porous materials	31
Figure 1.16 Simple cubic unit cell: (a) continuum model (solid FE elements); (b) 3-node beam model (1 element per strut).....	33

Figure 3.1 Cubic (a) and diamond (b) unit cell geometries showing main parameters	47
Figure 3.2 Symmetry surfaces and loading application of the solid FE model	50
Figure 3.3 Periodic boundary conditions used for the 3D Infinite media approach	51
Figure 3.4 $E_{ap,comp}$ as a function of n_p (from 2 to 10) for the cubic unit cell geometry using the solid, beam and infinite media FE models ($\phi_S = 450 \mu\text{m}$)	55
Figure 3.5 $ \Delta E_{ap,comp} $ as a function of Δn_p (variation of $E_{ap,comp}$ for n_p	56
Figure 3.6 $\varepsilon\%$ (difference in $E_{ap,comp}$ as between solid and beam FE models) a function of S_R ($\phi_S = 450 \mu\text{m}$) for $n_p = 8$	57
Figure 3.7 (a) Stress distribution within the struts for the cubic unit cell geometry; and (b) diamond unit cell geometry; (c) pure compression zones (in red) for the cubic unit cell geometry; (d) pure compression (in red) and (e) pure traction zones (in green), respectively, for the diamond unit cell geometry	60
Figure 4.1 (a) Cubic unit-cell pore geometry and main parameters and (b) 10-pore sample model generated by periodic repetitions of the unit-cell	68
Figure 4.2 Different types of geometrical manufacturing irregularities: strut diameter variation (solid points), strut inclination (straight lines) and fractured struts (empty circles)	70
Figure 4.3 Schematization of the strut diameter variation	71
Figure 4.4 Conversion of diameter value to section number	72
Figure 4.5 Conversion of the inclination angle θ to keypoint shifting distance	73
Figure 4.6 Apparent stress-compressive strain ($\sigma_{ap}-\varepsilon$) curves for the set S450P700 obtained with the idealized model, the different combinations of manufacturing irregularities, and the experimental tests. <i>Dvar</i> : diameter variation; <i>Sfr</i> : fractured struts; <i>Sinc</i> : inclined struts; Exp: experimental	76
Figure 4.7 E_{ap} and $S_{Y,ap}$ obtained with the idealized model, the different combinations of manufacturing irregularities, and the experimental tests for the set S450P700. <i>Dvar</i> : diameter variation; <i>Sfr</i> : fractured struts; <i>Sinc</i> : inclined struts; Exp: experimental	78

Figure 4.8 Comparison of $S_{Y,ap}$ (plain bars) and E_{ap} (hatched bars) obtained from experimental tests (Exp) and from FE simulations including the three manufacturing irregularities (Sim) for the three sets (S450P600, S450P700 and S450P800)	79
Figure 5.1 General schema for the functionally graded stem optimization.....	86
Figure 5.2 Geometrical variables (h_j) for the stem shape and grid (red dots) for the optimization of material properties. The angles $\alpha_1=29.79^\circ$, $\alpha_2=15.8^\circ$, $\alpha_3=4.88^\circ$ have fixed values.....	88
Figure 5.3 Meshing and loading of the stem and bone model	91
Figure 5.4 Porous material model at the mesoscale: a - idealized; b - with manufacturing irregularities. Beam elements have been thickened to show the ϕ_S variation ..	93
Figure 5.5 590 optimized stems after 50 generations (30090 function evaluations). Diamond markers: first non-dominated front. The different plots show the influence of bone resorption, stem size, stiffness and length in the interfacial failure index (F_{IS}) and bone loss index (F_{BL}). Representative selected stem designs b-e are circled.....	94
Figure 5.6 Distribution of resorbed bone (grey) and non-resorbed bone (black) and interfacial shear stresses (in MPa) for a) the original stem design; b)-e) the selected (optimized) stem designs of Figure 5.5. The color maps represent the strut thickness (ϕ_S in mm) and the corresponding apparent elastic modulus (E_{ap} , in GPa) as computed in the porous material tailoring at the mesoscale step.....	96
Figure 5.7 Differences (in %) between E_{ap} and the prescribed E for the selected stem designs b – e of Figure 5.5.	97
Figure AII.1 Sorting of the current population and creation of the parent population for the next generation in NSGA-II.	118

LIST OF ACRONYMS

2D	Two dimensions
3D	Three dimensions
ANOVA	Analysis of variance
BCC	Body centered cubic unit cell
Bend	Bending
CAD	Computer aided design
CoCrMo	Cobalt-Chrome-Molybdenum alloy
Comp	Compression
D	Diamond unit cell
<i>dir1, dir2</i>	Direction 1, 2
DO	Dodecahedron unit cell
DMLS	Direct metal laser sintering
DT	Dode-thin unit cell
<i>Dvar</i>	Strut diameter variation
EBM	Electron Beam Melting
Exp	Experimental value for the mechanical behavior of the porous material
FE	Finite element
FEA	Finite element analysis
FG	Functionally graded
gen	Generation of the genetic algorithm
GY	Gyroid unit cell

IBV	Biomechanic's Institute of Valence (Instituto de Biomecánica de Valencia), Spain
MP	Material properties
NSERC	Natural Sciences and Engineering Research Council of Canada
NSGA-II	Non-dominated sorted genetic algorithm II
PM	Polynomial mutation
OA	Osteoarthritis
RMSD	Root mean square difference
SC	Simple cubic unit cell
SBX	Simulated binary crossover
<i>Sfr</i>	Fractured struts
Sim	Simulated value for the mechanical behavior of the porous material
<i>Sinc</i>	Strut inclination
SLM	Selective laser melting
THA	Total hip arthroplasty
Ti6Al4V	Titanium-6-Aluminium-4-Vanadium alloy

LIST OF SYMBOLS

A	Area of the cross-section of the strut (μm^2)
A_{stem}	Interfacial area of the stem (mm^2)
C_I	Constant relating the apparent elastic modulus to the density of the porous material
dA_{stem}	Differential of stem interfacial area
dV_{bone}	Differential of bone volume
E	Elastic modulus (GPa)
E_{ap}	Apparent elastic modulus of the porous material (GPa)
$E_{ap,beam}$	Apparent elastic modulus of the beam model (GPa)
$E_{ap,bend}$	Apparent elastic modulus in bending of the porous material (GPa)
E_{canc}	Elastic modulus of the cancellous bone (GPa)
$E_{ap,comp}$	Apparent elastic modulus in compression of the porous material (GPa)
$\Delta E_{ap,comp}$	Variation in $E_{ap,comp}$ for a 1 pore increase in the sample size (GPa)
$E_{ap,dir1}$	Apparent elastic modulus of the porous material in direction 1 (GPa)
$E_{ap,dir2}$	Apparent elastic modulus of the porous material in direction 2 (GPa)
$E_{ap,solid}$	Apparent elastic modulus of the solid (continuum) model (GPa)
E_{cort}	Elastic modulus of the cortical bone (GPa)
E_i	Elastic modulus the stem material optimization point i (GPa)
E_{max}	Maximum elastic modulus for the stem material optimization (GPa)
E_{min}	Minimum elastic modulus for the stem material optimization (GPa)
E_S	Elastic modulus of the solid phase of the porous material (GPa)
F	Force (N)

F_{abd}	Abductor muscle force (N)
F_{BL}	Function of the bone loss (N)
F_{cont}	Hip contact force (N)
f_{IS}	Local interfacial failure index
F_{IS}	Global interfacial failure index
F_{vl}	Vastus lateralis muscle force (N)
F_{vm}	Vastus medialis muscle force (N)
G	Shear modulus (GPa)
$g(S_{en})$	Bone resorption function
h_j	Shape variable j of the stem (mm)
$h_{j,max}$	Maximum value of the shape variable j of the stem (mm)
$h_{j,min}$	Minimum value of the shape variable j of the stem (mm)
I	Counter
I	Inertia of the cross-section of the strut (μm^4)
I_{ap}	Apparent inertia of the porous material (μm^4)
K	Tangent modulus (GPa)
K_i, K'_i	Keypoint
L	Length of the strut (μm)
L_{cell}, L_{UC}	Length of the unit cell ($\mu\text{m}, \text{mm}$)
$L_{cell,cubic}$	Length of the simple cubic unit cell (μm)
$L_{cell,diamond}$	Length of the diamond unit cell (μm)
L_{sample}	Porous material sample length (mm)
M	Total bone mass (mg)

$m_{loss,stem}$	Bone loss (resected) due to the stem insertion (mg)
m_r	Resorbed bone mass fraction
m_s	Mass of the porous material (mg)
$nmppt$	Number of stem material optimization points
n_p	Number of unit cells
Δn_p	Increment of the number of unit cells
$P_{\%}$	Porosity
S_{bone}	Strength of the bone (MPa)
S_c	Interfacial compression strength (MPa)
sd	Dead zone parameter
S_{en}	Strain energy per unit of bone mass (mJ/mg)
$S_{en,ref}$	Reference strain energy per unit of bone mass (mJ/mg)
S_{Max}	Maximum (apparent) strength of the porous material (MPa)
S_n	Section number
S_R	Slenderness ratio
S_S	Interfacial shear strength (MPa)
S_t	Interfacial traction strength (MPa)
S_Y	Yield strength (MPa)
$S_{Y,ap}$	Apparent yield strength of the porous material (MPa)
tol	Tolerance
U	Strain energy density (mJ/mm ³)
Δu	Displacement (mm)
Δu_N	Normal displacement (mm)

u_{ij}	Directional degree of freedom (mm)
U_N	Normal degree of freedom (mm)
u_{vj}	Vertex directional degree of freedom (mm)
V_{app}	Apparent volume of the porous material (mm ³)
V_{bone}	Volume of the bone (mm ³)
V_{pores}	Volume of the void phase of the porous material (mm ³)
V_{solid}	Volume of the solid phase of the porous material (mm ³)

Greek symbols

α_i	Angle for defining the shape of the stem (°)
Δ	Keypoint shifting distance (μm)
ε	Strain (mm/mm)
$\varepsilon\%$	Difference between solid and beam models
θ	Inclination angle (°)
μ	Mean value
μ_D	Mean strut diameter (μm)
ν	Poisson's ratio
ν_{ap}	Apparent Poisson's ratio of the porous material
ρ	Density of the bone (mg/mm ³)
ρ_{app}	Apparent density of the porous material (mg/mm ³)
ρ_r	Relative density
ρ_S	Density of the solid phase of the porous material (mg/mm ³)
τ	Shear interfacial stress (MPa)
ϕ_{design}	Designed strut diameter (μm)

$\phi_{min}, \phi_{S,min}$	Minimum strut diameter (μm)
ϕ_P	Pore diameter (μm)
ϕ_{rand}	Random strut diameter (μm)
ϕ_S	Strut diameter (μm)
$\phi_{S,max}$	Maximum strut diameter (μm)
σ	Standard deviation
σ_{ap}	Apparent stress of the porous material (MPa)
σ_{AVG}	Average (von Mises) stress (MPa)
σ_N	Normal interfacial stress (MPa)
σ_{MAX}	Maximum (von Mises) stress (MPa)
σ_{VM}	Von Mises stress (MPa)

INTRODUCTION

Hip arthroplasty is a successful procedure for relatively old patients. However, when it comes to younger and more active patients, the outcomes of this procedure are not as good (Swedish Hip Arthroplasty Register 2013, Canadian Institute for Health Information 2015, UK National Joint Registry 2015). Indeed, younger patients need implants (stems) that can not only withstand the increased loads derived from a more demanding physical activity, but also that can last longer (Kurtz, et al. 2009). In addition, the implant shall conserve as much bone stock as possible for an eventual revision. Implant shape and material properties have an impact on these requirements. For instance, large implants may provide great stability, but require more bone resection; on the other hand, smaller implants may improve the stress distribution in the proximal femur, but their stability is usually decreased (Reimeringer, et al. 2013) and the stresses at the bone-implant interface are much higher (Kuiper and Huiskes 1992). On the other hand, while stiff implants cause stress shielding (i.e. reduction of the stresses) of the bone that may lead to its resorption, more flexible implants have been shown to increase the interfacial stresses (Figure 0.1), with the associated increase in the risk of interfacial failure and pain (Kuiper and Huiskes 1992, 1997).

Two strategies have been proposed to simultaneously solve the above problems (decrease stress shielding and obtain appropriate interfacial stresses): 1) optimize the implant shape (Ruben, et al. 2012, Fernandes, et al. 2004, Chanda, et al. 2015), or 2) generate a gradation of the material properties of the stem (Kuiper and Huiskes 1997, Hedia, et al. 2006, Arabnejad Khanoki and Pasini 2012). Additive manufacturing technologies show few restrictions in terms of the shapes that can be produced. This allows the fabrication of porous materials with mechanical properties tailored to certain specifics by simply adjusting their (meso) structure (Figure 0.1). As a result, implants can now be created having the aforementioned optimized shape and gradation of mechanical properties, in order to decrease the effects of stress shielding (bone resorption) and the risks associated with inadequate interfacial stress distribution (failure and pain). Furthermore, with additive manufacturing design changes can be easily introduced, allowing for patient-specific design of hip implants (Figure 0.1).

In order to fully take advantage of these possibilities offered by additive manufacturing for implant design, it is necessary 1) to develop computational models to accurately evaluate the mechanical behavior of porous materials so that these can be tailored, and 2) develop a strategy for the optimization of the shape and material properties distribution of the implants (Figure 0.1) in order to improve their mechanical compatibility with the bone.

The main objective of this thesis is to develop a methodology for the design of a new generation of hip implants taking advantage of the various manufacturing capabilities offered by additive manufacturing technologies. In this way, additive manufactured porous materials are considered for obtaining a gradation in the mechanical properties of the stem such that the stress shielding is reduced and adequate interfacial stresses are obtained. The thesis is divided in three parts aiming, respectively, at 1) determining the cost-effective modeling approach for porous materials, 2) increasing the accuracy of computational model of additive manufactured porous materials, and 3) optimizing a hip stem made of porous materials. For all three parts, computational models were developed.

The present thesis is divided into six chapters. Chapter 1 presents a general literature review about the biomechanics of the femur, the hip implants and porous materials. Chapter 2 aims at formulating the main and specific objectives of the present thesis. Then the chapters 3, 4 and 5 comprise the three articles that attempt to address the proposed problem by answering each specific objective. Chapter 6 provides a summary of the results, and highlights the advantages and limitations of the present thesis, offering some recommendations for future work. A general conclusion follows.

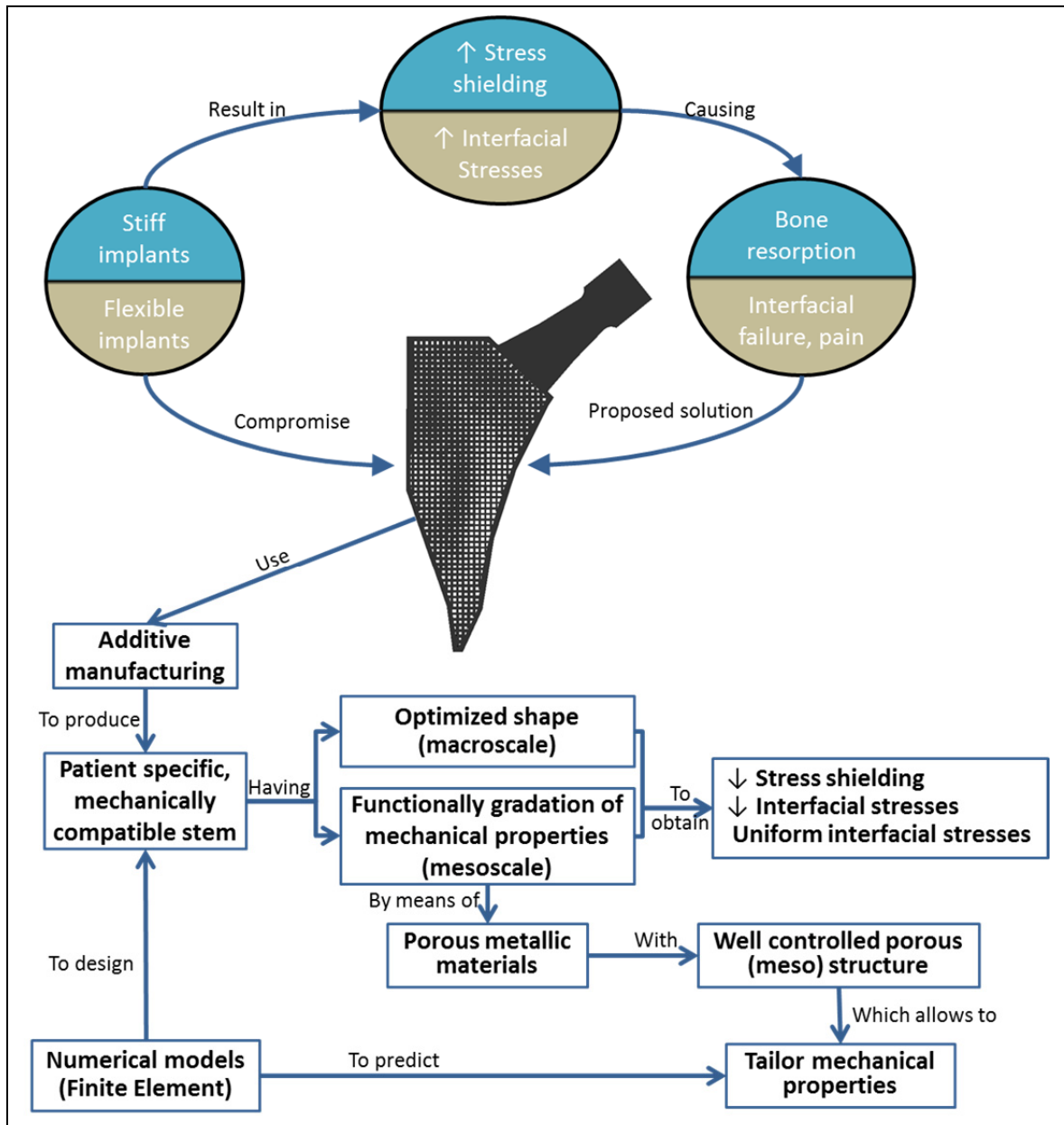


Figure 0.1 General schema of the thesis

CHAPTER 1

GENERAL CONCEPTS AND LITERATURE REVIEW

This thesis relies on concepts from engineering and medicine. More particularly, the context of the problem being solved belongs to the medical field: improving the hip arthroplasty. On the other hand, the tools and concepts that provide the proposed solution are derived from the mechanical engineering and optimization principles: material mechanical behavior, porous materials and hip stem design optimization. This chapter aims at introducing the basic concepts from these disciplines to facilitate the understanding of the thesis. This chapter is structured as follows: first the biomechanics of the femur at the hip joint is depicted; second, the hip arthroplasty is presented; third the numerical analyses and optimization of hip stems are presented; fourth, the porous materials are described.

1.1 The biomechanics of the femur at the hip joint

1.1.1 Anatomy

The femur goes from the hip to the knee, and is the longest bone of the body. It has an almost-cylindrical shape in its central portion (diaphysis). Proximally, the almost-spherical head of the femur articulates with the congruent surface of the pelvic acetabulum, forming the hip joint (Figure 1.1). This joint can be seen as a ball-and-socket (or spheroidal) union that has good range of tridimensional motion (Figure 1.2 - a) and good stability to dislocation. Both articulating surfaces are covered with cartilage that reduces friction and helps to absorb the shocks. The whole joint is enclosed in the synovial capsule, which contains the synovial fluid that provides lubrication and nutrients to the cells of the cartilage as well as helps to absorb shocks. The joint is reinforced by ligaments and muscles that provide stability and generate the movements of the articulation (Tortora 2012).

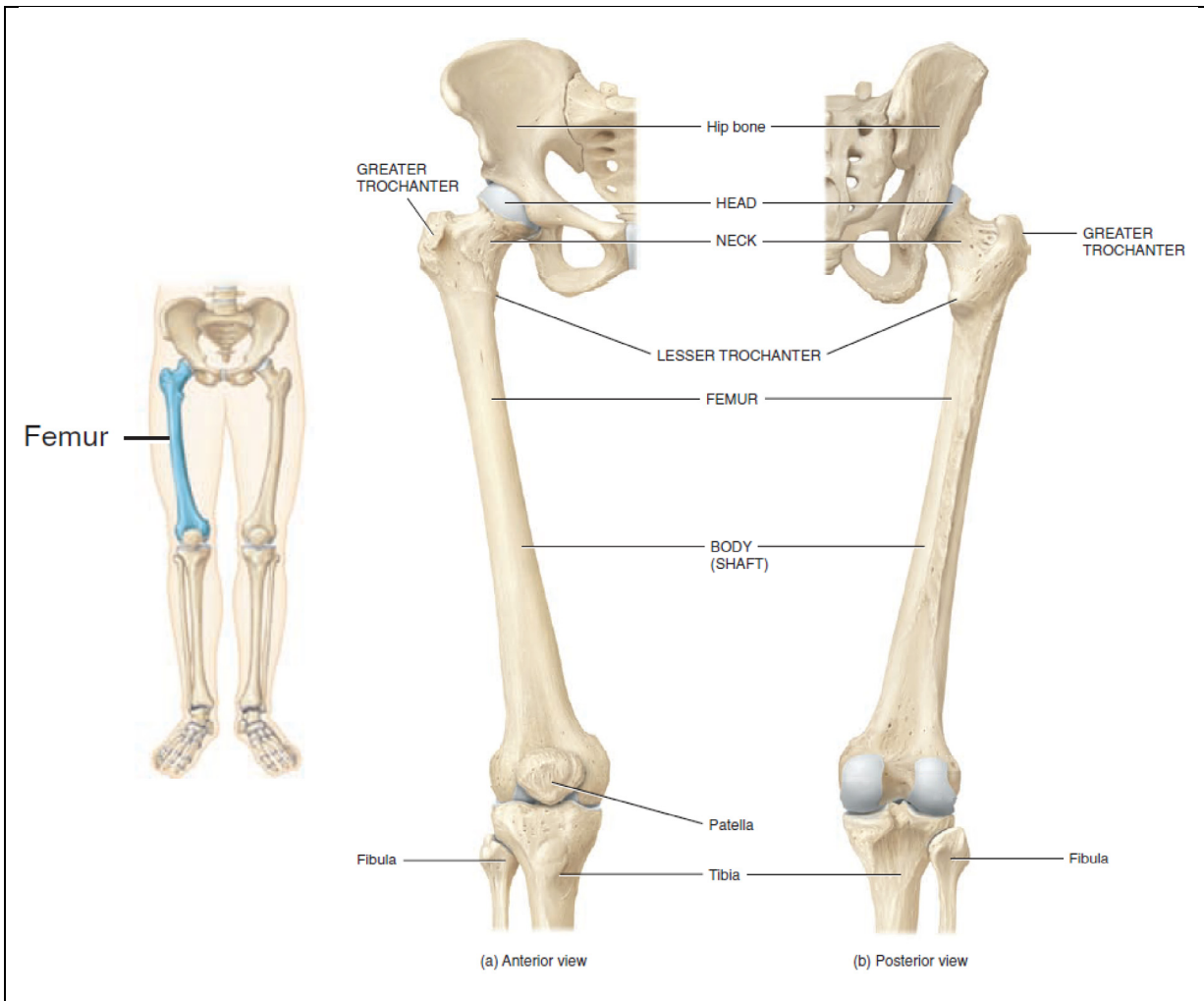


Figure 1.1 The femur.
Adapted from Tortora and Derrickson (2012)

The reference system of the proximal femur is commonly centered in the femoral head (Bergmann, et al. 2001). Three planes are defined: the sagittal, coronal (or frontal) and transversal (or horizontal). Furthermore, three reference directions can be defined: medial-lateral, anterior-posterior and proximal-distal (Figure 1.2 - b).

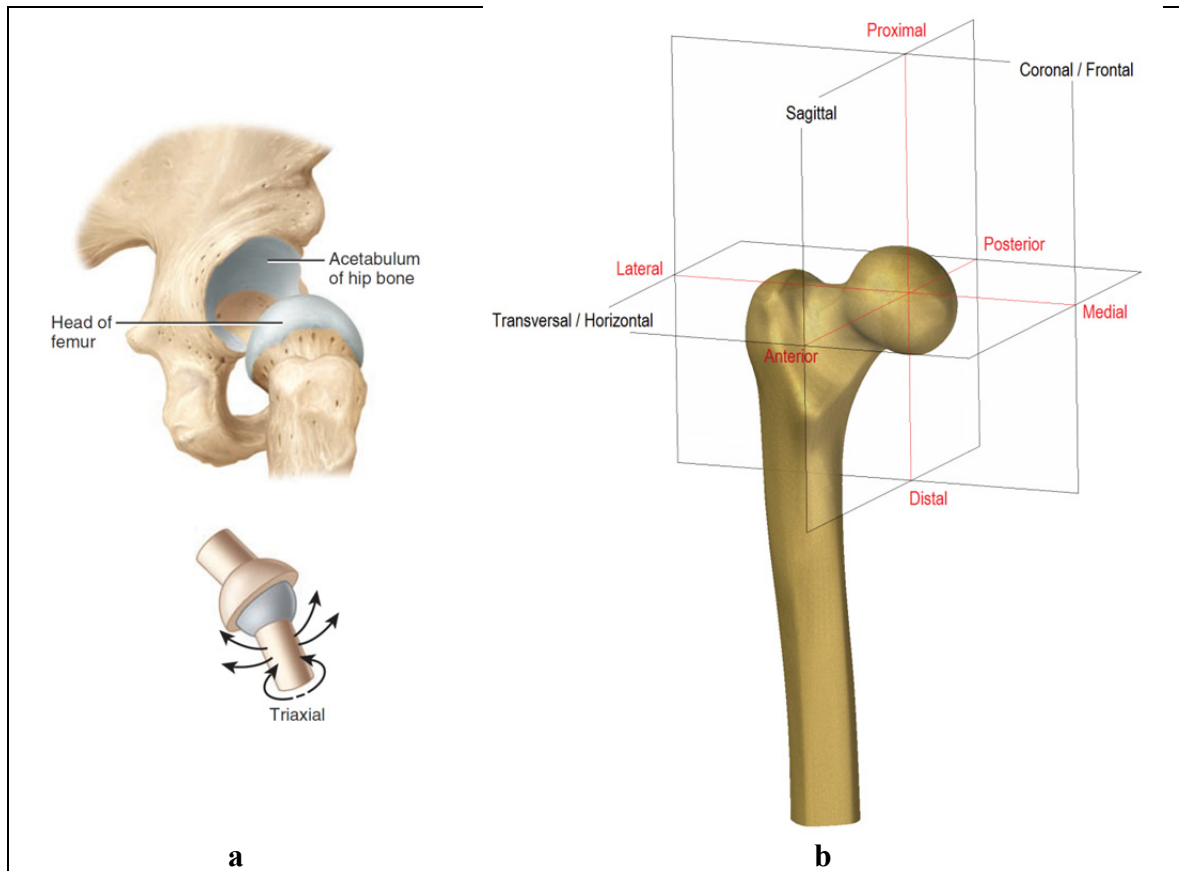


Figure 1.2 (a) The hip joint and its movements (adapted from (Tortora 2012)); (b) reference system of the femur

1.1.2 Forces

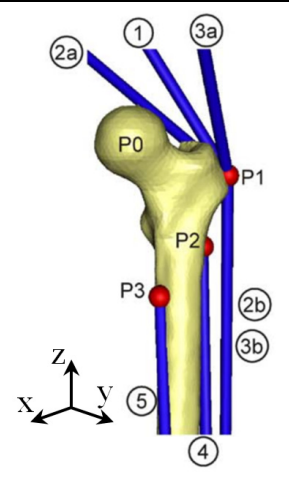
The load conditions at the proximal femur are dictated by the contact force of the hip joint and the muscular forces. The magnitude and direction of these loads depend on the activity (Bergmann, et al. 2001). The main attachment zones for the muscles at the proximal femur are the greater trochanter, situated laterally and the lesser trochanter, in medial orientation (Figure 1.1). An extensive description of the muscles attached to the femur is out of the scope of this work, and can be found, for instance in (Marieb 1999).

The values for the hip contact force have been measured by Bergmann et al. (2001) for different daily activities using instrumented implants. The authors found that this force can be up to 300% of the bodyweight. Heller et al. (2005) determined, using inverse dynamics,

that in order to respect physiological-like loading conditions at the proximal femur, the muscle forces could be simplified to the action of the hip contact force and 5 muscular groups: abductor, ilio-tibial tract, tensor fascia latae, vastus lateralis and vastus medialis. The values of the forces (in % of bodyweight) and the corresponding representation for the stair climbing activity, as determined by Heller et al. (2005) are given in Table 1.1.

Table 1.1 Muscle forces (in % of the bodyweight) and their representation for stair climbing.
Taken from Heller et al. (2005)

Force	Value x	Value y	Value z
Hip contact	-59.3	-60.6	-236.3
Abductor (1)	70.1	28.8	84.9
Ilio-tibial, proximal (2a)	10.5	3.0	12.8
Ilio-tibial, distal (2b)	-0.5	-0.8	-16.8
Tensor fascia latae, proximal (3a)	3.1	4.9	2.9
Tensor fascia latae, distal (3b)	-0.2	-0.3	-6.5
Vastus lateralis (4)	-2.2	22.4	-135.1
Vastus medialis (5)	-8.8	39.6	-267.1



1.1.3 Mechanical properties

The mechanical properties of the bone change continuously to adapt to the mechano-biological environment (García, et al. 2002). This makes it very complicated to provide an exact value for the mechanical properties of the bone, since in addition to this evolution, they change from bone to bone, with the location within the bone, with its quality (i.e. density and mineralization), and the measurements are influenced by the conditions of the test (Currey 2002). On the other hand, although bone is an orthotropic material, in many computational (finite element) studies it is considered as isotropic (see for instance Huiskes, et al. (1992), Tomaszewski, et al. (2010), Arabnejad Khanoki and Pasini (2012), Chanda, et al. (2015)). Therefore in the present thesis, it will be treated as such.

At a macroscopic level, the bone can be divided into compact or cortical and cancellous or trabecular bone. The cortical bone is mostly solid, with only around 10% porosity; on the counterpart, the cancellous bone is formed by an architecture of trabeculae that results in around 50 – 90% porosity with large spaces that are observable at the naked eye (Sikavitsas, et al. 2001, Currey 2002). In the femur, only cortical bone can be identified at the central portion (diaphysis), whereas the extremities (metaphysis) are composed by both types of bone, being the cancellous predominant (Figure 1.3).

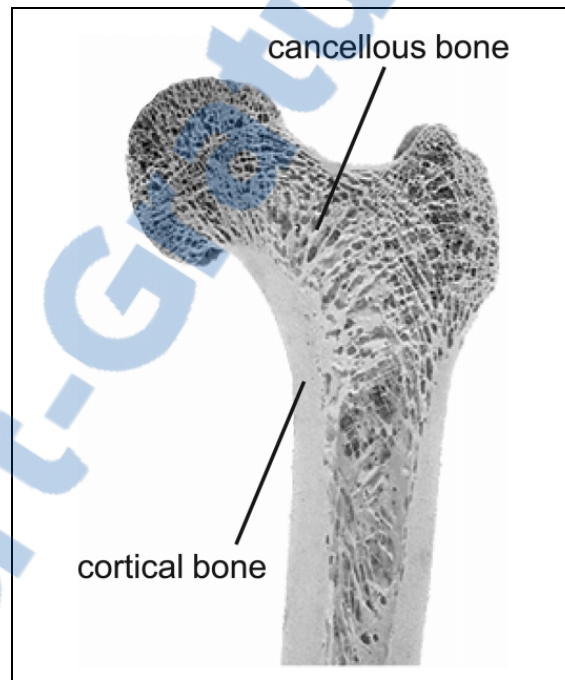


Figure 1.3 Cortical and cancellous bone
Taken from Willems et al. (2014)

Each type of bone has well differentiated mechanical properties, and these are commonly related to its density (or porosity), allowing for the use of general expressions for the mechanical properties and for the personalization of the finite element (FE) models by relating the density to computer tomography data (see for instance Keyak and Falkinstein (2003), Chanda, et al. (2015)). Moreover, the changes in the bone are often referred to as changes in density (García, et al. 2002, Huiskes, et al. 1987). Therefore, one can also track the evolution of mechanical properties of bone. It is not the objective of this section to provide a detailed review of the reported values for the mechanical properties. Instead, the

aim is to provide the reader with an idea of the ranges for these mechanical properties that allows positioning the bone with respect to other materials. In the following the main mechanical properties of bone and their relationship with bone density (ρ) are depicted.

1.1.3.1 Elastic modulus

The elastic modulus (E) of cortical bone is commonly found in the range 10 GPa – 22 GPa; while for cancellous bone reported values are commonly in the range 0.03 GPa to 2.5 GPa (Reimeringer and Nuño 2014). One of the most commonly used expressions for relating the cortical and cancellous E elastic to ρ (Eq. (1.1)) was proposed by Carter and Hayes (1977).

$$E = 3790 \cdot \rho^3 \quad (1.1)$$

1.1.3.2 Strength

Similar to the elastic modulus, large variations are found for the strength of bone (S_{bone}). The cortical bone strength is commonly reported in the range 133 MPa to 158 MPa (Currey 2002), while the strength of cancellous bone is between 1 MPa and 50 MPa (Carter and Hayes 1977). One of the most common relationships between S_{bone} and ρ , proposed by (Carter and Hayes 1977), is shown in (Eq. (1.2)).

$$S_{bone} = 68 \cdot \rho^2 \quad (1.2)$$

1.1.3.3 Interfacial strength

At the bone-implant interface, a multiaxial stress state can be identified: normal (traction and compression) and tangential (shear) stresses occur. Stone et al. (1983) and Kaplan et al. (1985) determined the strength of the bone at the interface in both directions, obtaining the power expressions (Eqs. (1.3) - (1.5)) for the traction ($S_t=2.6-7.6$ MPa), compression ($S_c=8.3-12.4$ MPa), and shear ($S_s=4-6$ MPa) strengths as a function of ρ .

$$S_t = 14.5\rho^{1.71} \quad (1.3)$$

$$S_c = 32.4\rho^{1.85} \quad (1.4)$$

$$S_s = 21.6\rho^{1.65} \quad (1.5)$$

1.2 Total hip arthroplasty

Osteoarthritis (OA) or degenerative arthritis is the most common disease of the hip, and consists in the degeneration of the articular cartilage. In advanced stages, it is accompanied by severe pain and limitation in daily activities, and the solution is to perform a total hip arthroplasty (THA) (Siopack and Jergesen 1995, Pivec, et al. 2013). During the period 2013-2014 OA accounted for 74.7% of the hip arthroplasties in Canada while hip fracture was the second most common cause with 14.5% of the replacements (Canadian Institute for Health Information 2015). OA is also the main indication in other countries. For instance, it accounts for 85% of male and 79.8% of female arthroplasties in Sweden (Swedish Hip Arthroplasty Register 2013) and 93% of the replacements in the United Kingdom (UK National Joint Registry 2015).

In THA, both sides of the hip joint are replaced with the objective of reducing or eliminating pain and restoring the function of the hip (Pivec, et al. 2013). The most common configuration of hip implants is shown in Figure 1.4. It comprises a metallic shell and a polyethylene or ceramic liner on the acetabular side, and a metallic stem with a metallic or ceramic head on the femoral side. Most modern prostheses allow some degree of modularity, with different choices for the stem neck and head in order to reproduce the adequate anatomy of a healthy hip. This thesis is focused in the femoral component, and in the following the terms (hip) implant or prosthesis will refer to this component

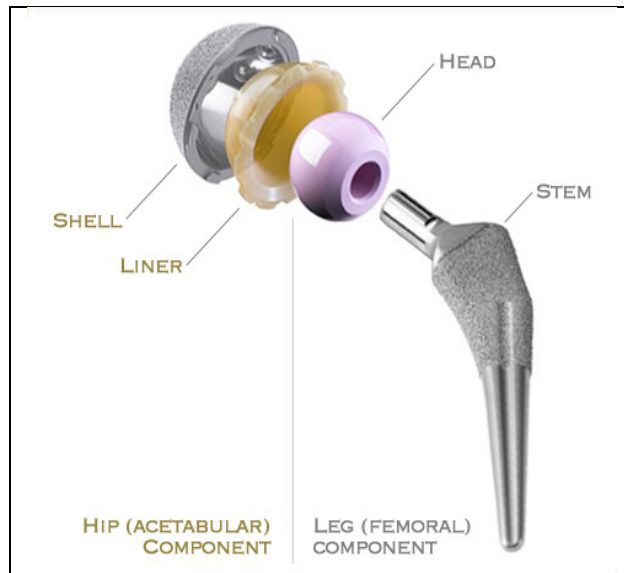


Figure 1.4 Total hip replacement components.
Taken from Ever Smith (2007-2008)

Hip stems are usually made of titanium (Ti6Al4V), which has shown superior biocompatibility, corrosion resistance and closer mechanical properties to bone ($E=110$ GPa), compared to other alloys, such as cobalt-chrome-molybdenum (CoCrMo, $E=210$ GPa) (Learmonth, et al. 2007, Mai, et al. 2010).

The implant can be fixed using cement (Poly-Methyl Methacrylate Acid), guaranteeing its stability immediately after the operation; however, cementless fixation is preferred nowadays (Berry and Bozic 2010, Pivec, et al. 2013). For this type of fixation, the initial mechanical stability is usually achieved by press-fit (Khanuja, et al. 2011), and the secondary (i.e. long-term) stability is obtained by bone ingrowth (Learmonth, et al. 2007, Mai, et al. 2010). To this end, the implant is made porous where bone ingrowth is desired, and in some occasions, hydroxyapatite (calcium phosphate) is included to enhance osteoconductivity (Learmonth, et al. 2007, Mai, et al. 2010, Khanuja, et al. 2011).

Different stem designs exist with the objectives of establishing proper contact and achieving sufficient initial stability so that bone ingrowth can happen (Khanuja, et al. 2011), and guaranteeing the long-term survivorship of the implant. According to their shape, stem

designs can be classified into: anatomic (Figure 1.5 – a), which try to replicate the natural curvature of the femur; cylindrical (Figure 1.5 – b), which rely on distal cortical support to reach immediate stabilization; and tapered (Figure 1.5 – c), which show a wedged shape and achieve fixation in the cortical bone just below the lesser trochanter (Learmonth, et al. 2007, Mai, et al. 2010). Amongst these designs, anatomic and tapered stems show somewhat better results, compared to cylindrical stems (Mai, et al. 2010) and thus are the most common choice.

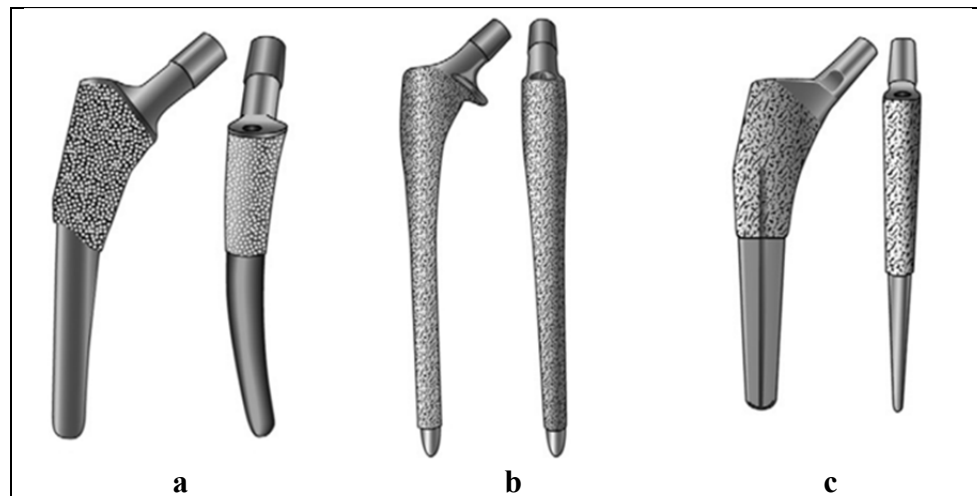


Figure 1.5 (a) Anatomical, (b) cylindrical and (c) tapered cementless stems. The hatched represents the porous coated zone for bone ingrowth.
Adapted from Khanuja et al. (2011)

1.2.1 Epidemiology and future perspectives

In Canada, 49,503 hospitalizations related to hip replacement were registered in the period 2013-2014, which represents an annual increase of 5% and a 5-year increase of 19.1% (Canadian Institute for Health Information 2015). Worldwide the same tendency has been observed, with more than a million THA performed every year and the prevision of doubling this number within the next two decades (Pivec, et al. 2013).

In addition, patients are younger: in Canada, 40.4% (males) and 26.8% (females) of all hip arthroplasties recipients in the period 2013-2014 were under 65 years old (Canadian Institute

for Health Information 2015). In other countries, similar rates have been observed: in Sweden, the proportion of young patients increased from around 50% to almost 60% for men and from around 40% to almost 50% for women in the period 1992-2011 (Swedish Hip Arthroplasty Register 2013). Predictions are that up to 50% of all THA will be done in patients under 65 years old by 2030 (Kurtz, et al. 2009).

1.2.2 Main related problems

The commonly accepted lifespan of a hip stem is 15 years (Siopack and Jergesen 1995); however some studies have found up to 22.6 years implant survivorship (Khanuja, et al. 2011). Multiple factors affect this long-term survivorship of the arthroplasty, including a careful patient selection and surgical technique, the stem design and material resistance (Mai, et al. 2010, Pivec, et al. 2013). Younger patients are considered a risk population for hip arthroplasty, since they have higher activity levels and require implants with increased longevity (Kurtz, et al. 2009). This translates in higher failure rates for younger patients. For instance, in Canada the 5.44% revision rate for patients under 45 years old contrasts with the 1.72% for patients over 85 years old (Canadian Institute for Health Information 2015). In the United Kingdom, patients under 55 years old showed 7.26% 10-year revision rate whereas patients over 75 years old only showed 2.83% (UK National Joint Registry 2015). In Sweden patients under 50 years show up to 40% 20-year revision rate, compared to the 10% for patients over 75 years (Swedish Hip Arthroplasty Register 2013).

The implant failure comes generally in the form of aseptic (without infection) loosening. This represented 23.9% of failures in Canada in 2015 (Figure 1.6). This is also true worldwide. For instance, aseptic loosening represented approximately 40% of the revisions in Sweden during 2013; and 24.4% of the revisions in the United Kingdom.

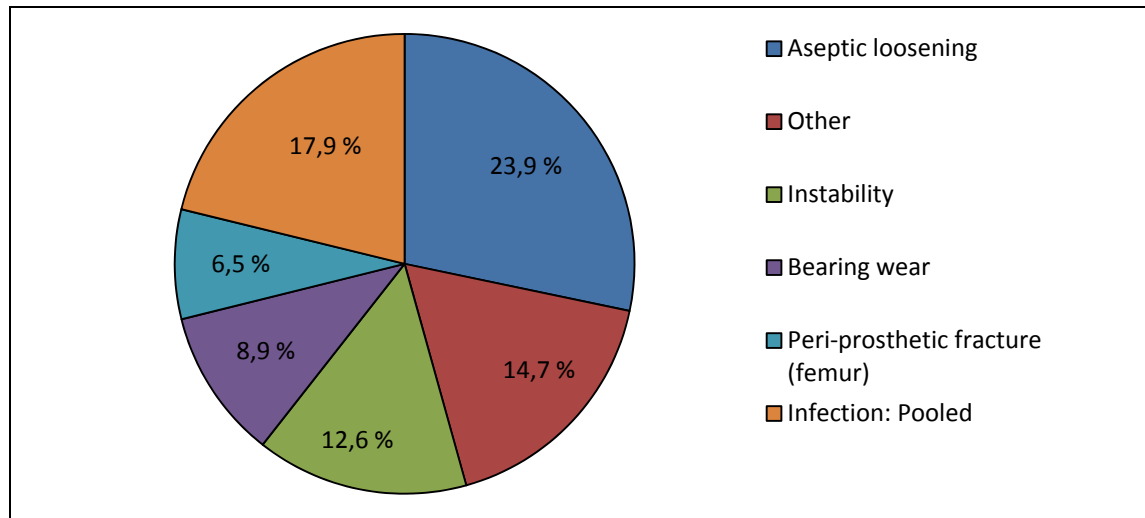


Figure 1.6 Causes for revision of the arthroplasty in Canada
Source: Canadian Institute for Health Information (2015)

1.3 Numerical analysis of hip implants

In an attempt to improve THA longevity, numerical (finite element) analysis allows researchers to study stresses and strains within the bone and at the stem-bone contact interface, as well as to evaluate implant stability, bone resorption or simulate bone remodeling. Therefore, the causes of mechanical-related implant failure can be analyzed and the implants can be optimized to improve their mechanical compatibility with bone.

1.3.1 Mechanical causes of implant failure

It is believed that the bone loss caused by the stress shielding effect and the interfacial failure due to improper interfacial conditions may contribute to the aseptic loosening of the implant (Kuiper and Huiskes 1997, Arabnejad Khanoki and Pasini 2012).

1.3.1.1 Stress shielding

When the femoral bone is partially replaced by a stiffer metallic hip stem, a redistribution of the mechanical stimuli within the bone occurs in such a way that the stresses are decreased at

the proximal femur. The bone is hence stress shielded, and being a living tissue that reacts to the mechanical stimuli (Huiskes, Weinans, et al. 1987), bone can be partially resorbed. The clinical impact of such bone resorption due to stress shielding may not be clear yet; however the diminution of the bone stock and quality that this phenomenon causes may compromise a future revision arthroplasty (Kuiper and Huiskes 1992, Mai, et al. 2010). Flexible and less invasive (i.e. smaller) implants have been shown to decrease the stress shielding (Huiskes and Boeklagen 1988, Weinans, et al. 1992, Kuiper and Huiskes 1992). In this way, Kuiper and Huiskes (1992) computed 70% decrease in the resorbed bone mass for a 70% reduction of the implant elastic modulus.

From a computational point of view, the bone resorption due to stress shielding is quantified by means of the changes in the bone density (ρ). Such changes are generally assumed to be proportional to the variations in the strain energy per unit of bone mass ($S_{en} = U / \rho$, where U is the strain energy density). Although detailed algorithms that model the time-dependent ρ evolution exist (see for instance García, et al. (2002)), the simpler formulation proposed by Kuiper and Huiskes (1997) is commonly used for quantifying the effects of stress shielding. This considers that the bone is resorbed if S_{en} for the implanted bone is lower than a reference case ($S_{en,ref}$), which is usually the original (non-implanted) bone. In order to take into account the variations in S_{en} that do not carry changes in ρ , the dead-zone parameter (sd) is introduced. This formulation gives place to the binary resorption function ($g(S_{en})$) shown in Eq. (1.6):

$$g(S_{en}) = \begin{cases} 1 & \text{if } S_{en} < (1 - sd) \cdot S_{en,ref} \\ 0 & \text{otherwise} \end{cases} \quad (1.6)$$

and, the resorbed bone mass fraction (m_r) can be computed for the entire bone volume (V_{bone}) by dividing by the total bone mass (M), as shown in Eq. (1.7).

$$m_r = \frac{1}{M} \int_{V_{bone}} g(S) \cdot \rho \cdot dV_{bone} \quad (1.7)$$

1.3.1.2 Interfacial failure

Large stresses at the bone-implant contact may result in the interfacial failure. In addition, it has been suggested that they can increase the level of pain and, in the immediate post-operative situation, result in larger interfacial micro-movements that would inhibit bone ingrowth (Kuiper and Huiskes 1997). Similarly to the stress shielding, the interfacial failure depends on the characteristics of the implant (mechanical properties and shape). Kuiper and Huiskes (1992, 1997) showed that the peaks of interfacial stresses are increased and shifted proximally with flexible stems (Figure 1.7), and Chanda et al. (2015) found that less invasive stems would result in more critical interfacial conditions.

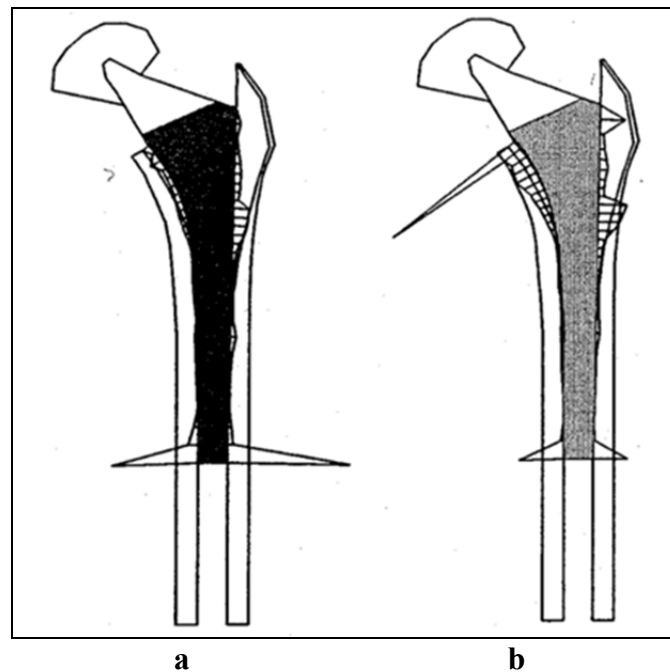


Figure 1.7 Interfacial failure index for (a) solid titanium and (b) flexible stems.

Taken from Kuiper and Huiskes (1992)

Few researchers have considered the short-term failure of implants, addressed by the interfacial displacements (Fernandes, et al. 2004, Ruben, et al. 2012). Nevertheless, the most common approach is to consider the long-term failure, based on a local interfacial failure index (f_{IS}) that takes into account normal (σ_N) and/or shear (τ) interfacial stresses. In its most

general form, this index is based on the Hoffman multiaxial failure criterion (Pal, et al. 2009), as shown in Eq. (1.8).

$$f_{IS} = \frac{\sigma_N^2}{S_t S_c} + \left(\frac{1}{S_t} - \frac{1}{S_c} \right) \sigma_N + \left(\frac{\tau}{S_s} \right)^2 \quad (1.8)$$

The values of S_t , S_c and S_s are the traction, compression and shear bone interfacial strengths, which can be related to bone density as shown in section 1.1.3.3. A common simplification to this index is to consider only the failure by shear stress (Kuiper and Huiskes 1997, Arabnejad Khanoki and Pasini 2013b). In such cases, only the last term of Eq. (1.8) is taken into account ($f_{IS} = (\tau / S_s)^2$).

A global interface index (F_{IS}) is generally constructed by averaging over the entire area in contact ($F_{IS} = 1/A \int f_{IS} \cdot dA$) (Kuiper and Huiskes 1997); although formulations based on the maximum local value have also been proposed (Arabnejad Khanoki and Pasini 2013b).

1.3.2 Improvement of stem performance

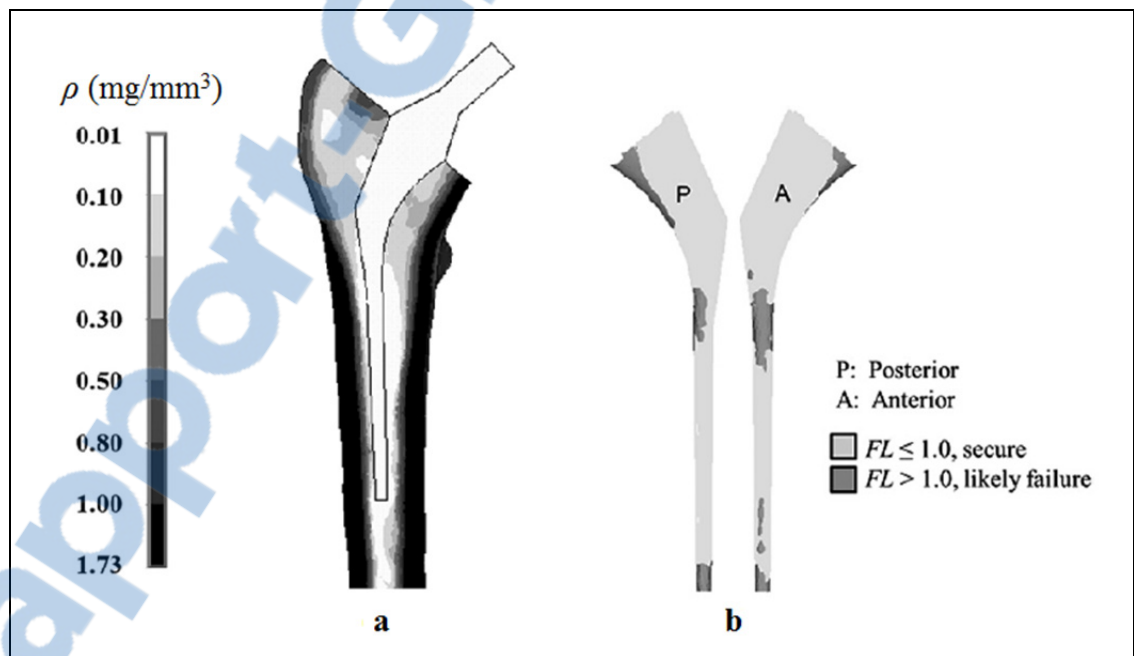
In the previous section, it was shown that the stem characteristics (e.g. shape and mechanical properties) produce contradictory effects that can lead to implant failure. Therefore a compromise has to be found, and two methodologies to address this specific problem have been proposed: 1) optimize the implant shape and 2) design functionally graded stems.

1.3.2.1 Optimization of implant shape

To optimize the stem shape (Figure 1.8), 2D (Huiskes and Boeklagen 1989, Fernandes, et al. 2004) and 3D (Kowalczyk 2001, Ruben, et al. 2012, Chanda, et al. 2015) models have been employed. In these problems, a set of geometrical variables defines the shape of the stem; while constraint relationships between the variables assure proper shape of the implant. A variety of objective functions have been used based on the interfacial stresses/failure

(Huiskes and Boeklagen 1989, Kowalczyk 2001, Fernandes, et al. 2004, Ruben, et al. 2012), interfacial displacements (Fernandes, et al. 2004, Ruben, et al. 2012), and bone resorption (Ruben, et al. 2012, Chanda, et al. 2015).

Although single-objective optimization has been performed (Kowalczyk 2001), the multi-objective optimization is more common (Fernandes, et al. 2004, Ruben, et al. 2012, Chanda, et al. 2015). In this way, Fernandes et al (2004) compared these two approaches, finding that the multi-objective optimization provides compromise solutions within the boundaries given by the single-objective optimization. For multi-objective optimization, genetic algorithms have been a choice in recent studies (Chanda, et al. 2015) since they allow the determination of a large set of optimal solutions, from which the desired solutions can be selected afterwards according to either one or the other objective.



In general, stems having wedged shape, with thick distal tip and almost rectangular cross sections improve the primary stability (minimize interfacial displacements) (Fernandes, et al.

2004, Ruben, et al. 2012). On the other hand, minimally invasive implants having small (thin) tip have resulted in decreased interfacial stresses (Fernandes, et al. 2004, Ruben, et al. 2012, Chanda, et al. 2015). Furthermore, such minimally invasive implants lead to a diminution of the bone resorption (Ruben, et al. 2012, Chanda, et al. 2015). Recent studies have shown (Figure 1.8) that optimized stems can reduce the interfacial failure by 68% compared to standard stems, while bone resorption has been decreased from 39% to 24-27% (Chanda, et al. 2015).

1.3.2.2 Functionally graded stems

Another approach that has been proposed seeks at optimizing the non-uniform distribution of mechanical properties of the stem (Figure 1.9). Implants conceived according to this principle are said to be functionally graded (FG). For this approach, only 2D models have been considered (Kuiper and Huiskes 1992, Simoes, et al. 1998, Hedia, et al. 2006, Arabnejad Khanoki and Pasini 2012). In this problem, the variables are the mechanical properties (e.g. the elastic modulus) at a certain number of optimization points distributed within the stem. Some authors have evaluated the performance of such stems in terms of a combination of the strain energy density and principal stresses on the bone and the cement (for cemented prostheses) (Simoes, et al. 1998), or a combination of the von Mises stress and the interfacial stresses (Hedia, et al. 2006). However, the most commonly used approach considers the multi-objective optimization in terms of the resorbed bone mass fraction and the interfacial failure (Kuiper and Huiskes 1992, Arabnejad Khanoki and Pasini 2012, 2013b, 2013c).

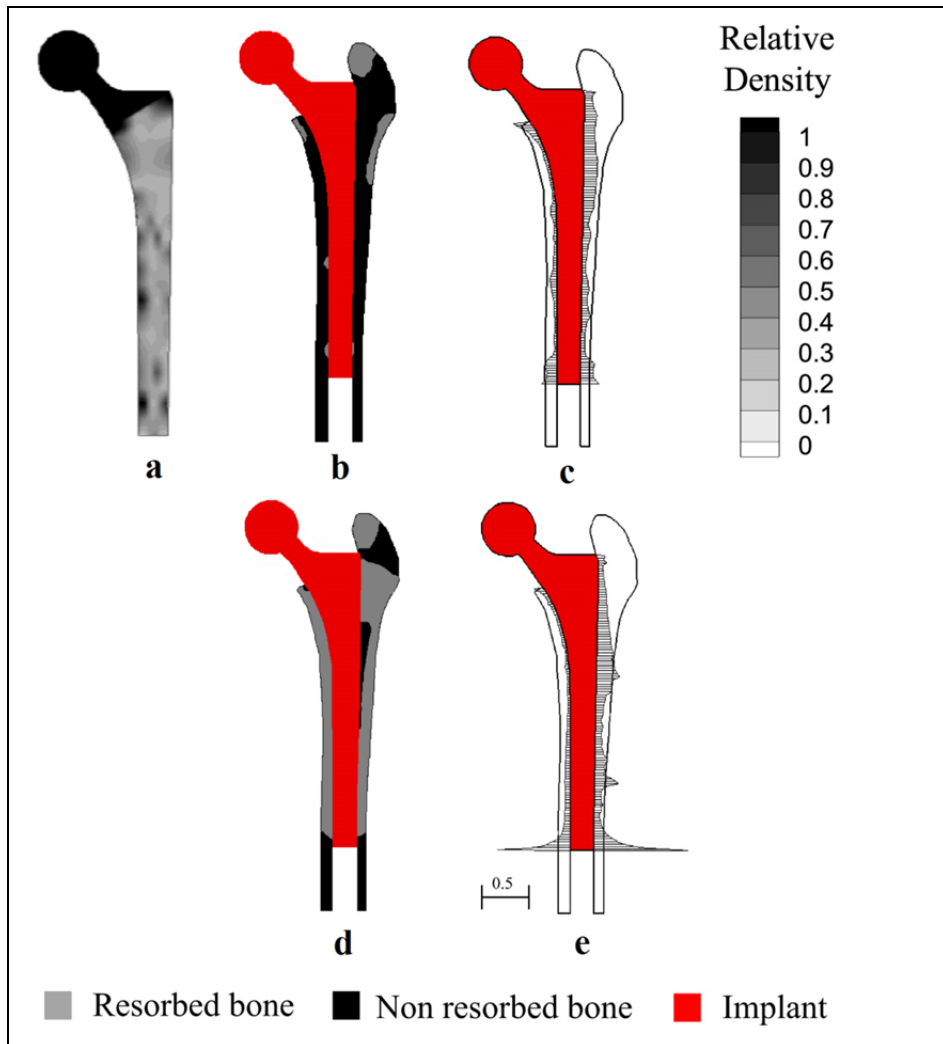


Figure 1.9 (a) Porous material density distribution; (b) bone resorption; (c) interfacial shear stresses for a functionally graded hip stem; (d) bone resorption; (e) interfacial shear stresses for a solid Ti6Al4V stem. Adapted from Arabnejad Khanoki and Pasini (2013c)

Different strategies have been proposed for designing the FG of the implants. Kuiper and Huiskes (1992) considered linear variations of the elastic modulus along the stem length. Hedia et al. (2006) performed a linear interpolation between 3 points located at the proximal and distal ends of the FG implant. Simões et al. (1998) compared linear, square root and logarithmic continuous variations of the material of the stem from proximal to distal. More recently, Arabnejad Khanoki and Pasini (2012, 2013b, 2013c) considered a grid of 130 material optimization points uniformly distributed along the stem with linear interpolation

between the points, which resulted in more general non-uniform distribution of the mechanical properties of the stem (Figure 1.9).

In general, best results have been obtained with optimized stems being stiffer at the proximal and medial levels than distally and laterally (Kuiper and Huiskes 1992, Simões, et al. 1998, Hedia, et al. 2006, Arabnejad Khanoki and Pasini 2012). Compared to standard stems, FG stems have shown to reduce stress shielding and yield better interfacial conditions. Arabnejad Khanoki and Pasini (2012) determined that compared to a standard titanium stem, the FG stem could produce 76% and 50% reduction in terms of bone resorption and peak interfacial failure, respectively.

To obtain the FG of material properties, different options have been proposed. Simões et al. (1998) considered a cobalt-chrome core with a controlled stiffness composite outer layer. Hedia et al. (2006) obtained the FG by means of a mixture of collagen, ceramic (bioglass) and metallic materials. Nevertheless, the most interesting approach has been recently proposed by Arabnejad Khanoki and Pasini (2012), who took advantage of additively manufactured porous materials. As it will be described in the next section, such materials allow for the tailoring of their mechanical properties by controlling their geometrical parameters. This has led to an increasing interest for such materials not only for hip stems, but also for other implants where tailored mechanical properties are needed and/or bone ingrowth is desired such as long bone defect regeneration (Wieding, et al. 2014), acetabular cups with enhanced fixation properties (Marin, et al. 2010), or stems for total knee arthroplasty with better mechanical compatibility with the bone (Murr, et al. 2011).

1.4 Porous materials

Gibson and Ashby (1999) defined a porous material as “*an interconnected network of solid struts or plates which form the edges and faces of cells*”. Since such network has its own set of effective mechanical properties, it is a material itself and can be compared with common bulk materials (Ashby, 2006). The material can be found forming walls (or plates), resulting

in “*closed-cell*” porosity; or struts, resulting in an interconnected network of “*open-cell*” pores (Gibson 2005). On the other hand, the porous material may have a random nature, in which case it is referred to as foam; or result from the 3D uniform repetition of a base unit cell (tessellation), in which case it is called lattice or well-ordered.

Three different size levels or scales can be identified in a porous material: macroscale, mesoscale and microscale (Figure 1.10). The macroscale defines the (external) dimensions of the part, and it can go from some millimeters to several centimeters. At the mesoscale, the details of the porous structure can be observed (e.g. unit cell shape and dimensions). This scale goes from hundreds to some thousands of microns, lying between the macroscale and the microscale. The microscale which cannot be seen to the naked eye, goes up to several micrometers and contains information at the strut level (e.g. crystallographic composition of the material).

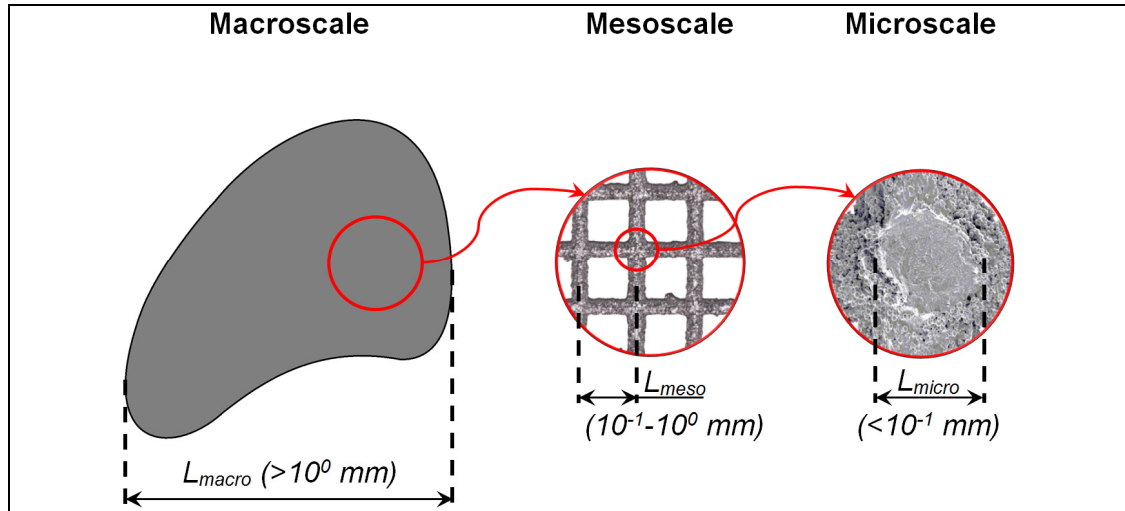


Figure 1.10 Macroscale, mesoscale and microscale of a porous material

1.4.1 Well-ordered porous materials

Non stochastic (i.e. well-ordered) porous materials result in similar stiffness than stochastic foams (Murr, et al. 2011), with higher specific strength (Cheng, et al. 2012). Therefore, this thesis is focused on porous materials having a well-ordered structure at the mesoscale

(lattices). Furthermore, since the planned application is load-bearing prosthesis, titanium (Ti6Al4V) material is considered for being the most commonly used material in hip stems (Learmonth, et al. 2007, Mai, et al. 2010). In the following, the terms porous, lattice, well-ordered porous or cellular materials may be used indistinctively, referring in all cases to porous materials resulting from the 3D repetition of a base unit cell.

1.4.2 Main geometrical parameters of porous materials

The unit cell geometry at the mesoscale plays an important role not only on the structural dimensions, but also on the mechanical behavior of porous materials (Gibson 2005). Amongst the different unit cell geometries that have been considered in experimental or computational studies, the two most common are the simple cubic (Heinl, et al. 2008, Parthasarathy, et al. 2010, Parthasarathy, et al. 2011, Hazlehurst, et al. 2013) and diamond unit cells (Cansizoglu, et al. 2008, Heinl, et al. 2008, 2008b, Marin, et al. 2010, Hrabe, et al. 2011, Ahmadi, et al. 2014, Herrera, et al. 2014, Horn, et al. 2014). These are shown in Figure 1.11.



Figure 1.11 (a) Simple cubic and (b) diamond unit cells

Even though porous materials have such non-homogeneous structure at the mesoscale, they are treated as homogeneous at the macroscopic level. Macroscopic dimensions (and mechanical properties) are thus said to be apparent, and they are the dimensions (and mechanical properties) as of the “equivalent” fully solid material. These dimensions can be

computed as the product of the unit cell length at the mesoscale (L_{UC}) times the number of unit cells (n_p) in each spatial direction. The unit cell length depends on the geometry of the unit cell and on the strut (ϕ_s) diameter and pore (ϕ_p) diameter (i.e. the diameter of the largest sphere that can be inscribed in the pore or its 2D projection).

Other parameters, that can be derived from the fundamental ones (L_{UC} , ϕ_s , and ϕ_p), are used for relating the mechanical behavior to the structure of porous materials: the relative density (ρ_r), defined as the ratio from the apparent density of the porous material (ρ_{app}) to the density of the solid material (ρ_s) (Gibson, 2005); the porosity ($P\%$), which is equivalent to ρ_r (Eq.(1.9)) and defined as the ratio of the volume of the pores (V_{pores}) to the apparent volume of the porous material (V_{app}) (Parthasarathy, et al. 2011); or the slenderness ratio (S_R), which gives an idea of the length-to-thickness of the struts (see section 3.3.1).

$$\rho_r = \frac{\rho_{app}}{\rho_s} = \frac{m_s/V_{app}}{\rho_s} = \frac{V_{solid} \cdot \rho_s / V_{app}}{\rho_s} = \frac{V_{solid}}{V_{app}} = 1 - \frac{V_{pores}}{V_{app}} = 1 - \frac{P\%}{100} \quad (1.9)$$

where m_s is the mass of the porous material, V_{solid} is the volume of the solid part of the porous material.

1.4.3 Additive manufacturing of porous materials

The production of materials having such complex, well-controlled porous mesostructure is possible thanks to additive manufacturing technologies (Murr, et al. 2012). In particular, powder-beam based technologies, such as Electron Beam Melting (EBM) and Selective Laser Melting (SLM), also known as Direct Metal Laser Sintering (DMLS) are very popular for the production of such materials.

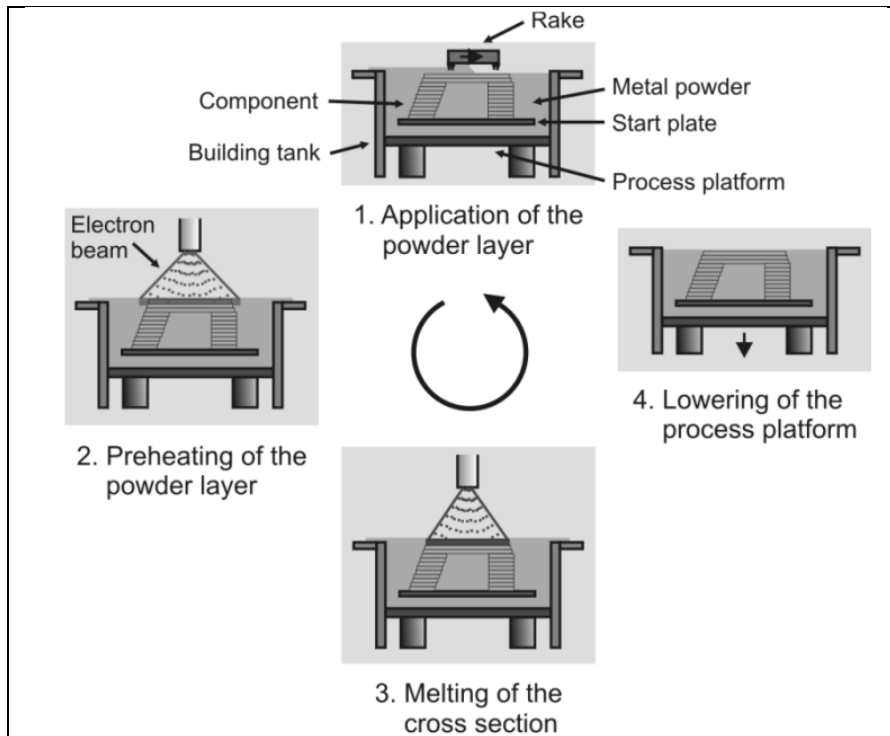


Figure 1.12 The process of additive manufacturing.
Taken from (Heinl, et al. 2008)

Both EBM and SLM (or DMLS) share the same working principle (Figure 1.12). The CAD model of the part to be produced is first sliced in a number of cross-sections. Then an iterative process begins, where the material powder is extended in the fabrication platform. A beam preheats the powder bed and then selectively melts the zones that conform to a specific cross-section of the part. Afterwards the fabrication platform is lowered, a new powder layer is extended and the process is repeated until the part is completed (Heinl, et al. 2008).

The main differences between EBM and SLM processes are outlined in Table 1.2. Apart from differences concerning the powder size, layer thickness and building rate, the most relevant discrepancies arise from the nature of the beam (electron or laser), which forces the EBM technology to work with conductive materials, and also from the working environment that for EBM is vacuum while for DMLS is a mix of inert gas.

Table 1.2 Differences between EBM and DSLM technologies

		EBM	SLM/DMLS
Beam	Nature	Electron	Laser
	Min. Diameter (μm)	100 ^{a)}	100 ^{e)}
Powder size (μm)		45 – 100 ^{b)}	5 – 50 ^{f)}
Accuracy (μm)		130 ^{c)}	± 50 (wall thickness 0.3 – 0.4 mm) ^{f)}
Layer thickness (μm)		100 ^{d)}	20 – 100 ^{e)}
Building rate (mm/h)		6 – 7 ^{d)} (55-80 cm ³ /h ^{c)})	7 – 8 ^{d)} (7.2-72 cm ³ /h ^{e)})
Environment		Vacuum (10^{-5} bar) / Partial pressure of He (10^{-3} bar) ^{a)}	Argon/nitrogen mix ^{d)}
Other		Conductive materials. Pre-sintering of the powder	
Note: ^{a)} (ARCAM AB, Q10 brochure), ^{b)} (ARCAM AB, Ti6Al4V ELI Titanium Alloy brochure), ^{c)} (ARCAM AB, A1 brochure), ^{d)} (Koike, et al. 2011), ^{e)} (EOS, EOSINT M270 brochure), ^{f)} (Rehme and Emmelmann 2006), ^{g)} (EOS, Titanium Ti64ELI brochure)			

1.4.3.1 Irregularities of additively manufactured porous materials

EBM and SLM/DMLS are considered to allow the manufacturing of porous materials with high degree of control over the dimensions at the mesoscale; however, differences between designed and manufactured dimensions arise (Harrysson, et al. 2008). Since the mesoscale dimensions of the porous materials are typically of the same order of magnitude of the accuracy of the technologies (hundreds of microns), the manufacturing errors can represent large percentages of the design dimensions.

At the macroscale, the manufactured sample size of EBM-produced porous materials has been found to be 1% larger than the designed size, with porosity variations up to 23.5% (Parthasarathy, et al. 2011).

At the mesoscale, Li et al. (2009) obtained strut diameter of 750 μm and pore diameter of 1.386 mm, instead of 500 μm and 1.5 mm, respectively for EBM-produced porous materials; while Smith et al. (2013) reported variations up to 17 μm in the strut diameter for SLM. Moreover, differences between the designed and produced strut diameters of 23% (representing $\pm 100 \mu\text{m}$), 20% and 10% have been reported by Parthasarathy et al. (2011), Horn et al. (2014), and Herrera et al. (2014), respectively.

At the microscale, micro-porosities have been reported by Hrabe et al. (2011) and Herrera et al. (2014) for EBM-produced parts; and by Yan et al. (2015) for parts produced by SLM. Campoli et al. (2013) estimated this microporosity to be between 10 and 20%.

1.4.3.1.1 Contribution related to this thesis

As part of the work derived from the present thesis, Vanderesse et al. (2016) showed that DMLS produced porous materials also show differences in the designed and manufactured strut diameter that can be up to 200 μm in average for samples having strut diameters from 500 μm to 1000 μm . These differences were dependent on the strut direction (i.e. on the manufacturing plane or in the perpendicular direction). Moreover, the authors found that the struts were not perfectly straight but there exists a certain inclination in the struts.

1.4.4 Mechanical properties of porous materials

The mechanical behavior of porous materials is often described in terms of the apparent elastic modulus (E_{ap}), the apparent yield strength ($S_{Y,ap}$) and the maximum (apparent) strength (S_{Max}). These can be computed from the uniaxial compression apparent stress (σ_{ap})-strain (ε) curve (Figure 1.13), which is obtained dividing the force by the apparent area and the displacement by the total (apparent) length of the sample. Then, E_{ap} is defined as the slope of the apparent linear zone (in red in Figure 1.13), while $S_{Y,ap}$ is determined at 0.2% deformation and S_{max} corresponds to the maximum stress before the first failure of the sample.

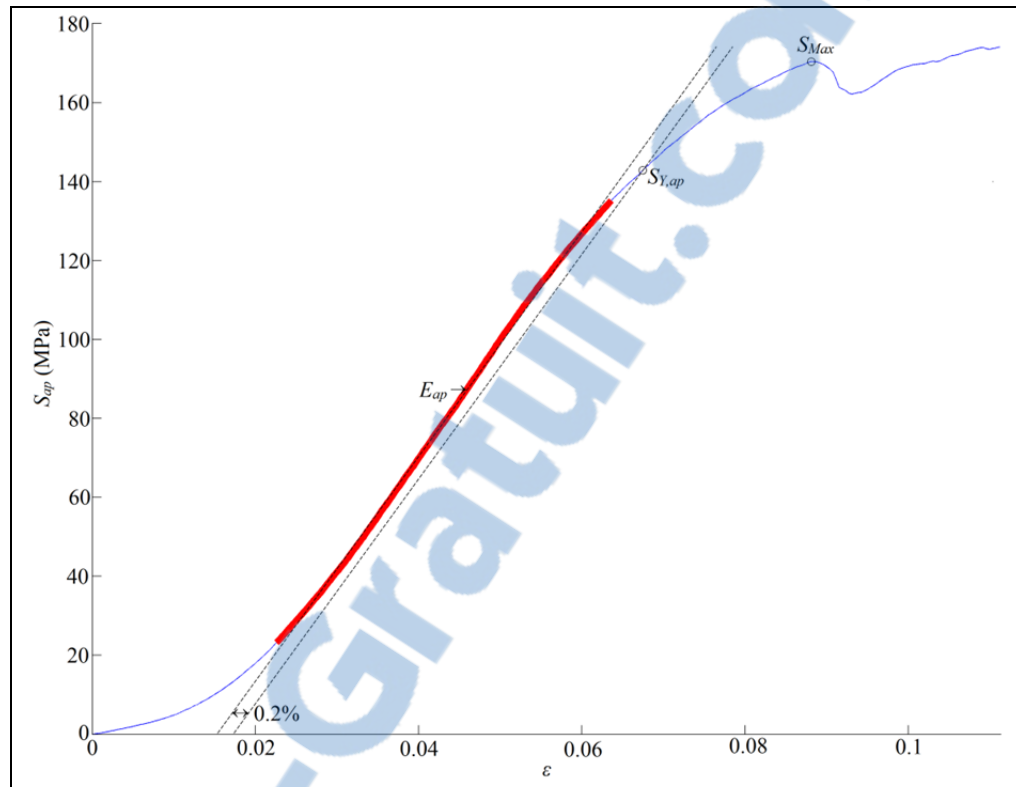


Figure 1.13 Computation of apparent mechanical behavior from the results of an experimental compression test. Apparent linear zone stands in red

1.4.4.1 Experimental testing of porous materials

Experimental testing provides the mechanical behavior of the manufactured samples. In Figure 1.14, reported values from selected studies for E_{ap} under compression and bending of Ti6Al4V porous materials having different unit cell geometries are shown. This is not an extensive review, but it is a representative selection of studies to give an idea of the values and variability that can be obtained for E_{ap} of porous materials. More details and additional studies can be found in APPENDIX I.

The values for E_{ap} show large variations, between 0.047 GPa and 14.05 GPa. These values cover the ranges of the trabecular ($E = 0.03$ GPa - 2.5 GPa) and cortical ($E = 10$ GPa - 22 GPa) bones (see section 1.1.3.1). The unit cell geometry and the dimensions (e.g. porosity or

relative density) play a role on the reported E_{ap} . Nevertheless, results reveal that it is possible to obtain similar ranges for E_{ap} with different combinations of unit cell geometry and dimensions (see e.g. Parthasarathy et al. (2010, 2011), Murr et al. (2011), Cheng et al. (2012) and Herrera et al. (2014)). In addition, similar values are reported for E_{ap} in bending and compression (see for instance Herrera et al. (2014) and Horn et al. (2014)).

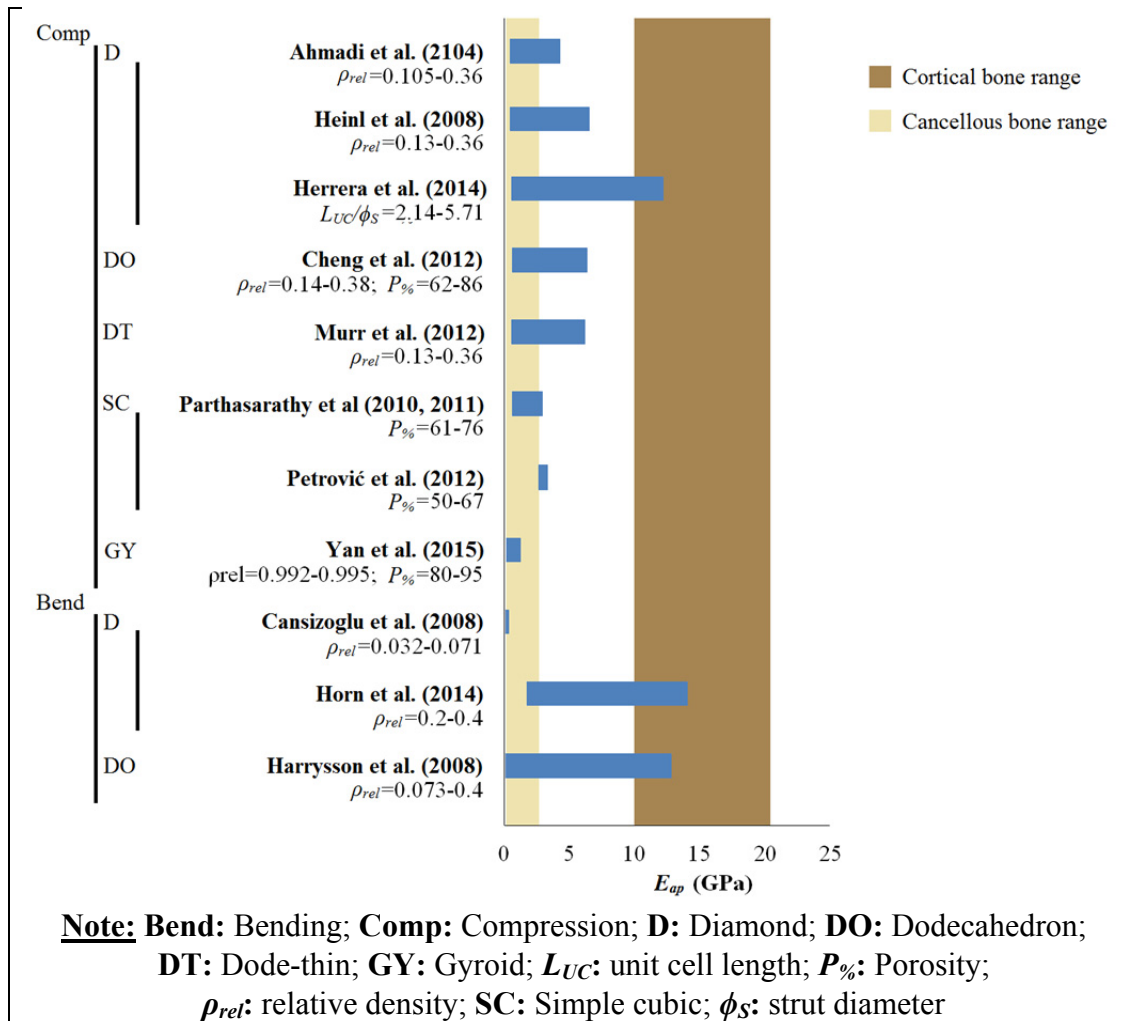


Figure 1.14 Reported values of E_{ap} of Ti6Al4V porous materials

Similarly, as shown in Figure 1.15, large variations have been reported for the values for S_{Max} (between 7.28 MPa and 163.02 MPa) and $S_{Y,ap}$ (between 8.2 MPa and 99.7 MPa). The values cover the range of strength for the cancellous ($S_{bone}=1$ MPa - 50 MPa) and cortical ($S_{bone}=133$ MPa - 158 MPa) bones (see section 1.1.3.2). The values of S_{Max} and $S_{Y,ap}$ are also greatly

influenced by the unit cell geometry and the dimensions (e.g. porosity or relative density). It is also possible to obtain similar ranges for S_{MAX} and $S_{Y,ap}$ with different combinations of unit cell geometry and dimensions (see e.g. Heintl et al. (2008) and Parthasarathy et al. (2010, 2011)). The strength in bending has also been shown to be similar to the compressive strength (see for instance Heintl et al. (2008) and Horn et al. (2014)).

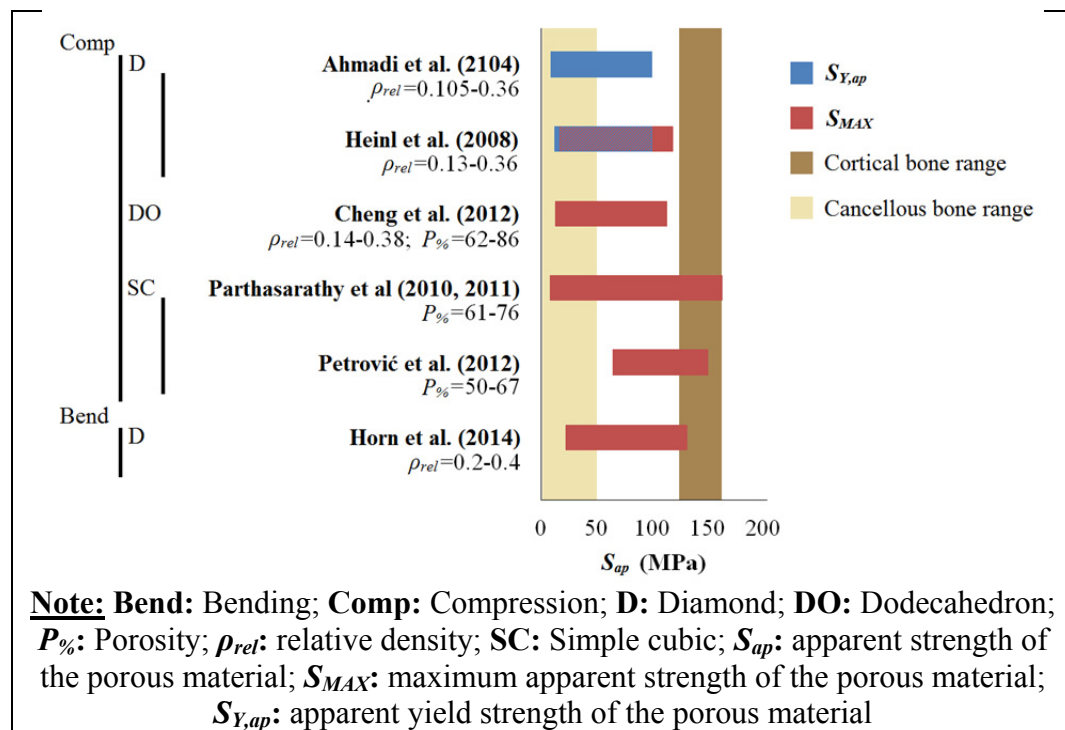


Figure 1.15 Reported values of $S_{Y,ap}$ and S_{MAX} of Ti6Al4V porous materials

Concerning the fatigue behavior, Hrabe et al. (2011) showed that the fatigue strength was somewhat lower than expected, and attributed this to stress concentrators both at the mesoscale or microscale. Amin Yavari et al. (2013) determined that any of the tested porous structures could withstand 10^6 cycles for any load. On the other hand, Amin Yavari et al. (2015) showed that while this was true for diamond and octahedron unit cells, the simple cubic unit cell did not fail after 10^6 cycles even for loads up to $0.8 \cdot S_{Y,ap}$.

Researchers are commonly interested in predicting E_{ap} based on the geometrical parameters of the porous material (e.g. the relative density, ρ_r). To this end, different relationships have

been proposed based on experimental data or on analytical deductions. The most commonly used relationship was proposed by Gibson and Ashby (1999) and considers quadratic relationship between E_{ap} and ρ_r . Recently, Horn et al (2014) showed that such a relationship can well represent the results found by different researchers, for a variety of unit cells. Some commonly used expressions are shown in Table 1.3.

Table 1.3 Relationship between the elastic modulus and the relative density for different unit cells. Analytical relationships are indicated by *

Study	Unit cell	Relationship
Gibson and Ashby (1999) *	General	$\frac{E_{ap}}{E_s} = C_1 \rho_r^2$
Wang and McDowell (2004) *	Simple cubic	$\frac{E_{ap}}{E_s} = \frac{\rho_r}{2}$
Babaei et al. (2012) *	Rhombic dodecahedron	$\frac{E_{ap,dir1}}{E_s} = \frac{\rho_r^2}{3\sqrt{3}}$ $\frac{E_{ap,dir2}}{E_s} = \frac{3\rho_r^2}{3\sqrt{3} + \rho_r}$
Maalej et al. (2013) *	Tetrakaidecahedral	$\frac{E_{ap}}{E_s} = \frac{4\sqrt{2}\rho_r^2}{6 + 8\sqrt{2}\rho_r}$
Ahmadi et al. (2014) *	Diamond	$\frac{E_{ap}}{E_s} = (1 - \rho_r)e^{-2.376\rho_r}$
Hazlehurst et al. (2013)	Simple cubic	$\frac{E_{ap}}{E_s} = \frac{1 - \rho_r^2}{3.85 + 1.41\rho_r}$
Parthasarathy et al. (2010, 2011)	Simple cubic	$E_{ap} = \rho_r^2$
Herrera et al. (2014)	Diamond	$E_{ap} = (L_{UC}/\phi_s)^{-3.411}$
Note: C_1 : constant; dir : direction; E_{ap} : apparent elastic modulus, E_s : elastic modulus of the solid material, L_{UC} : unit cell length; ϕ_s : strut diameter; ρ_r : relative density		

1.4.4.2 Numerical modeling

The previous relationships allow researchers to estimate the expected mechanical behavior of porous materials; however it has been shown that two samples with similar porosity, but obtained with different combinations of strut and pore dimensions, can yield different

apparent elastic modulus (Parthasarathy, et al. 2010, 2011). Therefore, the previously presented formulae do not always adequately represent the relationship between the mechanical properties and the geometrical parameters. In contrast, numerical models (i.e. finite element) simulate particular unit cell geometries and geometrical parameters overcoming such limitation. Furthermore, they show the advantage of providing detailed information about the stresses and strains in the porous material (Campoli, et al. 2013).

Several approaches exist for the finite element (FE) modeling of porous materials. In terms of the finite elements that are employed, the models can be divided into continuum (solid FE) and beam models (Figure 1.16). In terms of the size, models can represent an infinite media or have finite size, being thus subjected to specific boundary conditions.

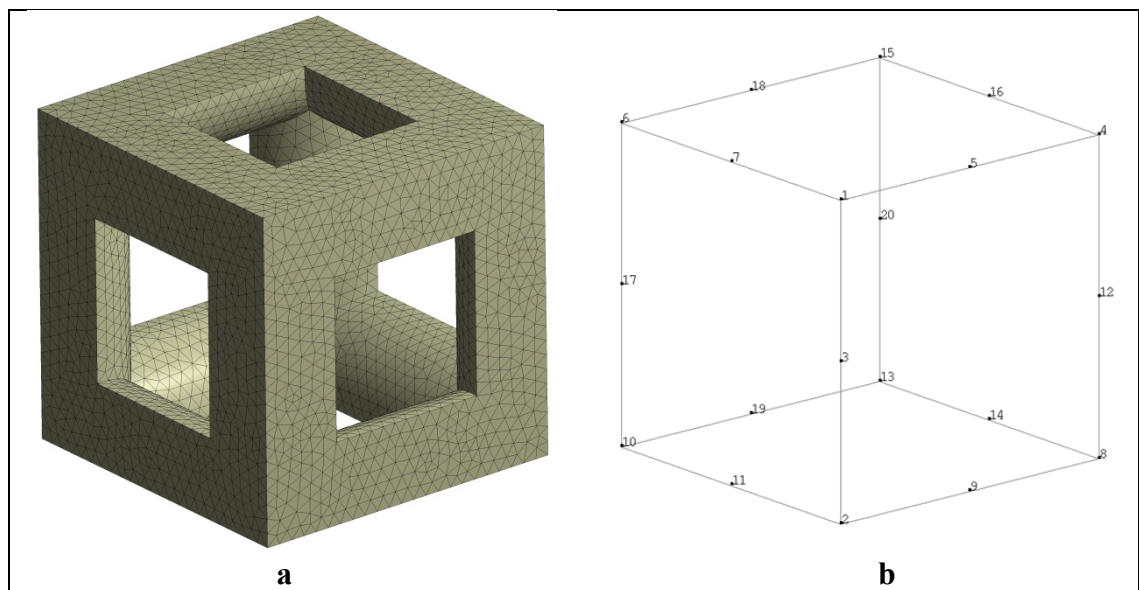


Figure 1.16 Simple cubic unit cell: (a) continuum model (solid FE elements); (b) 3-node beam model (1 element per strut)

In beam models, the struts of the porous material are represented by lines and beam finite elements are used (see e.g. Onck, et al. (2001), Luxner, et al. (2005), Gümruk and Mines (2013), Smith, et al. (2013)). This approach shows little computational cost; on the other hand, limited information is given about the mechanical behavior at the mesoscale. In

addition, the precision of the results, compared to analytical solutions, decreases as the length-to-thickness ratio diminishes.

In continuum models, the struts of the material are modeled with their volume and continuum (solid) finite elements are employed (see e.g. Luxner, et al. (2005), Arabnejad Khanoki and Pasini (2013), Gümruk and Mines (2013), Smith, et al. (2013), Parthasarathy, et al. (2011), Herrera, et al. (2014)). This approach may result in large computational cost, but it provides greater detail about the mechanical behavior at the mesoscale (i.e. stresses and strains in the struts); and the length-to-thickness ratio of the struts does not affect the accuracy of the results. Therefore, this it is usually considered as the reference approach (Luxner, et al. 2005).

Beam and continuum models have shown to provide close results in terms of the mechanical behavior of porous materials (Luxner, et al. 2005, Gümruk and Mines 2013). The differences between both approaches have been reported to be dependent on the unit cell geometry (Luxner, et al. 2005). In addition, although continuum models may provide closer results to analytical solutions, the difference with experimental data has been reported to be around 30% compared to 5% for beam models for reinforced body centered cubic unit cells (Smith, et al. 2013).

Concerning the model size, some researchers have taken advantage of the repeating (periodic) characteristics of porous materials and the fact that the mesoscale is much smaller than the macroscale, in order to consider only a unit cell in their models (Babaei, et al. 2012, Vigliotti and Pasini 2012, Arabnejad Khanoki and Pasini 2013, El Ghezal, et al. 2013, Maalej, et al. 2013). To this end, periodic boundary conditions are applied and the material is considered an infinite media. The apparent mechanical properties are obtained by averaging the mechanical properties at the mesoscale over the whole volume of the unit cell (Kouznetsova 2002). Results have shown that this approach can provide results close to analytical models, with the advantage of low computational cost. However, differences of 6.25% (Vigliotti and Pasini 2012) and up to 20% (Luxner, et al. 2005) have been computed

between this approach and the explicit modeling of the porous material, depending on the unit cell geometry. Indeed when the dimensions at the mesoscale are similar to the macroscale (i.e. the porous material has small number of unit cells), this approach can provide wrong results (Kouznetsova 2002, Vigliotti and Pasini 2012).

Other researchers have explicitly modeled the whole porous material, having a finite size given by a certain number of unit cells in each spatial direction (Luxner, et al. 2005, Adjari, et al. 2008, Hazlehurst, et al. 2014, Herrera, et al. 2014). In this case, the effective mechanical properties are obtained from the macroscopic forces and displacements, as previously described in section 1.4.4. Results obtained with these models are also in accordance with analytical expressions, and they tend to converge to the infinite media approach when the sample size (i.e. number of unit cells) is increased (Onck, et al. 2001, Campoli, et al. 2013, Dai and Zhang 2009, Coelho, et al. 2015). On the other hand, this approach overcomes the limitations of the infinite media approach for comparable mesoscale and macroscale sizes, since the effect of particular boundary conditions is captured. In addition, this approach allows for the replication of experimental testing conditions (Luxner, et al. 2005). On the counterpart, the computational cost is increased and results are influenced by the boundary conditions, thus when determining the apparent mechanical behavior of the material (i.e. without the influence of boundary conditions) the choice of the sample size must be done carefully. The finite element modeling approach (beam or continuum and sample size) constitutes the subject of the first journal article of this thesis, presented in 0.

1.4.4.2.1 Effect of manufacturing irregularities

Although the previously presented models may produce results close to analytical models, the correspondence with experimental data is much more limited. The elastic modulus computed with computational models has been found to be up to 10 times larger than experimental data for simple cubic unit cell (Parthasarathy, et al. 2011), whereas differences up to 30% have been computed with diamond unit cells (Herrera, et al. 2014). This has

motivated researchers to investigate the influence of manufacturing irregularities on the mechanical behavior of porous materials (Luxner, et al. 2007, Luxner and Pettermann 2009, Luxner, et al. 2009, Campoli, et al. 2013, Hazlehurst, et al. 2013, Karamooz Ravari and Kadkhodaei 2015). This matter constitutes the subject of the second journal article of the present thesis, presented in chapter CHAPTER 4.

1.5 Summary

Different attempts have been made to improve hip implants by optimizing their shape or their mechanical properties. Additive manufacturing allows for the production of well-ordered porous materials, for which the mechanical properties are dependent on their geometrical parameters at the mesoscale. Experimental mechanical tests and analytical deductions have been used in an attempt to describe this dependence. On the other hand, computational (finite element) models can provide detailed information about the mechanical behavior at the macro and mesoscales, with little cost and time consumption. The computational model approach (e.g. beam or continuum, finite or infinite model size) is not clear yet. In addition, the mechanical behavior predicted with computational models is often far from experimental data.

CHAPTER 2

HYPOTHESIS, OBJECTIVES AND STRUCTURE OF THE THESIS

2.1 Problem statement

In the previous chapter, it has been shown that one of the most common causes for hip implant failure is aseptic loosening. It is believed that stress shielding, caused by the presence of a stiff implant, can contribute to bone resorption that may lead to loosening of the implant. Moreover, it has been suggested that this bone resorption due to stress shielding can complicate an eventual revision arthroplasty. On the other hand, interfacial stresses are also a cause for concern, since large interfacial stresses increase the risk of interfacial failure and pain. Stress shielding and interfacial stresses have been found to be dependent on the implant shape and material properties: more flexible implants reduce stress shielding but result in less optimal interfacial stress distribution; on the other hand, the implant shape can also critically affect both factors. This has led some authors to propose strategies for improving the mechanical compatibility of the stems by either optimizing their shape or by considering a functional gradation of the mechanical properties throughout the implant.

Nowadays, additive manufacturing offers the capability of not only fabricating the optimized implant shapes, but also of achieving the optimized functional gradation of mechanical properties. In this way, porous materials can be produced with high degree of control over the geometrical parameters at the mesoscale. This allows for the tailoring of their mechanical properties. To this end, several authors have tried to express the relationship between the mesostructure and mechanical properties for porous materials. However, in general these relationships cannot fully predict the mechanical behavior.

Numerical analysis (using finite element, FE) of porous materials have been used in an attempt to obtain detailed information about their mechanical behavior, however the modeling approach is not clear yet. Questions arise whether to use continuum or beam finite elements and also whether a homogenized approach with the material considered as infinite

media is the best choice. More importantly, FE models show results that are in general far from experimental data. This has been explained by the manufacturing irregularities that arise during the production of porous materials. Up to now, no model has succeeded in finding adequate precision compared to experimental data.

2.2 Hypothesis and objectives

The basic hypothesis of this thesis is that it is possible to improve the mechanical compatibility of implants by 1) optimizing their shape and 2) optimizing the functional gradation of the material properties of the stem, which can be obtained with porous materials produced by additive manufacturing. The main objective of this thesis, which derives from the previous statement, is **to design hip implants having optimized shape and functionally graded material properties, with the goal of improving their mechanical compatibility with bone**. Such implants could be produced by additive manufacturing technologies, which means that few shape restrictions would need to be applied and that the functional gradation of mechanical properties could be obtained by means of porous materials with well-controlled mesostructure. Numerical (finite element) models will need to be developed to accurately simulate and predict the mechanical behavior of porous materials, and to design the mechanically compatible hip stems.

This main objective is attained by means of three specific objectives:

- The first specific objective is **to investigate different finite element modeling approaches to simulate porous materials**. As presented in section 1.4.4.2, FE models of porous materials can consider beam or continuum elements, and can represent the whole porous material (finite size models) or only the basic repeated unit cell (infinite media approach). Although beam and continuum FE models have been compared (e.g. Luxner, et al. 2005, Smith, et al. 2013) as well as finite size and infinite media approaches (e.g. Onck, et al. 2001, Dai and Zhang, 2009 Campoli, et al. 2013), no detailed comparison explaining the advantages and disadvantages of

these choices has been found. Furthermore, no cost-effective FE model has been proposed for porous materials.

Therefore with this first specific objective, the two FE modeling approaches (beam and continuum) will be evaluated and the influence of the sample size will be assessed and compared to the infinite media approach. The results of these analyses resulted in the first journal article, entitled “*Finite element modelling approaches for well-ordered porous metallic materials for orthopaedic applications: cost effectiveness and geometrical considerations*”, and published in *Computer Methods in Biomechanics and Biomedical Engineering* in August 2015.

- The second specific objective is **to evaluate the effects of manufacturing irregularities of porous materials in the accuracy of computational models compared to experimental data**. As presented in section 1.4.4.2.1 large differences in the mechanical behavior obtained with FE models and experimental data exist, which can be explained by the inherent manufacturing irregularities of porous materials. Different approaches have been suggested to enhance the correlation of FE models with experimental data: considering beam FE models with varying cross sections (Campoli, et al. 2013), obtaining the equivalent mechanical properties of an irregular strut (Karamooz Ravari and Kadkhodaei 2015), or decreasing the stiffness of a certain number of elements of the model (Hazlehurst et al., 2013). Nevertheless, these approaches have either resulted in limited improvement in the FE-experimental correlation or they were not based on experimental measurements of the manufacturing irregularities.

Therefore, this second specific objective aims at identifying, measuring, and including the main manufacturing irregularities of porous materials in the FE models. The mechanical behavior computed with different manufacturing irregularities was evaluated and compared to experimental data in order to determine the combination that yields the closest results to experimental data. This resulted in the second journal

article, entitled “*Finite element modeling of manufacturing irregularities of porous materials*”, and published in Biomaterials and Biomechanics in Bioengineering in March 2016. In addition, an article (third author) entitled “*Image analysis characterization of periodic porous materials produced by additive manufacturing*” has been published in January 2016 in the Journal of Materials Design. My contribution to this publication has been to design the samples to be produced and to help with the identification of the most determinant irregularities to be characterized.

- The third specific objective is **to develop an optimization approach for hip stems having functionally graded material properties through porous materials**. As presented in section 1.3.2 two methodologies have been proposed to improve the mechanical compatibility of hip implants: 1) optimization of their shape (e.g. Fernandes, et al. 2004, Chanda, et al. 2015) or 2) optimization of the functional gradation of their mechanical properties (e.g. Kuiper and Huiskes 1992, Arabnejad Khanoki and Pasini 2012). However, the combination of these two approaches has not been found. Furthermore, when designing functionally graded implants, the manufacturing irregularities are usually not taken into account and the optimization of the stem (macroscale) and the porous material (mesoscale) are usually coupled, making it difficult to introduce changes in the porous material afterwards.

Therefore, this third specific objective aims at finding in a first step the gradation of the mechanical properties that optimizes the load transfer to the bone (i.e. minimizes stress shielding and interfacial stresses). In a separate second step, the models developed in the previous first and second specific objectives (including manufacturing irregularities) are used to find the geometrical parameters of the porous materials that allow obtaining the desired gradation in the mechanical properties throughout the hip stem. This resulted in the third journal article, entitled “*Numerical design of hip stems with optimized shape and functionally graded material properties by means of additive manufactured porous materials*”, and submitted to the Journal of Biomechanics in April 2016. Additionally, an article (first

author) entitled “*On the 2D simplification of 3D bone-implant systems: application to a hip stem*” has been accepted for publication on the Journal of Biomechanical Engineering. My contribution to this publication has been to perform the 2D simulations, establish the comparisons with the 3D reference model and write the manuscript.

CHAPTER 3

ARTICLE 1. FINITE ELEMENT MODELLING APPROACHES FOR WELL-ORDERED POROUS METALLIC MATERIALS FOR ORTHOPAEDIC APPLICATIONS: COST EFFECTIVENESS AND GEOMETRICAL CONSIDERATIONS

Fernando Quevedo González¹ and Natalia Nuño¹

¹Département de Génie de la Production Automatisée, Laboratoire de recherche en imagerie et orthopédie, École de technologie supérieure, 1100 Notre-Dame Ouest, Montréal, Québec, Canada H3C 1K3

Article published in the journal « Computer Methods in Biomechanics and Biomedical Engineering, Taylor & Francis », 2015, **19**(8): 845-854

3.1 Abstract

The mechanical properties of well-ordered porous materials are related to their geometrical parameters at the mesoscale. Finite element analysis (FEA) is a powerful tool to design well-ordered porous materials by analysing the mechanical behaviour. However, FE models are often computationally expensive. This article aims to develop a cost-effective FE model to simulate well-ordered porous metallic materials for orthopaedic applications. Solid and beam FE modelling approaches are compared, using finite size and infinite media models considering cubic unit cell geometry. The model is then applied to compare two unit cell geometries: cubic and diamond. Models having finite size provide similar results than the infinite media model approach for large sample sizes. In addition, these finite size models also capture the influence of the boundary conditions on the mechanical response for small sample sizes. The beam FE modelling approach showed little computational cost and similar results to the solid FE modelling approach. Diamond unit cell geometry appeared to be more suitable for orthopaedic applications than the cubic unit cell geometry.

Keywords: well-ordered porous materials; cellular materials; finite element; mechanical properties; cost-effectiveness, orthopaedic applications.

3.2 Introduction

In total joint replacement, long-term survivorship of the arthroplasty remains a challenge (Delaunay, et al. 2008). One of the different factors compromising the long-term stability of the arthroplasty is bone resorption around the implant, believed to be due to stress shielding (Harrysson, et al. 2008, Murr, et al. 2011). Hip stems made of a homogeneous material with lower elastic modulus (E), while reducing stress shielding, produce large shear stresses at the bone-implant interface, thus increasing the risk of interface motion (Kuiper and Huiskes 1997, Arabnejad Khanoki and Pasini 2012) and pain (Huiskes, et al. 1992).

“Functionally graded implants” show a variable Young modulus (E) through the material. This E could be locally optimised to decrease stress shielding and shear stresses at the bone-implant interface (Kuiper and Huiskes 1997, Arabnejad Khanoki and Pasini 2012). The variation of E may be obtained with well-ordered porous metallic materials, also known as cellular materials or lattice materials (Heinl, et al. 2007, Arabnejad Khanoki and Pasini 2012). Formed by an arrangement of struts in the order of hundreds to thousands of microns (mesoscale), their mechanical properties are related to the geometry of this mesoscale architecture. In this way, well-ordered porous materials have shown superior and more predictable mechanical properties (i.e. stiffness and strength) than stochastic foams (Parthasarathy, et al. 2010, Arabnejad Khanoki and Pasini 2012). Therefore, in the present paper, only well-ordered porous materials formed by the repetition of a regular unit cell will be discussed.

Finite Element (FE) analysis is of great interest to study the overall (at the macroscale) and local (at the mesoscale) mechanical behaviours of porous materials. Due to the level of details needed, FE models have high computational cost. Thus, there is a need to develop cost-effective approaches to simulate these materials, and to obtain a compromise between precision and numerical cost.

One source of cost-effectiveness is the model size. Some researchers (Arabnejad Khanoki and Pasini 2012, Babaei, et al. 2012, El Ghezal, et al. 2013, Maalej, et al. 2013, Karamooz Ravari and Kadkhodaei 2015) have used infinite media FE models to investigate the mechanical behaviour of porous materials with little computational cost. This approach considers the smallest repeated unit of the porous material (unit cell), subjected to periodic boundary conditions. However, infinite media models cannot capture phenomena like deformation localization or structural irregularities at the mesoscale (Luxner, et al. 2007), and their use is not adequate when the sizes at the macroscale and mesoscale are similar (Kouznetsova 2002).

As opposed to infinite media models, finite size FE models (i.e. one or more repeated unit cells without periodic boundary conditions) are computationally more expensive, but can overcome the aforementioned limitations. The size of the model must be however carefully selected, since the influence of boundary conditions on the mechanical properties is dependent on this model size. Only few authors have investigated the effect of the model size on the mechanical behaviour of porous materials using 2D (Onck, et al. 2001, Dai and Zhang 2009) and 3D FE models (Luxner, et al. 2005, Campoli, et al. 2013, Ahmadi, et al. 2014).

Another source of cost-effectiveness is the FE modelling approach. Some authors have used solid FE models (Parthasarathy, et al. 2011, Arabnejad Khanoki and Pasini 2013, Hazlehurst, et al. 2013, Herrera et al. 2014) which include large number of elements. Others have used beam FE models (Campoli, et al. 2013, El Ghezal, et al. 2013, Ahmadi, et al. 2014, Karamooz Ravari and Kadkhodaei 2015), which are less computationally expensive, but results are less detailed and precise. However, very few have compared both (solid and beam) modelling approaches (Luxner, et al. 2005, Smith, et al. 2013).

The overall mechanical behaviour of porous materials is influenced by the unit cell geometry at the mesoscale. Only few researchers have studied this unit cell geometry effect with finite size models (Luxner, et al. 2005, Dai and Zhang 2009), and with infinite media models (Arabnejad Khanoki and Pasini 2013) under compressive loads. In addition, no study has

been found comparing different unit cell geometries under bending loads, which are closer to physiological loads supported by orthopaedic implants.

The objective of this paper is to develop a cost-effective FE model to predict the mechanical behaviour of well-ordered porous materials. Three models are compared in terms of the apparent elastic modulus under compression ($E_{ap,comp}$): a finite size beam FE model, a finite size solid FE model and an infinite size solid FE model. Then, the effect of the unit cell geometry at the mesoscale on the mechanical behaviour is investigated. Two unit cell geometries (cubic and diamond) are compared under compression and bending loads to determine an appropriate unit cell geometry for orthopaedic implants.

3.3 Materials and Methods

The geometrical parameters at mesoscale are presented. Then, the three FE modelling approaches are described. Finally, the performed FE analyses, summarized in Table 3.1, are detailed.

Table 3.1 Performed analyses

	Analysis	Unit cell geometry (mesoscale)	Model approach and size (macroscale)	FE approach	Loading	n_p
Cost-effective model	Cost-effective model size (n_p)	Cubic	Finite – cubic	Solid / beam	Comp	2-10
		Cubic	Infinite	Solid	Comp	1
	Beam-solid FE difference	Cubic	Finite - cubic	Solid / beam	Comp	8
Unit-cell geometry comparison	$E_{ap,bend}$ vs $E_{ap,comp}$	Cubic / diamond	Finite - prismatic	Beam	Comp / bend	8
	Mechanical properties	Cubic / diamond	Finite - cubic	Beam	Comp	8
	Stress distribution	Cubic / Diamond	Finite - Cubic	Solid	Comp	8
Note: Comp: compressive load; bend: bending load.						

3.3.1 Geometrical parameters at mesoscale

At the mesoscale, the unit cell has straight cylindrical struts, and contains a single pore. Thus, the number of unit cells is equal to the number of pores (n_p). Cubic (Figure 3.1 (a)) and diamond (Figure 3.1 (b)) unit cell geometries were considered.

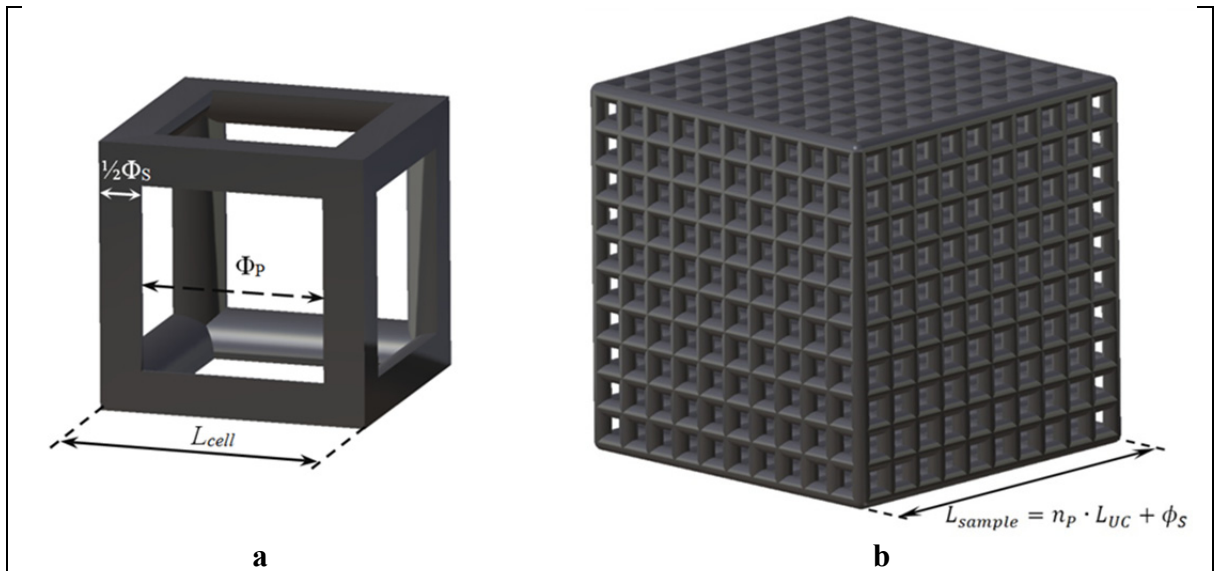


Figure 3.1 Cubic (a) and diamond (b) unit cell geometries showing main parameters

The two main geometrical parameters of the unit cell are *strut diameter* (ϕ_s , diameter of the cross section of the strut) and *pore diameter* (ϕ_p , 2D projection of the diameter of the biggest sphere that can be inscribed in the pore). These define the unit cell length for the cubic ($L_{cell,cubic}$) and the diamond ($L_{cell,diamond}$) unit cell geometries as shown in Equations (3.1) and (3.2).

$$L_{cell,cubic} = \phi_p + \phi_s \quad (3.1)$$

$$L_{cell,diamond} = \frac{4}{\sqrt{3}}(\phi_p + \phi_s) \quad (3.2)$$

The mechanical behaviour of well-ordered porous materials is commonly analysed in terms of the relative (or apparent) density (Luxner, et al. 2005, Campoli, et al. 2013, Ahmadi, et al. 2014). Other authors (Parthasarathy, et al. 2010) prefer the porosity ($P\%$), defined as the ratio

between the pore volume (V_{pores} , mm³) and the apparent volume (V_{app} , mm³) of the unit cell. As shown in Equation (3.3), porosity can be redefined as a function of the solid volume (V_{solid} , mm³), directly measured in the CAD model, and the cell length (L_{cell} , mm).

$$P_{\%} = \left(\frac{V_{pores}}{V_{app}} \right) \cdot 100 = \left(\frac{V_{app} - V_{solid}}{V_{app}} \right) \cdot 100 = \left(1 - \frac{V_{solid}}{(n_p \cdot L_{cell})^3} \right) \cdot 100 \quad (3.3)$$

The relative density (or the porosity) can be written in terms of the aspect ratio of the struts (length to thickness ratio) (Gibson 2005). The slenderness ratio of the struts (S_R) is another interesting parameter as it considers the material properties in addition to the aspect ratio and has also been related to the failure mechanism of the struts (Queheillalt and Wadley 2005). This dimensionless parameter expresses the relation between a strut diameter (ϕ_S) and its length ($\phi_S + \phi_P$), as shown in Equation (3.4).

$$S_R = \frac{G \cdot A \cdot L^2}{E \cdot I} \quad (3.4)$$

Where “ G ” (GPa) is the shear modulus, “ A ” (mm²) is cross-sectional area and “ L ” (mm) is the strut length, “ E ” (GPa) is the Young’s modulus and “ I ” (mm⁴) is the inertia moment of the strut cross section. Thus, a single value for S_R may define different combinations of strut and pore diameters. In the present study, the S_R and $P_{\%}$ will be used.

3.3.2 Finite element (FE) modelling approaches

Meshing and simulations were done in ANSYS v14 (Ansys Inc., Canonsburg, PA). Ti6Al4V material was considered and modelled as perfectly elastic ($E=120$ GPa, $\nu=0.3$) (ARCAM AB n.d.). Static analyses, accounting for large deformations, were performed. The three models were considered: finite size model with solid elements (finite size solid model), finite size

model with beam elements (finite size beam model), and infinite size model with solid elements (infinite media model), and are described below.

3.3.2.1 Finite size solid FE model

The 3D-geometry was generated in CATIA v5 (Dassault Systems, Waltham, MA). Symmetry was used and only a quarter of the porous material was analysed (Figure 3.2). Meshing was done with 10-node tetrahedral elements with quadratic displacement behaviour. As an example, for a 10-pore solid model having cubic unit cell geometry with $S_R=34$ ($\phi_p=600\mu\text{m}$ and $\phi_s=450\mu\text{m}$; $P\%=68\%$), mesh had 4.5 million elements considering symmetry. Boundary conditions consisted in constraining normal displacements to symmetry faces, fixing the bottom surface and applying an axial displacement (Δu) to the top face to perform a uniaxial compression (Figure 3.2). The resulting force (F) and the apparent elastic modulus in compression ($E_{ap,comp}$) were obtained as shown in Equation (3.5).

$$E_{ap,comp} = \frac{F}{\Delta u \cdot (n_p \cdot L_{cell})} \quad (3.5)$$

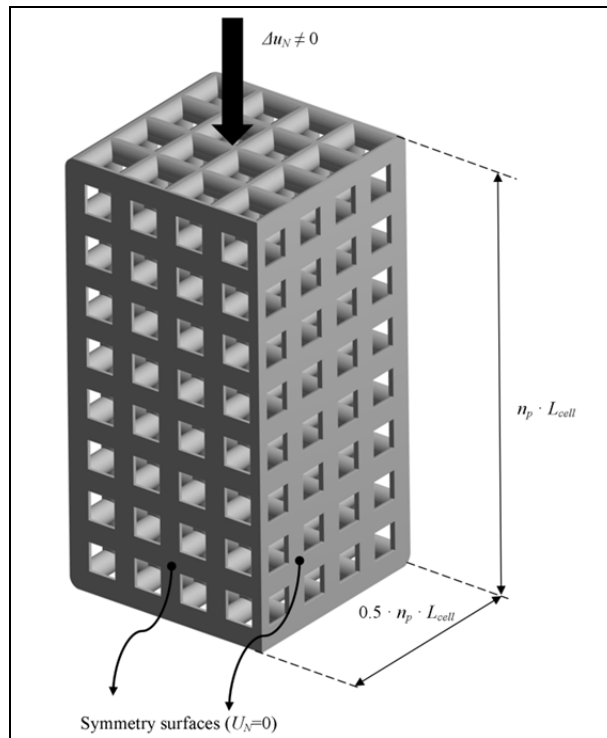


Figure 3.2 Symmetry surfaces and loading application of the solid FE model

3.3.2.2 Finite size beam FE model

The 3D geometry was done in ANSYS v14 APDL using custom subroutines. Each strut was represented by a line located at its axis of revolution. Lines were meshed with four 3-node Timoshenko beam elements with quadratic displacement behaviour, which allow analysing moderately thick struts. This resulted in 14520 elements for the 10-pore beam model, which represents more than 100 times less than the solid FE model. Circular cross section with a constant diameter, equal to ϕ_s , was considered. Boundary conditions consisted in fixing the bottom face nodes and applying an axial displacement (Δu) to the top face nodes. From this displacement and the reaction force obtained from the bottom face nodes, the $E_{ap,comp}$ was computed (Equation (3.5)).

3.3.2.3 Infinite media model

This approach considered a single unit cell. The 3D geometry was generated in CATIA v5 (Dassault Systems, Waltham, MA). Meshing was done with 10-node tetrahedral elements with quadratic displacement behaviour. To simulate the infinite media, periodic boundary conditions were applied to the unit cell by constraining each pair of opposite faces to deform in the same way (Figure 3.3). This is done by generalizing the 2D expressions from (van der Sluis, et al. 2000) to 3D, which result in the Equations (3.6) - (3.8).

$$u_{12} - u_{V2} = u_{11} - u_{V1} ; \quad (3.6)$$

$$u_{22} - u_{V4} = u_{21} - u_{V1} ; \quad (3.7)$$

$$u_{32} - u_{V5} = u_{31} - u_{V1} ; \quad (3.8)$$

Here u represents the 3D displacement vector ($u=[u_x, u_y, u_z]$). Vertex V1 was fixed in all directions ($u_{V1}^x = u_{V1}^y = u_{V1}^z = 0$) and rigid body motion was prevented by setting: $u_{V2}^y = u_{V4}^z = u_{V5}^x = 0$. A compressive displacement was applied to node 4 ($u_{V4}^y \neq 0$) and from the resulting force on this node, the $E_{ap,comp}$ was computed (Equation (3.5)).

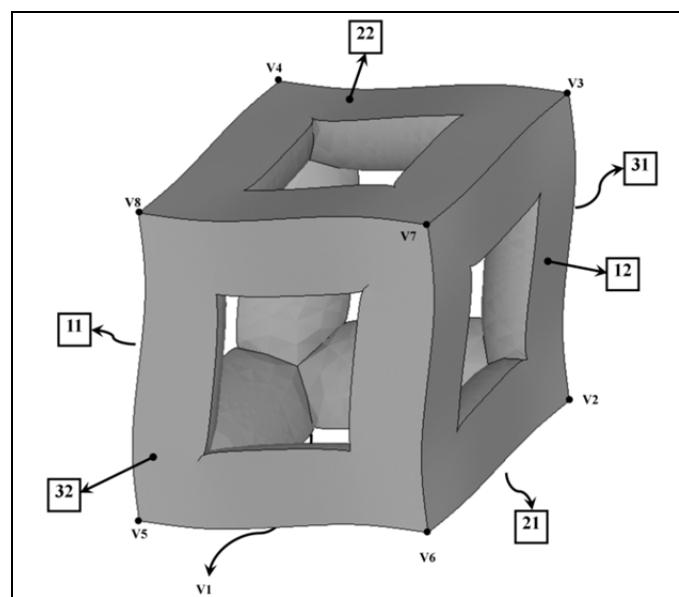


Figure 3.3 Periodic boundary conditions used for the 3D Infinite media approach

3.3.3 Performed FE analyses

Table 3.1 presents two groups of analyses performed to: 1) determine the cost-effective model (n_p and modelling approach); and to 2) investigate the effect of two unit cell pore geometries at mesoscale on the mechanical behaviour.

3.3.3.1 Determination of the cost-effective model approach

Table 3.1 shows the analyses performed to determine the cost-effective approach. At the macroscale, solid and beam finite size models had cubic shape with n_p varying from 2x2x2 to 10x10x10 pores. At the mesoscale, the cubic unit cell geometry was used. The evolution of $E_{ap,comp}$ as a function of n_p for each of the three modelling approaches (infinite media, finite solid model and finite beam model) were evaluated for 7 different slenderness ratios S_R (or $P\%$ between 55% and 98%) as shown in Table 3.2.

Table 3.2 Geometrical parameters at the mesoscale used in the FE analyses.

ϕ_S (μm)	ϕ_P (μm)	L_{cell} (μm)		S_R	$P\%$	
		Cubic	Diamond		Cubic	Diamond
450	400	850	1962	22	55	78
	600	1050	2424	34	68	85
	800	1250	2886	48	76	89
	1000	1450	3348	64	82	92
	1500	1950	4503	116	89	95
	3000	3450	7967	362	96	98
	5000	5450	12586	903	98	99

Note: ϕ_S : Strut diameter; ϕ_P : Pore diameter; L_{cell} : unit cell length; S_R : Slenderness ratio; $P\%$: Porosity

Then, using the cost-effective model size n_p selected, the $E_{ap,comp}$ obtained using the solid and beam FE models were compared (Table 3.1). The difference ($\varepsilon\%$) in $E_{ap,comp}$ for solid ($E_{ap,solid}$) and beam ($E_{ap,beam}$) was evaluated as shown in Equation (3.9).

$$\varepsilon\% = \frac{E_{ap,solid} - E_{ap,beam}}{E_{ap,solid}} \cdot 100 \quad (3.9)$$

3.3.3.2 Unit cell geometry comparison: cubic and diamond

At the mesoscale, cubic and diamond unit cell geometries were compared using three criteria (Table 3.1). The same ϕ_S and ϕ_P values for both unit cell geometries were used (Figure 3.1).

3.3.3.3 Criteria 1: similar bending and compressive behaviours

Prismatic shape models at the macroscale, better suited for bending than cubic shape models, were considered using the finite size beam FE model (Table 3.1). The previously computed cost-effective model size (n_p) was used in x and y directions, and 3 times this n_p in the z direction ($n_{p,l}$). The elastic modulus in bending ($E_{ap,bend}$) was computed from the transversal displacement (Δu) resulting from applying a transversal force (F) to the top face, while the bottom face was fixed (Eq. (3.10)).

$$E_{ap,bend} = \frac{F \cdot (n_{p,l} \cdot L_{cell})^3}{3 \cdot \Delta u \cdot I_{ap}} \quad (3.10)$$

Where I_{ap} (mm^4) is the apparent inertia of the cross section of the model, which for a squared section is Eq. (3.11).

$$I_{ap} = \frac{(n_p \cdot L_{cell})^4}{12} \quad (3.11)$$

3.3.3.4 Criteria 2: mechanical properties close to bone

Cubic shape models at the macroscale using the finite size beam FE model were considered under compression loading. $E_{ap,comp}$ was computed for 7 different S_R ($P\%$), see Table 3.2. The apparent Poisson's ratio (ν_{ap}) was computed as the ratio of the transversal strain to the axial strain.

3.3.3.5 Criteria 3: Stress distribution uniformity within struts

Due to the need of a detailed response at the mesoscale, the finite size solid FE model was employed under compression loading (Table 3.1). Cubic shape models at the macroscale with symmetry were considered. The uniformity of the Von Mises stress distribution (σ_{VM}) within the struts was evaluated qualitatively. Then, a quantitative comparison was done by comparing the ratio of the maximum stress (σ_{MAX}), obtained in the middle of the struts (excluding the zones close to the struts' junction) to the average stress (σ_{AVG}) computed as the average of stresses obtained in the middle of the struts.

3.4 Results

3.4.1 Determination of the cost-effective model approach

Figure 3.4 shows the computed apparent elastic modulus in compression ($E_{ap,comp}$) as a function of finite sample sizes (n_p) for the infinite media (horizontal dotted lines), finite size solid (plain bars) and finite size beam (stripped bars) FE modelling approaches. For the three models, for n_p constant, $E_{ap,comp}$ decreases when S_R (or $P\%$) is increased. For the infinite media approach, $E_{ap,comp}$ varies from 32.7 GPa when $S_R=22$ ($P\%=55\%$) to 0.66 GPa when $S_R=902$ ($P\%=98\%$). For the finite size solid model, $E_{ap,comp}$ varies from 39.6 GPa when $n_p=2$ and $S_R=22$ ($P\%=55\%$) to 0.78 GPa when $n_p=10$ and $S_R=902$ ($P\%=98\%$). For the finite size

beam model, $E_{ap,comp}$ varies from 47.5 GPa when $n_p=2$ and $S_R=22$ ($P_{\%}=55\%$) to 0.78 GPa when $n_p=10$ and $S_R=902$ ($P_{\%}=98\%$).

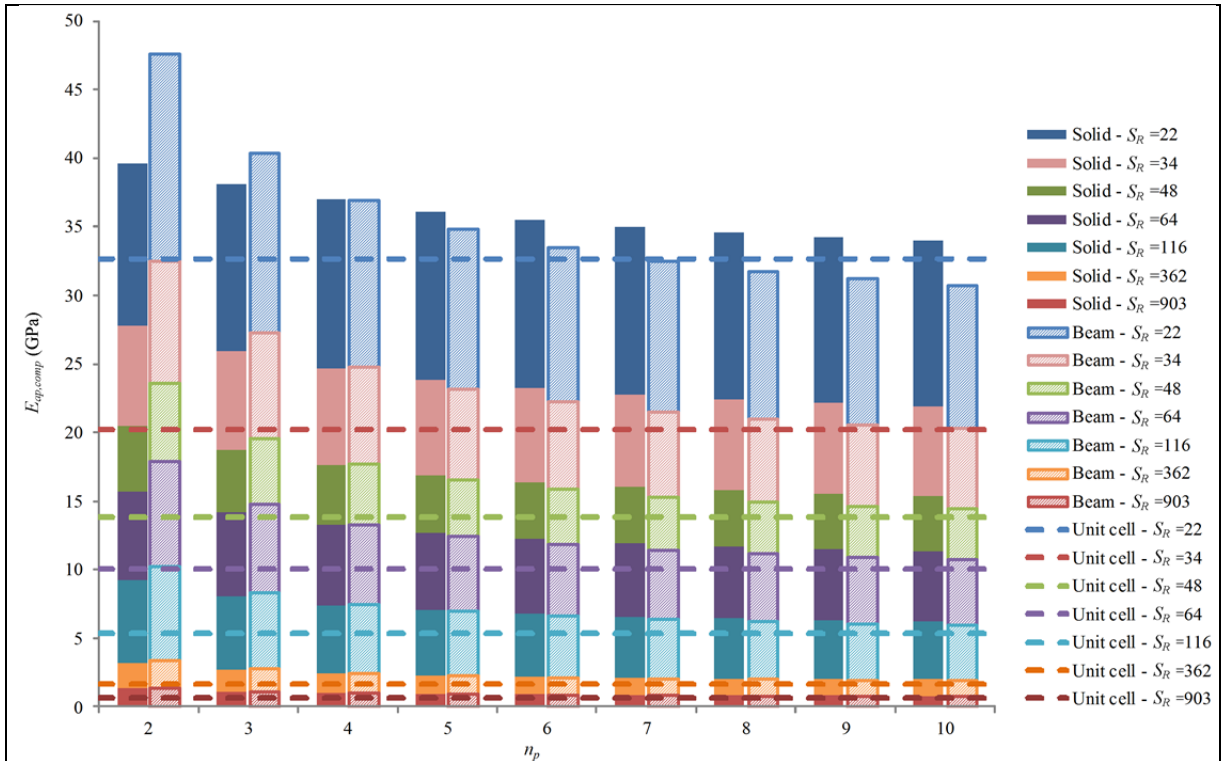


Figure 3.4 $E_{ap,comp}$ as a function of n_p (from 2 to 10) for the cubi unit cell geometry using the solid, beam and infinite media FE models ($\phi_S = 450 \mu\text{m}$)

As expected, for the infinite media approach $E_{ap,comp}$ is constant for each S_R , since it is not dependent on n_p . For both finite size models (beam and solid), computed $E_{ap,comp}$ values decrease when n_p is increased, trending to the values predicted by the infinite media approach (Figure 3.4). The decrease is more important for small S_R and for the finite size beam approach. Both finite size approaches (solid and beam) are stiffer (larger $E_{ap,comp}$) than the infinite media approach except for the finite size beam model for $S_R=22$ ($P_{\%}=55\%$) and $n_p>7$. For small sample sizes ($n_p<4$), the finite size beam model results in larger $E_{ap,comp}$ than the finite size solid model, however when the sample size is larger ($n_p>4$) the finite size solid model shows larger $E_{ap,comp}$ than the finite size beam model.

Figure 3.5 shows the absolute value of $\Delta E_{ap,comp}$ ($E_{ap,comp}$ variation when n_p is increased by 1) as a function of n_p for both finite size models (beam and solid) using cubic unit cell geometry. An intermediate S_R value of 48 ($P_{\%}=76\%$) is used. Curves are steeper for small n_p , especially for the finite size beam model (i.e. larger influence of n_p on $E_{ap,comp}$). All curves show an asymptotic decrease trending to zero as n_p increases. For $n_p > 8$, $\Delta E_{ap,comp}$ is less than 2.5% for the finite size beam model approach ($E_{ap,comp}$ decreases from 21.02 GPa to 20.62 GPa) and less than 1.5% for the finite size solid model ($E_{ap,comp}$ decreases from 15.54 GPa to 15.32 GPa). Therefore, $n_p=8$ pores is considered the cost-effective finite model size (i.e. the minimum n_p to obtain the effective $E_{ap,comp}$ of the porous material minimizing the sample size effects).

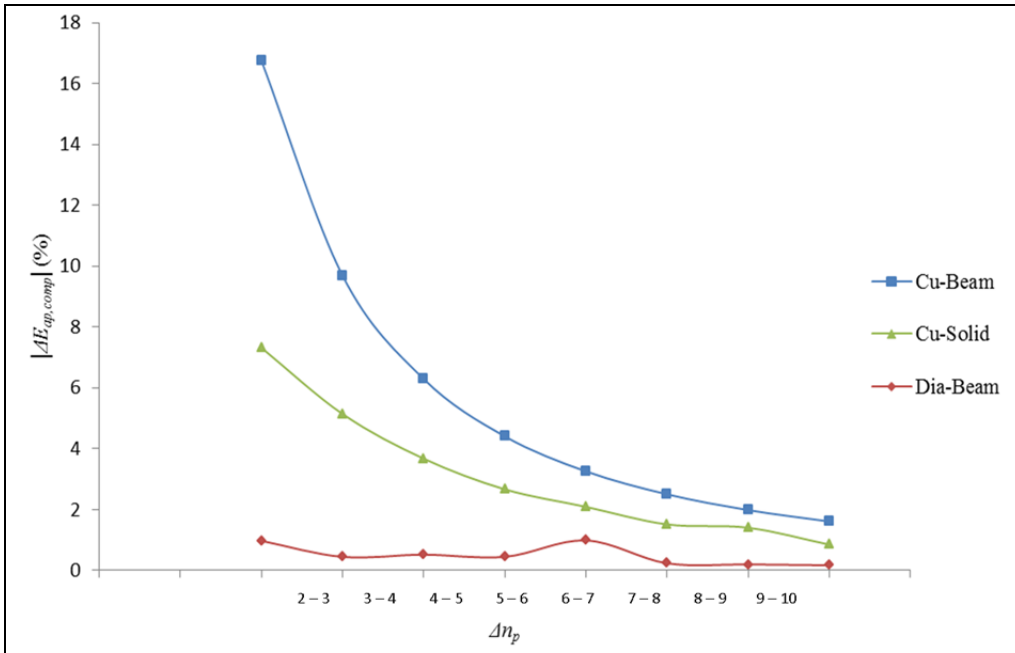


Figure 3.5 $|\Delta E_{ap,comp}|$ as a function of Δn_p (variation of $E_{ap,comp}$ for n_p increment of 1) for cubic (beam and solid FE models) and diamond beamFE model) unit cell geometries, using $S_R = 48$

Figure 3.6 shows the difference in $E_{ap,comp}$ ($\varepsilon_{\%}$, see Eq.8) as a function of S_R between finite size solid and beam models for $n_p=8$. When S_R increases, $\varepsilon_{\%}$ diminishes showing an asymptotical behaviour. The difference between both finite size models decreases from approximately 8.4% when $S_R=22$ ($\phi_S=450\mu\text{m}$ and $\phi_P=400\mu\text{m}$, $P_{\%}=55\%$), to approximately

2% when $S_R=116$ ($\phi_S=450\mu\text{m}$ and $\phi_P=1500\mu\text{m}$, $P_\%=89\%$), and to 1% when S_R is 903 ($\phi_S=450\mu\text{m}$ and $\phi_P=5000\mu\text{m}$, $P_\%=98\%$).

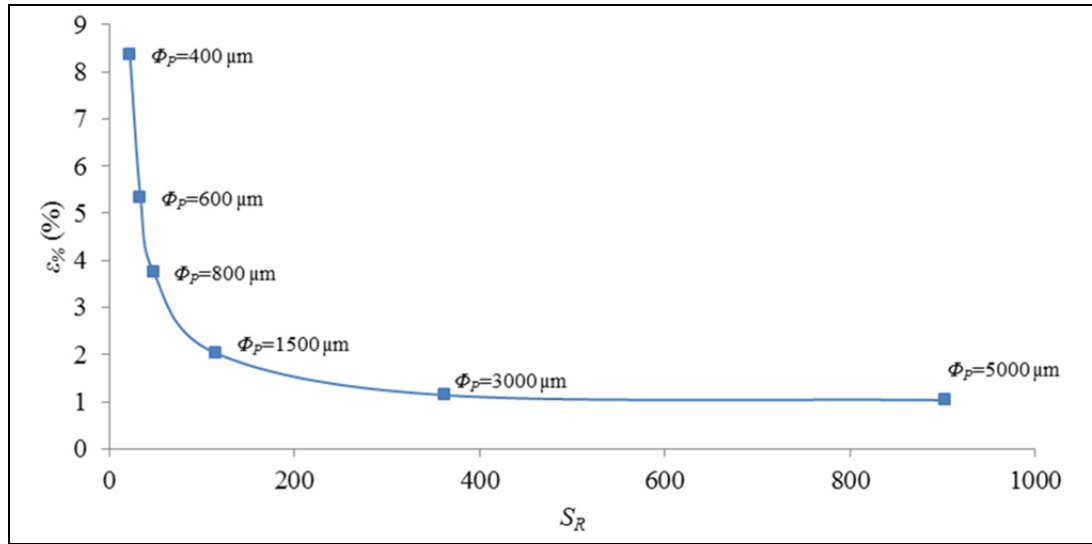


Figure 3.6 $\epsilon_\%$ (difference in $E_{ap,comp}$ as between solid and beam FE models) a function of S_R ($\phi_S = 450\mu\text{m}$) for $n_p = 8$

3.4.2 Unit cell geometry comparison: cubic and diamond

Figure 3.5 shows the absolute value of $\Delta E_{ap,comp}$ as a function of n_p for the diamond unit cell geometry with $S_R=48$ ($P_\%=76\%$) using the finite size beam model. The total $\Delta E_{ap,comp}$ increase is only 2%: from 0.69 ($n_p=2$) to 0.71 GPa ($n_p=10$). This is roughly 10 times less variation than for the cubic unit cell geometry (around 20%). The absolute value of $\Delta E_{ap,comp}$ is under 0.2% for the diamond unit cell geometry when n_p is increased from 8 to 9, also 10 times less than for the cubic unit cell geometry (around 2.5%). Therefore, the diamond unit cell geometry is less influenced by n_p (boundary conditions) than the cubic pore geometry.

3.4.2.1 Criteria 1: similar bending and compressive behaviours

Table 3.3 presents the difference in % between $E_{ap,comp}$ and $E_{ap,bend}$ for the two unit cell geometries (cubic and diamond) and different values of S_R (ϕ_P). For both unit cell geometries, the difference between $E_{ap,comp}$ and $E_{ap,bend}$ increases with S_R . The cubic unit cell geometry

shows a maximum difference between E_{ap} in bending and compression of 83.3%, while the diamond unit cell geometry shows a maximum difference of 24.2%. Therefore, the diamond geometry has more similar bending and compressive behaviours.

Table 3.3 Comparison between $E_{ap,comp}$ and $E_{ap,bend}$ for the two unit cell geometries and different S_R using $n_p=8$.

S_R	Cubic			Diamond		
	$E_{ap,comp}$ (GPa)	$E_{ap,bend}$ (GPa)	Difference (%)	$E_{ap,comp}$ (GPa)	$E_{ap,bend}$ (GPa)	Difference (%)
22	31,70	21,42	32,4	2,41	1,93	19,9
34	21,02	12,96	38,4	1,25	0,98	21,8
48	14,95	8,28	44,6	0,70	0,54	23,2
64	11,18	5,52	50,6	0,42	0,35	18,3
116	6,24	2,30	63,2	0,15	0,11	25,8
362	2,02	0,34	83,3	0,02	0,01	24,23

3.4.2.2 Criteria 2: mechanical properties close to bone

Table 3.3 shows the $E_{ap,comp}$ and $E_{ap,bend}$ for both unit cell geometries for $n_p=8$. For the diamond unit cell geometry, $E_{ap,comp}$ varies between 0.02 GPa and 2.41 GPa, and the cubic unit cell geometry between 2 GPa to 31.7 GPa. Bone's E ranges from 0.5 to 20 GPa (Parthasarathy et al. 2010). For the cubic unit cell geometry, to obtain a small $E_{ap,comp}$ of 2 GPa a porosity as high as 96% is needed, whereas for the diamond unit cell geometry, a lower porosity of 78% would be required.

Table 3.4 shows the apparent Poisson's ratio (ν_{ap}) for the cubic and diamond unit cell geometries. For the cubic unit cell geometry, ν_{ap} decreases with S_R , while for the diamond unit cell geometry it increases. In general, values for the cubic unit cell geometry are very

low (between 0.089 and 0.19), while for the diamond unit cell geometry, values are exceptionally high (between 0.437 and 0.521).

Table 3.4 Comparison of ν_{ap} for the two unit cell geometries and different S_R using $n_p=8$

S_R	22	34	48	64	116	362	903
Cubic	0,190	0,165	0,150	0,140	0,120	0,1	0,089
Diamond	0,437	0,457	0,472	0,483	0,499	0,516	0,521

3.4.2.3 Criteria 3: stress distribution uniformity within struts

Figure 3.7 shows the stress distribution within the struts for cubic and diamond unit cell geometries under compressive loading, obtained with the finite size solid model. For the cubic unit cell geometry, stress values (> 800 MPa) found in the vertical struts (Figure 3.7 (a)) were roughly 10 to 20 times higher than those found in the horizontal struts (< 90 MPa). On the contrary, similar stress levels were observed for all struts of the diamond unit cell geometry (Figure 3.7 (b)). In addition, the ratio of the maximum stress (obtained in the middle of the struts) to the average stress is around 2.75 for the cubic unit cell geometry, while for the diamond unit cell geometry it is around 1.1, indicating a more even stress distribution in the struts for this geometry.

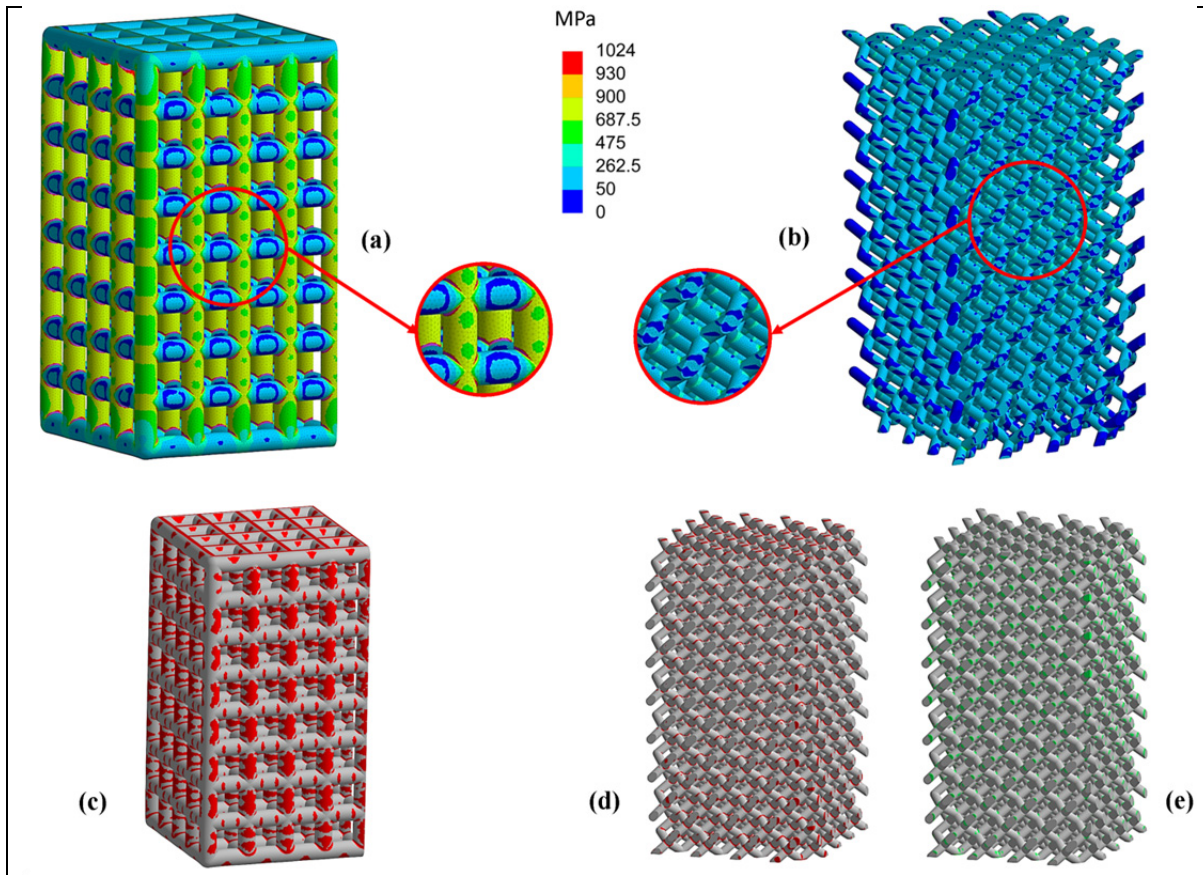


Figure 3.7 (a) Stress distribution within the struts for the cubic unit cell geometry; and (b) diamond unit cell geometry; (c) pure compression zones (in red) for the cubic unit cell geometry; (d) pure compression (in red) and (e) pure traction zones (in green), respectively, for the diamond unit cell geometry

For the cubic unit cell geometry, vertical struts showed negative maximum principal stress (red colour in Figure 3.7 (c)), indicating pure compression of the struts. For the diamond unit cell geometry neither pure compression (negative maximum principal stresses, red colour in Figure 3.7 (d)), nor pure traction (positive minimum principal stresses, green colour in Figure 3.7 (e)) was observed within the struts.

3.5 Discussion

Infinite media solid model and finite size beam and solid models having different n_p were simulated for different S_R ($P\%$). The cost-effective finite model size (n_p) and modelling approach (solid or beam) for the simulation of well-ordered porous materials were then

determined. This cost-effective model was applied to compare two unit cell geometries at the mesoscale. Results were analysed in terms of slenderness ratio, S_R and the porosity ($P\%$) as this choice is advantageous since the conclusions obtained are representative of multiple possible combinations of pore/strut diameters.

In the present article, the 2D infinite media FE model approach was extended to 3D models. Using 2D model, Arabnejad Khanoki and Pasini (2013) calculated $E_{ap,comp}$ around 10% of the bulk material for $P\%=80\%$. Using 3D model, Luxner et al. (2005) predicted around 4% of the bulk material for $P\%=90\%$. In the present study, for Ti6Al4V bulk material ($E=120$ GPa), we obtained $E_{ap,comp}=10.1$ GPa for $P\%=82\%$ ($S_R=64$) and $E_{ap,comp}=5.4$ GPa for $P\%=89\%$ ($S_R=116$) (Figure 3.4 and Table 3.2). Our results agree with these two studies.

Finite size models capture the effects of the boundary conditions, as opposed to the infinite media model approach. When n_p is small (similar sizes at the macroscale and mesoscale), the infinite media model approach underestimates $E_{ap,comp}$. This limitation does not apply to finite size models. Thus, finite size models may be preferable in orthopaedics, where parts to model may have small dimensions. The present results show that the size (n_p) of the finite size models has an effect on the $E_{ap,comp}$. The cost-effective n_p for finite size models was found to be 8 pores: incrementing the model size does not report substantial changes in $E_{ap,comp}$.

The difference in $E_{ap,comp}$ between solid and beam FE modelling approaches using the cubic unit cell geometry and cost-effective $n_p=8$, was found to be under 8.4% for any S_R . This difference was smaller for larger porosities ($P\%$). However, the solid FE model needed around 3 times more solving time than the beam FE model and 4.4 times when including the mesh generation.

Results show that cubic unit cell geometry is stiffer than the diamond unit cell geometry. However, the cubic unit cell geometry shows larger variation in E_{ap} between bending and compression (maximum of 83.3%) than the diamond unit cell geometry (maximum of

25.8%), being therefore more sensitive to force direction. Our results are in accordance with conclusions of Luxner et al. (2009), and extend the conclusions to bending cases that were not yet investigated by other researchers. In addition, mechanical properties for the diamond unit cell geometry are closer to bone than for the cubic unit cell geometry, which requires large S_R (large ϕ_P) or large porosity ($P > 70\%$ to obtain $E_{ap} = 20$ GPa) values to match bone's mechanical properties. The diamond unit cell geometry also presented a more uniform distribution of stresses within the struts. Thus based on these three criteria, we suggest using diamond unit cell geometry as an appropriate geometry at the mesoscale for bone implant applications.

3.6 Conclusion

New additive manufacturing technologies make possible the fabrication of complex-shaped porous metallic materials to design fully customized implants. Functionally graded implants could be obtained by optimizing the material properties of the implant (E) to decrease stress shielding phenomenon associated with bone resorption, while keeping low interfacial shear stresses between implant and bone.

We suggest using the finite size beam FE model as a cost-effective approach for the simulation of well-ordered porous materials. The finite size solid model may be used when more detailed information is needed. When macroscale size is larger than mesoscale, $n_p \geq 8$, finite size models provide equivalent results to the infinite media approach. When macroscale and mesoscale are of comparable sizes, $n_p < 8$, finite size models capture well the effect of boundary conditions on the mechanical response.

Diamond unit cell geometry showed more similar compressive and bending behaviours, mechanical properties closer to bone, and more uniform stress distribution. Therefore, the present results suggest using diamond unit cell geometry at the mesoscale for orthopaedic applications.

3.7 Acknowledgements

This study was supported by the Individual Discovery Grant Program from the Natural Sciences and Engineering Research Council of Canada (NSERC).

CHAPTER 4

ARTICLE 2. FINITE ELEMENT MODELING OF MANUFACTURING IRREGULARITIES OF POROUS MATERIALS

Fernando J. Quevedo González¹ and Natalia Nuño¹

¹Département de Génie de la Production Automatisée, Laboratoire de recherche en imagerie et orthopédie, École de technologie supérieure, 1100 Notre-Dame Ouest, Montréal, Québec, Canada H3C 1K3

Article published in the journal “Biomaterials and Biomechanics in Bioengineering, Techno-Press”, 2016, 3(1): 1-14

Rapport-gratuit.com
LE NUMERO 1 MONDIAL DU MÉMOIRES 

4.1 Abstract

Well-ordered porous materials are very promising in orthopedics since they allow tailoring the mechanical properties. Finite element (FE) analysis is commonly used to evaluate the mechanical behavior of well-ordered porous materials. However, FE results generally differ importantly from experimental data. In the present article, three types of manufacturing irregularities were characterized on an additive manufactured porous titanium sample having a simple cubic unit-cell: strut diameter variation, strut inclination and fractured struts. These were included in a beam FE model. Results were compared with experimental data in terms of the apparent elastic modulus (E_{ap}) and apparent yield strength ($S_{Y,ap}$). The combination of manufacturing irregularities that yielded the closest results to experimental data was determined. The idealized FE model resulted in an E_{ap} one order of magnitude larger than experimental data and a $S_{Y,ap}$ almost twice the experimental values. The strut inclination and fractured struts showed the strongest effects on E_{ap} and $S_{Y,ap}$, respectively. Combining the three manufacturing irregularities produced the closest results to experimental data. The model also performed well when applied to samples having different structural dimensions. We recommend including the three proposed manufacturing irregularities in the FE models to predict the mechanical behavior of such porous structures.

Keywords: additive manufacturing; electron beam melting; porous materials; finite element; manufacturing irregularities; mechanical properties

4.2 Introduction

Well-ordered porous metallic materials, also known as lattice materials, are formed by an arrangement of struts at the mesoscale. These structured materials are very promising in aerospace industry (Spadoni and Ruzzene 2007, Heo, et al. 2013), heat transfer (Kumar, et al. 2009, Maloney, et al. 2012) or shock absorption (Harrigan, et al. 2010), but specially in orthopedic applications (Parthasarathy, et al. 2011, Arabnejad Khanoki and Pasini 2012). The mechanical properties of these materials are dependent on the mesoscale shape (i.e. diamond, simple cubic, etc.) and dimensions (strut and pore diameters, porosity, etc.), thus can be tailored for specific needs (Luxner, et al. 2005). Moreover, mechanical properties can be varied throughout a piece, making possible to produce “functionally graded implants” that reduce stress shielding and interfacial failure risk (Kuiper and Huiskes 1997, Fraldi, et al. 2010, Arabnejad Khanoki and Pasini 2012).

Finite element (FE) modeling is a powerful tool to these design lattice materials, since overall (at the macroscale) and local (at the mesoscale) mechanical behaviors can be obtained with the required level of detail. However, the mechanical behavior (in terms of the apparent elastic modulus E_{ap}) predicted with FE models generally differ importantly from experimental data, especially in the case of metallic lattice materials. For instance, for well-ordered porous titanium material with simple cubic (SC) unit-cell produced by Electron Beam Melting (EBM), Parthasarathy *et al.* (2010) predicted as much as 10 times stiffer response with FE models (E_{ap} between 20 and 30 GPa) than experimental data (E_{ap} from 2.13 to 2.92 GPa) for porosities ranging from approximately 51% to 70%.

For other unit-cell geometries at the mesoscale, these differences are smaller. For instance, for body centered cubic (BCC) unit-cell, Smith *et al.* (2013) found around 15% difference between numerical and experimental values of E_{ap} . For diamond (D) unit-cell geometry,

Ahmadi *et al.* (2014) reported 15% difference and Herrera *et al.* (2014) an average of 27.5%. For an optimized unit-cell, Barbas *et al.* (2012) found a maximum difference of around 25% between FE and experimental E_{ap} .

The discrepancies between computational and experimental results may be caused by the manufacturing irregularities present on the physical samples, but that are usually not simulated in the FE models (Campoli, et al. 2013). In addition, most studies consider only perfectly elastic material, instead of an elastic-plastic behavior which also contributes to enlarge the differences. In this way, some parametric studies exist about the relationship between the irregularities and the mechanical behavior of well-ordered porous materials (Chen, et al. 1999, Zhu, et al. 2001, Adjari, et al. 2008, Alkhader and Vural 2008, Luxner, et al. 2009), showing the influence of irregularities in the mechanical response.

However, very few authors have compared FE results for well-ordered porous materials including irregularities with experimental data. Campoli *et al.* (2013) considered the effect of strut diameter variation and material micro-porosities at the fused solid scale of titanium porous material, with results that were closer to experimental data. Hazlehurst *et al.* (2013) assumed that 50% of the elements of a continuum FE model of CoCrMo had reduced stiffness, obtaining a stiffness decrease of around 66% compared to an idealized model. Karamooz Ravari and Kadkhodaei (2015) obtained the equivalent material properties of an irregular strut of 316L stainless steel and applied them to an idealized beam FE model of a BCC unit-cell, resulting in an E_{ap} that was approximately 91% of the experimental values. However, except from Campoli *et al.* (2013) (who directly used measured values for the strut diameter variation), in the aforementioned studies, the E_{ap} decrease from the FE model was not obtained by the direct implementation of manufacturing irregularities measured on physical samples.

Therefore, the aim of this paper is to develop a simple approach to include the geometrical irregularities in a FE model based on observations to predict the mechanical behavior of well-ordered porous metallic materials. These geometrical irregularities are inherent to rapid

manufacturing process of these materials. The objectives were to determine these irregularities directly from measurements of a physical sample made by EBM, and to include them in a beam FE model. To verify the validity of the proposed FE model, numerical results were compared to experimental data in terms of the apparent elastic modulus under compression (E_{ap}) and the apparent yield strength ($S_{Y,ap}$).

4.3 Materials and Methods

4.3.1 Experimental data

Fabrication and mechanical testing were done at the Biomechanics Institute of Valencia (IBV, Spain). The most important details of the experimental procedure are depicted below. More details may be found in (Petrović, et al. 2012).

The unit-cell and the macroscopic sample used by (Petrović, et al. 2012) are shown in Figure 4.1. At the mesoscale, simple cubic unit-cell with cylindrical struts was chosen (Figure 4.1 - a). At the macroscale, samples had cubic shape and 10 unit-cells by side (Figure 4.1 - b).

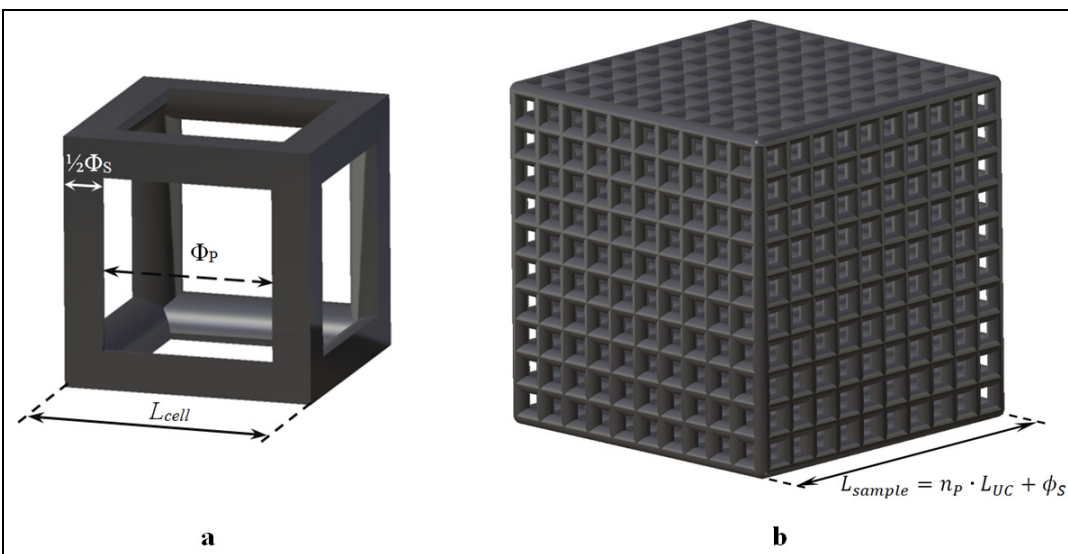


Figure 4.1 (a) Cubic unit-cell pore geometry and main parameters and (b) 10-pore sample model generated by periodic repetitions of the unit-cell

Three different sample sets with 5 samples per set (15 samples in total) of well-ordered Ti6Al4V porous material were fabricated by Electron Beam Melting (EBM). Design and measured diameters of struts (ϕ_S) and pores (ϕ_P) are shown in Table 4.1. Samples are referred to as “S” followed by the strut diameter, and “P” followed by the pore diameter (i.e. S450P700, for $\phi_S=450 \mu\text{m}$ $\phi_P=700 \mu\text{m}$). Sample marked in bold (S450P700), is used for further characterization of the other manufacturing irregularities.

Table 4.1 Design and experimental strut and pore sizes taken from Petrovic *et al.* (2012)

Sample set	Design values		Measured values	
	$\phi_S (\mu\text{m})$	$\phi_P (\mu\text{m})$	$\phi_S (\mu\text{m})$	$\phi_P (\mu\text{m})$
S450P600	450	600	666	376
S450P700	450	700	648	504
S450P800	450	800	577	681

4.3.2 FE modeling

Three types of geometrical irregularities due to the manufacturing process of the porous materials were identified at the mesoscale (Figure 4.2): strut diameter variation; strut inclination; and fractured (or nearly fractured) struts. These irregularities were implemented in the FE model by altering an idealized model (without manufacturing irregularities). In total, 8 different FE models were created and simulated in ANSYS v14.5: i) the idealized model, ii) three models including the manufacturing irregularities separately, iii) four models including the possible combinations of manufacturing irregularities.

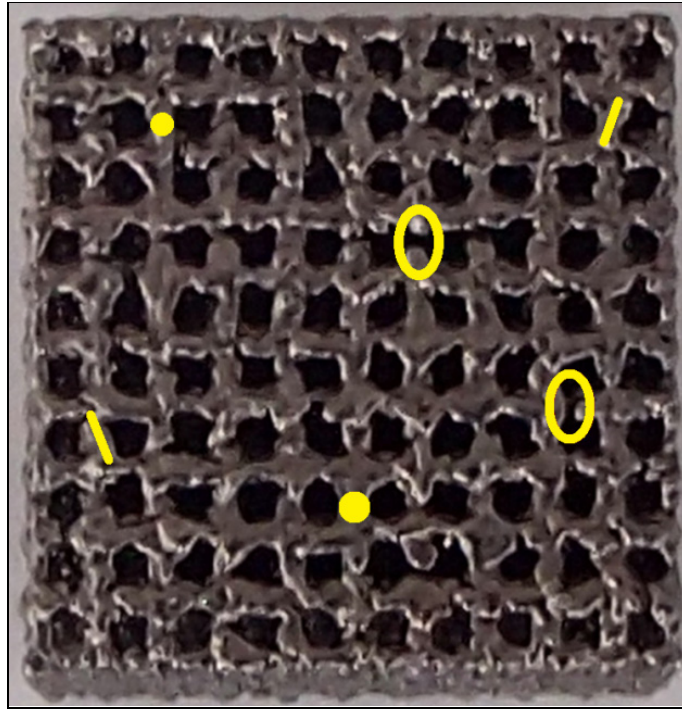


Figure 4.2 Different types of geometrical manufacturing irregularities: strut diameter variation (solid points), strut inclination (straight lines) and fractured struts (empty circles)

Material was modeled as bilinear elastic-plastic, based on Ti6Al4V-ELI data provided by the powder manufacturer (ARCAM AB n.d.). An elastic modulus of $E=120$ GPa, a Poisson's ratio of $\nu=0.3$, a yield strength of $S_y=930$ MPa and a hardening modulus of $K=1.4$ GPa were used. Struts were modeled as in (Quevedo González and Nuño, 2015), using straight lines and meshed with 3-node Timoshenko beam elements with circular cross-section and quadratic displacement behavior, which allow modeling moderately thick struts. A mesh sensitivity analysis showed that at least 2 elements (sharing a common node) were needed to mesh each strut. This resulted in 7260 elements for the idealized model.

Rigid surfaces (top and bottom) were used to simulate the experimental load application. Bonded contact (i.e. no sliding permitted) was considered, and pure Lagrange multiplier method was used. The bottom surface was fixed in all directions. A vertical displacement (i.e. normal to the surface) of 1.2 mm, similar to the one observed experimentally, was applied to the top surface.

4.3.3 Characterization and implementation of manufacturing irregularities in the FE model

A non-tested sample from the set S450P700 ($\phi_S=450 \mu\text{m}$; $\phi_P=700 \mu\text{m}$) was used. The three manufacturing irregularities and their implementation in the FE model are described below.

4.3.3.1 Strut diameter variation

The strut diameter was assumed to vary according to a normal distribution. The mean strut diameter for each sample set (μ_D) was taken as measured in the previous study of Petrović *et al.* (2012). Values are shown in Table 4.1. The maximum strut diameter variations were defined based on the maximum powder size, being of $100 \mu\text{m}$, as schematized in Figure 4.3: the maximum diameter is obtained when 2 powder particles are attached to the strut, whereas the minimum strut diameter is generated when 2 particle powders are not present. Therefore, a maximum diameter variation equal to 2 times the maximum powder size was assumed (i.e. $\mu_D \pm 200 \mu\text{m}$).

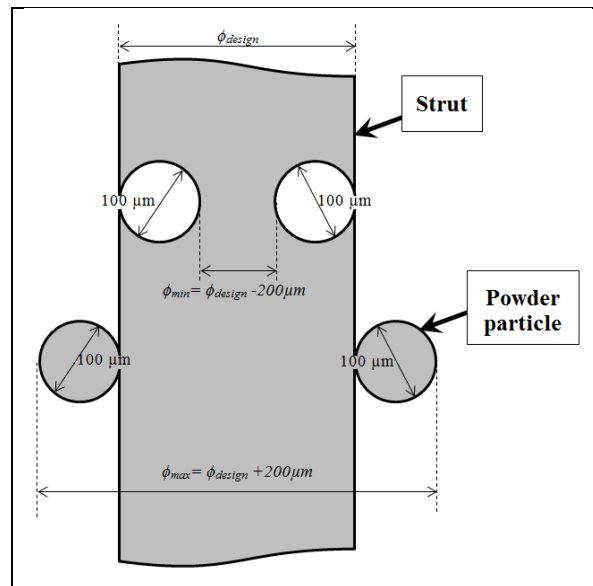


Figure 4.3 Schematization of the strut diameter variation



For the FE simulations, 9 circular beam cross-sections were created in ANSYS. Each cross-section accounted for diameters within $\pm 25 \mu\text{m}$ ($50 \mu\text{m}$ span) around its diameter value (Figure 4.4). Each strut was then assigned with a random diameter value (ϕ_{rand}), issued from a normal distribution with a standard deviation of $\sigma=75 \mu\text{m}$ ($225/3 \mu\text{m}$), chosen so that 99.8% of the values fell within $\mu_D \pm 225 \mu\text{m}$. Each assigned diameter was converted to the section number (S_n , from 1 to 9), according to Eq. (4.1).

$$S_n = \frac{\phi_{rand} - \phi_{min}}{50} + 1 = \frac{\phi_{rand} - (\mu_D - 3 \cdot \sigma)}{50} + 1 \quad (4.1)$$

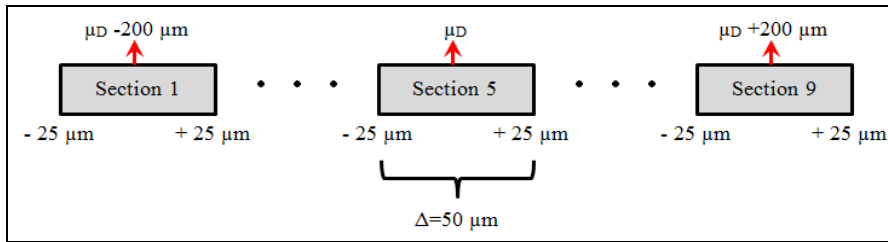


Figure 4.4 Conversion of diameter value to section number

4.3.3.2 Strut inclination

First each strut was approximated by a straight line. Then, the strut inclination angle ($Sinc$) was measured between this line and the coordinate axes for each non-fractured strut. Each sample face consists of 10 pores thus 11 struts in each direction, making at most 220 measures per face and 1320 for the entire sample. Measures were repeated twice and statistical analyses were performed to verify the repeatability of the measure (T-Student).

For the FE simulations, the extreme keypoints of each line K_1 , K_2 , K'_1 , K'_2 were shifted a random distance (Δ), issued from a normal distribution. For this purpose, the measured minimum, mean, maximum, and standard deviation inclination angles (θ) were converted to the corresponding Δ as shown in Figure 4.5. The same Δ was assumed in each direction, for a given inclination angle.

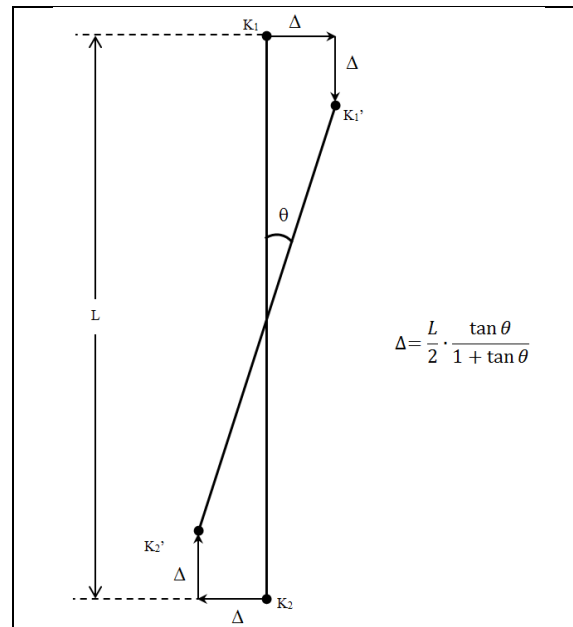


Figure 4.5 Conversion of the inclination angle θ to keypoint shifting distance

4.3.3.3 Fractured struts

The number of fractured struts (Sfr) was manually counted for each of the 6 faces of the non-tested S450P700 sample. The percentage of fractured struts ($\%Sfr$) was obtained dividing the count of fractured struts by the total number of struts (220 for each face). In the FE model, each strut was randomly assigned a value between 0 and 1, issued from a uniform distribution. Struts assigned with a number larger than the percentage of fractured struts ($\%Sfr$) were eliminated.

4.3.4 Finite Element Analyses

The 8 FE models of the sample S450P700 were simulated in ANSYS and the force-displacement curve was obtained. Then, the $\sigma_{ap}-\epsilon$ curve was computed by dividing the force and displacement by the apparent area and length of the samples, respectively. The E_{ap} was computed as the slope of the linear zone of the $\sigma_{ap}-\epsilon$ curve, and the $S_{Y,ap}$ by a parallel line at 0.2% strain. Due to their random nature, each model including manufacturing irregularities

was simulated 5 times and results were averaged. FE results were compared with the experimental data in terms of E_{ap} and $S_{Y,ap}$. The model that yielded the closest results to experimental data was applied to the other two sample sets (S450P600 and S450P800) comparing the results with experimental data.

4.4 Results

4.4.1 Characterization of manufacturing irregularities

Table 4.2 presents the strut inclination ($Sinc$) and fractured struts (Sfr) manufacturing irregularities measured on the sample S450P700. One face was discarded from the results due to the high irregularities present, thus 5 of the 6 faces of the non-tested sample were used for the characterization. Values correspond to the average of 5 faces.

Table 4.2 Measured strut inclination ($Sinc$) and fractured struts (Sfr) manufacturing irregularities of non-tested sample S450P700.

		Mean (μ)	Standard deviation	Minimum value	Maximum value
<i>Strut inclination</i>	<i>Sinc</i> (°)	0.05	8.28	-24.93	28.12
<i>Fractured struts</i>	<i>Sfr</i> (%)	13			

For $Sinc$, no statistical significant difference was found between the two measurements, indicating the repeatability of the measures.

As what concerns the strut diameter variation ($Dvar$), the mean value, as measured by Petrović *et al.* (2012), is shown in Table 4.1. Then, as explained in section 4.3.3.1, a maximum $Dvar$ of $\pm 200 \mu\text{m}$ was considered, and a standard deviation of $75 \mu\text{m}$ was used for the normal distribution.

4.4.2 Finite element analyses

First, results corresponding to the simulation of the idealized model and the 7 models including manufacturing irregularities are presented and compared with experimental data, for the sample S450P700. Then, the model that yielded the closest results to experimental data was used to analyze the other two sample sets (S450P600 and S450P800).

4.4.3 Influence of the three geometrical irregularities for set S450P700

Figure 4.6 shows, for set S450P700, the stress-strain ($\sigma_{ap}-\varepsilon$) curves corresponding to the simulations of the idealized model (from $n=1$ simulation), the 7 models including the manufacturing irregularities (average curves from $n=5$ simulations) and the experimental tests (average curve from $n=5$ tests). The experimental $\sigma_{ap}-\varepsilon$ curve (thick black, without markers) shows an initial concave zone (between $\varepsilon=0$ and $\varepsilon\approx 0.03$), followed by an apparently linear zone, and then a progressive transition to a lower slope zone (for $\varepsilon\approx 0.08$). The idealized FE model (thin, stripped black without markers) behavior is very different, with larger stress values and a marked transition from the linear elastic to the linear plastic zone (for $\varepsilon\approx 0.01$).

Including *Dvar* (dark blue with “○” markers) or *Sfr* (red with “×” markers) irregularities separately, result in similar curves to the idealized model, with lower stress values (especially for *Sfr*) and less drastic elastic to plastic transition. However, the *Sinc* irregularity (green with “+” markers) produces a drastic change of the $\sigma_{ap}-\varepsilon$ curve which becomes more similar to the experimental curve: an initial concave zone (from $\varepsilon=0$ to $\varepsilon\approx 0.015$) followed by an approximately linear zone and a progressive transition to a zone with lower slope (for $\varepsilon\approx 0.04$). Therefore, *Sinc* is the most influent irregularity.

When *Dvar* is combined either with *Sfr* (violet with “⊗” markers) or with *Sinc* (turquoise with “⊕” markers), curves are similar to those obtained considering only *Sfr* or *Sinc*, respectively. Therefore, *Dvar* is the less influent irregularity.

The combination of *Sfr* with *Sinc* (yellow with “*” markers) or the three manufacturing irregularities (grey “⊗” markers) yield the closest results to the experimental data.

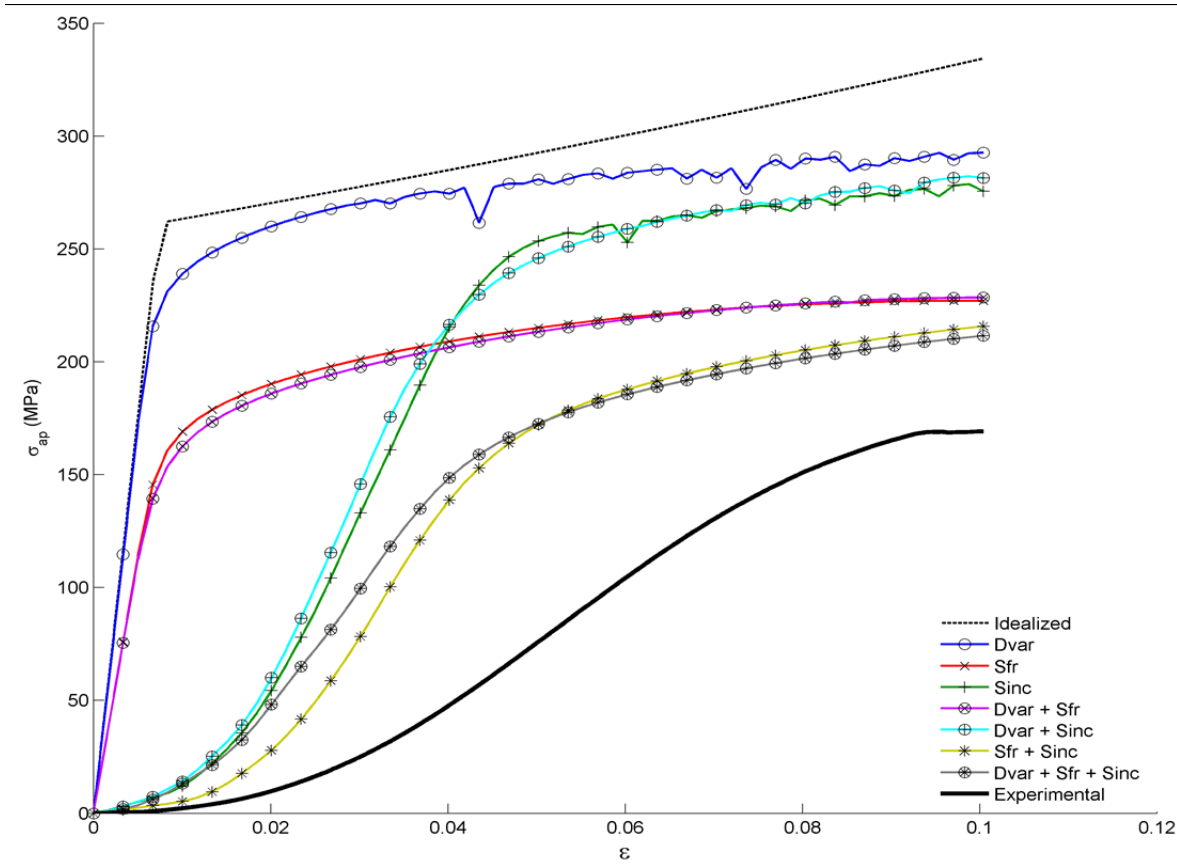


Figure 4.6 Apparent stress-compressive strain (σ_{ap} - ϵ) curves for the set S450P700 obtained with the idealized model, the different combinations of manufacturing irregularities, and the experimental tests. *Dvar*: diameter variation; *Sfr*: fractured struts; *Sinc*: inclined struts; Exp: experimental

Figure 4.7 presents, for set S450P700, the apparent elastic modulus (E_{ap} , hatched bars) and yield strength ($S_{Y,ap}$, plain bars), corresponding to the simulations considering the idealized model ($n=1$), the 7 models including manufacturing irregularities ($n=5$) and the experimental tests ($n=5$). The standard deviation is plotted as error bars. Values corresponding to $S_{Y,ap}$ are indicated in MPa while those corresponding to E_{ap} are in GPa.

The computed $S_{Y,ap}$ using the idealized model (263 MPa) is almost twice the experimental measures (146 ± 2.48 MPa). When considering *Dvar* ($S_{Y,ap} = 234 \pm 2.07$ MPa) or *Sinc* ($S_{Y,ap}$

=242±1.82 MPa) separately, similar but smaller $S_{Y,ap}$ values than the idealized model are obtained. When Sfr is considered alone, a large reduction in $S_{Y,ap}$ (166±8.22 MPa) is obtained and results are closer to experimental data. When $Dvar$ and $Sinc$ are combined, the $S_{Y,ap}$ (217±4.23 MPa) is similar and smaller than when $Dvar$ or $Sinc$ is considered alone. When Sfr is combined with any other manufacturing irregularity, $S_{Y,ap}$ is smaller but close to considering only Sfr , therefore this irregularity shows the strongest effect on $S_{Y,ap}$. The combination of the three manufacturing irregularities ($S_{Y,ap}$ =157±7.29 MPa) yields the closest results to the experimental data.

Statistical tests (one-factor ANOVA) revealed that the $S_{Y,ap}$ differences between the four models including Sfr were not statistically significant at a significance level of 0.05 (i.e. the four models can be considered as equivalents for the $S_{Y,ap}$).

The computed E_{ap} using the idealized model (35.16 GPa) is more than 10 times larger than the experimental observations (2.82±0.21 GPa). Considering $Dvar$ (E_{ap} =33.03±0.17 GPa) or Sfr (E_{ap} =22.1±1.07 GPa) separately reduces E_{ap} , but values remain one order of magnitude larger than experimental data. When $Sinc$ is considered alone, computed E_{ap} (8.33±0.25 GPa) is of the same order of magnitude than the experimental measurements. When $Dvar$ and $Sinc$ (E_{ap} =9.18±0.42 GPa) are combined, slightly larger E_{ap} values than considering $Sinc$ alone are predicted. When $Dvar$ and Sfr are combined (E_{ap} =21.83±0.48 GPa), E_{ap} is close to when Sfr is considered alone. When $Sinc$ is combined with other manufacturing irregularities, results are smaller and always close to considering $Sinc$ alone, therefore this irregularity shows the strongest effect on E_{ap} . The best results are also obtained when the three manufacturing irregularities are combined (E_{ap} =5.41±0.41 GPa).

Statistical tests (T-Student) revealed that the differences between all models are statistically significant except for the Sfr ($E_{ap,comp}$ =22.1±1.07 GPa) and $Dvar$ combined with Sfr (E_{ap} =21.83±0.48 GPa), which can be assumed to produce equivalent results in terms of E_{ap} .

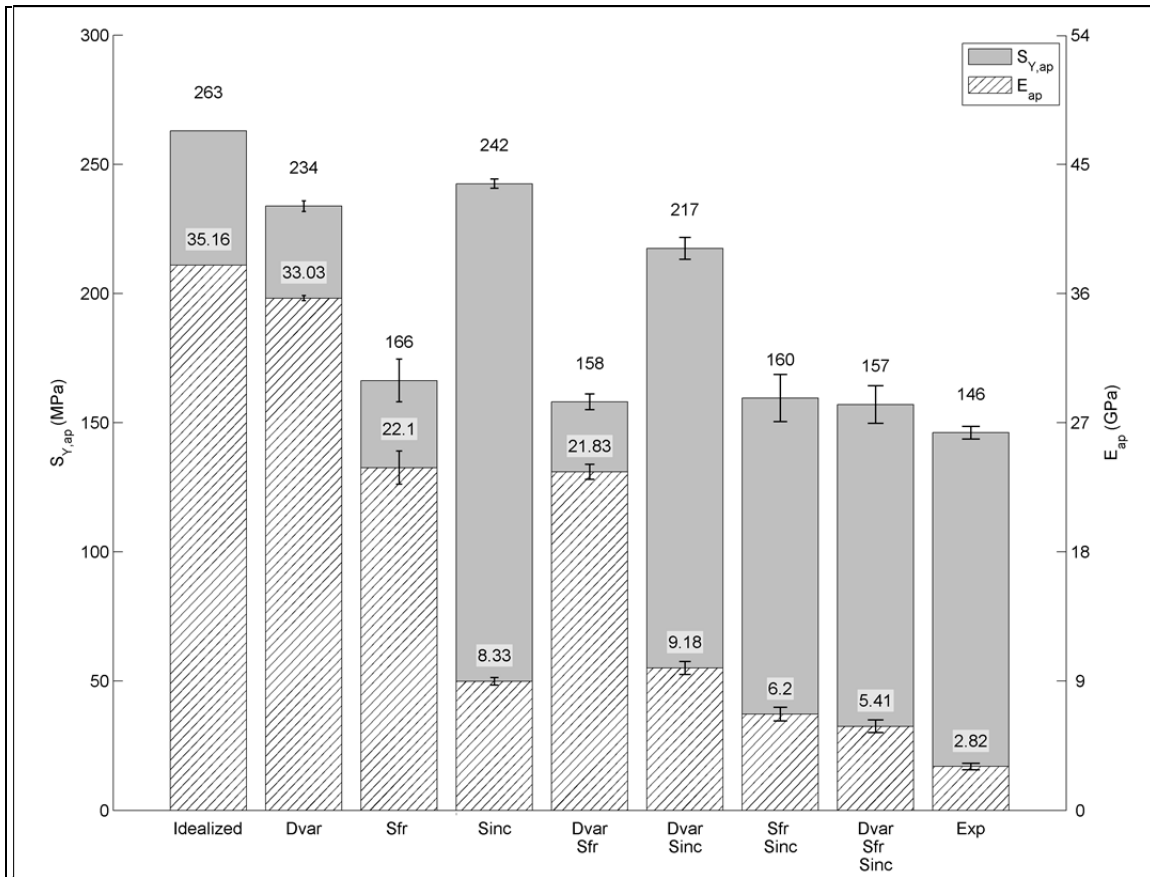


Figure 4.7 E_{ap} and $S_{Y,ap}$ obtained with the idealized model, the different combinations of manufacturing irregularities, and the experimental tests for the set S450P700. *Dvar*: diameter variation; *Sfr*: fractured struts; *Sinc*: inclined struts; Exp: experimental.

4.4.4 Simulation of the other sample sets

The methodology developed to include the three manufacturing irregularities (*Dvar*, *Sfr* and *Sinc*) was applied to the other two sample sets (S450P600 and S450P800). The *Sinc* and *Sfr* values were assumed to be the same as for the measured sample (S450P700). The strut and pore diameter values were taken from Petrović *et al.* (2012) and are shown in Table 4.1.

Figure 4.8 shows, for the three sample sets, the comparison of $S_{Y,ap}$ (plain bars) and E_{ap} (hatched bars) computed with the FE model (marked as “Sim”) and the experimental values (marked as “Exp”). The standard deviation is plotted as error bars. Values corresponding to $S_{Y,ap}$ are indicated in MPa while those corresponding to the E_{ap} are in GPa.

$S_{Y,ap}$ computed numerically is larger than experimental data for the sets S450P600 (197 ± 5.82 MPa and 174 ± 3.97 MPa, respectively) and S450P700 (157 ± 7.29 MPa and 146 ± 2.48 MPa, respectively). However for set S450P800 (i.e. the largest porosity), larger $S_{Y,ap}$ values were obtained experimentally (123 ± 3.06 MPa) than computationally (95 ± 4.09 MPa). Maximum difference is obtained for set S450P800 and minimum difference for set S450P700, which is the sample used for the characterization of irregularities.

Regarding E_{ap} , although the numerical values obtained are larger, they are of the same order of magnitude than experimental values for all three sets. Set S450P600 (i.e. smallest porosity) shows the maximum difference between computed (7.61 ± 0.64 GPa) and experimental E_{ap} (3.15 ± 0.05 GPa). Set S450P800 (largest porosity) shows the minimum difference between computed (3.65 ± 0.26 GPa) and experimental E_{ap} (2.57 ± 0.44 GPa).

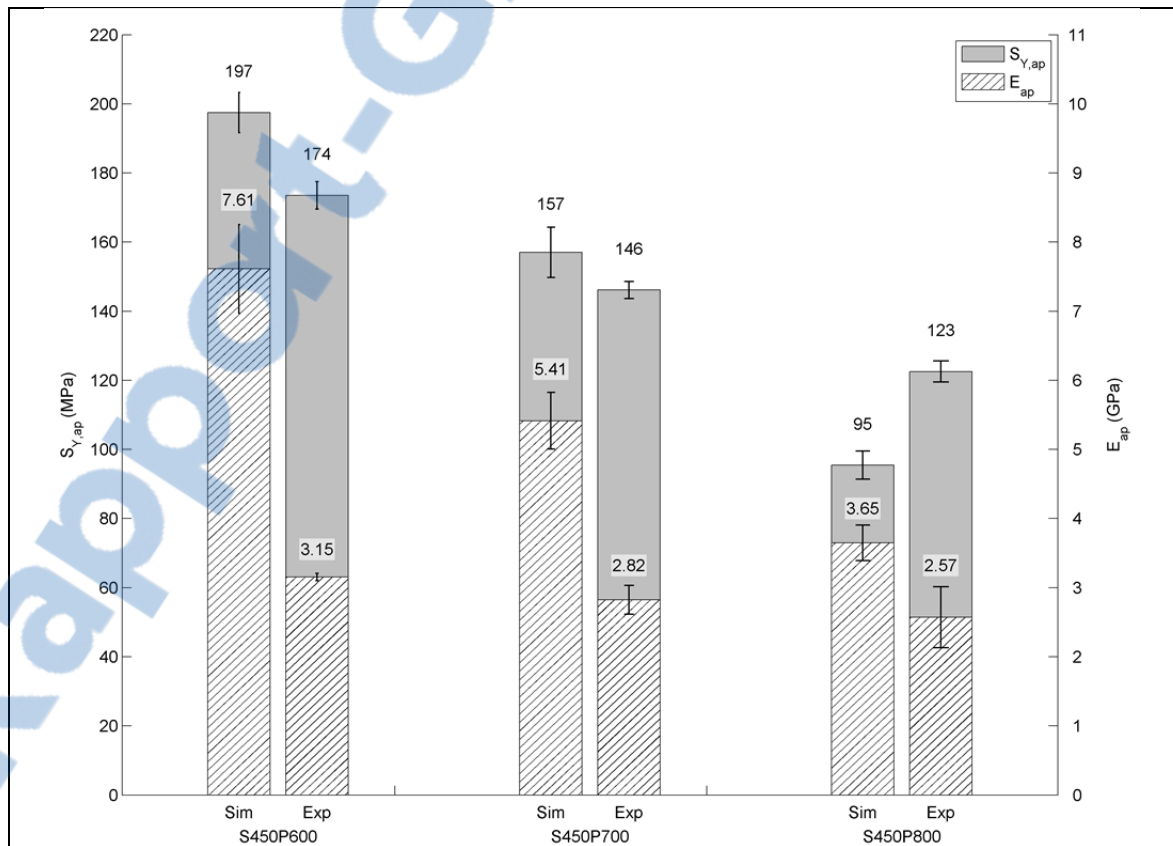


Figure 4.8 Comparison of $S_{Y,ap}$ (plain bars) and E_{ap} (hatched bars) obtained from experimental tests (Exp) and from FE simulations including the three manufacturing irregularities (Sim) for the three sets (S450P600, S450P700 and S450P800)

4.5 Discussion

In the present study, three manufacturing irregularities obtained from direct observations (strut inclination, strut diameter variation and fractured strut) were characterized on an EBM-produced sample of well-ordered porous metallic material. An idealized model and models including different combinations of these manufacturing irregularities were simulated using FE models. The results were compared with experimental data in terms of the apparent stress-strain curve ($\sigma_{ap}-\varepsilon$), the apparent elastic modulus (E_{ap}) and the apparent yield strength ($S_{Y,ap}$).

For the sample S450P700 (strut diameter of 450 μm and pore diameter of 700 μm), including the three manufacturing irregularities in the FE models resulted in a predicted $\sigma_{ap}-\varepsilon$ curve similar to the experimental one. In addition, the E_{ap} was reduced compared to an idealized model from 35.16 GPa to 5.41 ± 0.41 GPa which is a value close to the experimental one of 2.82 ± 0.21 GPa. The same was observed for the $S_{Y,ap}$, which decreased from 263 MPa to 157 ± 7.29 MPa, much closer to the experimental value of 146 ± 2.48 MPa. The combination of the three manufacturing irregularities also produced close results to the experimental values when applied to the other sets (S450P600 and S450P800), confirming the applicability of the developed model for the range of strut and pore sizes tested.

These results are in accordance with previous works considering manufacturing irregularities: (Campoli, et al. 2013, Hazlehurst, et al. 2013) who found a reduction of E_{ap} from 16.03 to 5.37 GPa; and (Karamooz Ravari and Kadkhodaei 2015), who found an E_{ap} that was around 91% of the experimental one. However, in this last case the chosen unit-cell (BCC) already showed a small difference between numerical and experimental results (around 15%) without considering manufacturing irregularities (Smith, et al. 2013).

The strut inclination (*Sinc*) was the most influent manufacturing irregularity on the computed $\sigma_{ap}-\varepsilon$ curve and on E_{ap} . This is in accordance with Luxner *et al.* (2009), Alkhader and Vural (2008), and with (Ashby 2006) who observed a 10 times difference in E_{ap} between stretch

and bending dominated porous materials. Perfectly aligned struts carry the load axially, however for inclined struts the load is no longer aligned with their axis, which induces bending of the struts (Luxner, et al. 2007) and consequently reduces the overall stiffness and strength (Alkhader and Vural 2008).

The fractured struts (S_{fr}) was the most determinant manufacturing irregularity influencing $S_{Y,ap}$. This is in accordance with Chen *et al.* (1999). When fractured struts are present, their load is distributed between the surrounding struts which become more solicited thus yielding earlier.

Additional investigation is needed to understand why the numerically computed $S_{Y,ap}$ for set S450P800 is smaller than the experimental one. It is not clear whether it is due to the larger pore size (i.e. more slender struts) for which bending effects are more important; or to the difference in the measured strut diameter compared to the two other sets. As shown in Table 4.1, sets S450P600 and S450P700 have similar strut diameters: 648 and 666 μm , respectively; however set S450P800 shows considerably smaller strut diameter, almost 100 μm smaller (577 μm). Also, additional studies are required to assess the performance of the proposed model under different loading conditions, such as bending and torsion.

In the present work we showed that not taking into account the manufacturing irregularities in the FE models lead to an overestimation of the mechanical properties of well-ordered porous materials. This may negatively impact the design of implants made with porous materials (Parthasarathy, et al. 2011, Xiao, et al. 2013). The proposed methodology is a simple way to measure and simulate manufacturing irregularities from a physical sample and this is precisely its strength. The results of the present study show that good agreement between numerical and experimental results can be obtained with little characterization and modeling effort. However, this study showed some limitations. First only one sample was used for the characterization of manufacturing irregularities, which were assumed to be similar for the other samples and were measured on exterior faces. Second, little data corresponding to the strut diameter variation was available and the standard deviation of the

diameter was assumed to be 75 μm based on geometrical considerations. Third, although statistical tests showed no influence, hand measures may be subjective since measured twice by the same person.

4.6 Conclusions

In this study, a simple methodology to characterize and include the most noticeable manufacturing irregularities in the FE models of well-ordered porous materials was presented.

- Manufacturing irregularities may explain the lack of agreement between experimental data and numerical simulations.
- The inclination of struts plays a critical role in the outcomes of the apparent elastic modulus.
- The fractured struts play a critical role in the outcomes of the apparent yield strength.
- We recommend including strut diameter variation, inclined struts and fractured struts in the FE models in order to better predict the mechanical behavior of well-ordered porous materials for implant applications.

4.7 Acknowledgements

Authors would like to acknowledge the Biomechanic's Institute of Valencia (Spain) for the precious experimental data that made possible this study. This study was supported by the Individual Discovery Grant Program from the Natural Sciences and Engineering Research Council of Canada (NSERC).

CHAPTER 5

ARTICLE 3. NUMERICAL DESIGN OF HIP STEMS WITH OPTIMIZED SHAPE AND FUNCTIONALLY GRADED MATERIAL PROPERTIES BY MEANS OF ADDITIVE MANUFACTURED POROUS MATERIALS

Fernando J. Quevedo González¹ and Natalia Nuño¹

¹Département de Génie de la Production Automatisée, Laboratoire de recherche en imagerie et orthopédie, École de technologie supérieure, 1100 Notre-Dame Ouest, Montréal, Québec, Canada H3C 1K3

Article submitted to the journal “Journal of Biomechanics”, Pergamon Press April 2016

5.1 Abstract

The long-term survivorship of hip stems may be affected by their mechanical characteristics. Flexible implants reduce bone resorption but result in worse interfacial conditions and short stems produce similar effects. Two approaches have been followed in the past to improve stem performance: optimize 1) the shape of the stem or 2) their functional gradation of material properties. Additive manufacturing allows producing optimized hip stems with little restrictions in terms of their shape, and material properties distribution, obtained by porous materials with controlled structure at the mesoscale. In the present study, a two-step approach for the simultaneous optimization of the shape and material properties distribution of additively manufactured hip stems is proposed. First, the stem is optimized at the macroscale to minimize the bone loss and the interfacial failure. Second, the porous material is tailored at the mesoscale to accommodate the material properties functional gradation of the stem. A finite element model that takes into account the manufacturing irregularities inherent to porous materials was used. Optimized stems showed 25%-39% bone loss reduction and 64%-97% less interfacial failure risk, compared to a commercial straight tapered stem (Profemur) stem. Optimized stems were 22%-39% smaller in size, 49%-95% less rigid and 27%-46% shorter than the commercial stem. The elastic modulus from the first step was adequately obtained with the porous material, with most differences between the elastic modulus

optimized in the first step and the apparent elastic modulus of the porous material within $\pm 0.9\%$.

Keywords: functionally graded implants, implant optimization, porous material, additive manufacturing.

5.2 Introduction

Stress shielding, which consists in a reduction of stresses in the bone due to the presence of stiff implants, leads to bone resorption that may affect the long-term survivorship of the prostheses and compromise the bone quality for a future revision of the implants (Kuiper and Huiskes 1992, Mai, et al. 2010). On the other hand, large stresses at the bone-implant interface arise with flexible implants, and have been related to increased risk of interfacial failure, pain and larger interfacial micro-movements (Kuiper and Huiskes 1997).

Some authors have attempted to reduce these antagonistic problems (stress shielding and inappropriate interfacial conditions) by optimizing the hip implant shape with 2D (Huiskes and Boeklagen 1988, Fernandes, et al. 2004) and 3D models (Katoozian and Davy 2000, Ruben, et al. 2007, 2012). Recently, Chanda et al. (2015) proposed a shape optimization schema based on genetic algorithms to minimize bone resorption due to stress-shielding and interfacial failure probability. The authors found that compared to the original hip stem design, optimized stems reduced the bone resorption by around 62%-70%, while the area at risk of interfacial failure was reduced from 54% to 38%.

Other researchers have proposed to solve the aforementioned problems with implants having functional gradation of the material properties (Kuiper and Huiskes 1992, 1997), known as functionally graded (FG) hip stems. Simões et al. (1998) investigated different optimization functions for the gradation of a composite cementless stem, while Hedia et al. (2006) optimized the proportions of hydroxyapatite, collagen and bioglass. More recently, Arabnejad Khanoki and Pasini (2013) considered a genetic algorithm based optimization for

a 2D FG hip stem to reduce bone resorption and interfacial failure. The gradation of material properties (e.g. the elastic modulus, E) was obtained by means of well-ordered porous materials, reducing the stress shielding by 76% and the interfacial failure probability by 50%, compared to a solid titanium stem.

Nowadays, additive manufacturing allows for producing hip implants with optimized shapes, imposing few restrictions. Furthermore, it allows the fabrication of well-ordered porous materials (also known as lattice or cellular materials) with high control over their geometry at the mesoscale. The mechanical behavior of these materials is related to their geometrical parameters at the mesoscale (i.e. geometry, strut and pore diameters), which allows for generating the variations of material properties required by FG implants (Luxner, et al. 2005, Harrysson, et al. 2008, Parthasarathy, et al. 2011, Murr, et al. 2012). Finite element (FE) models of lattice materials can be used to determine (tailor) the geometrical parameters of porous materials at the mesoscale in order to obtain the desired mechanical response. However, the computed mechanical behavior can be far from experimental data. Parthasarathy et al. (2010, 2011) found 10 times difference between FE-computed and experimentally-obtained E for lattice materials having simple-cubic unit-cell. Herrera et al. (2014) found this difference to be around 27.5% for diamond unit-cells. In this way, it has been shown that manufacturing irregularities need to be included in the FE models to overcome this limitation (Campoli, et al. 2013, Hazlehurst, et al. 2013, Karamooz Ravari and Kadkhodaei 2015, Quevedo González and Nuño 2016).

To the authors' knowledge, the simultaneous optimization of shape and material properties for hip stems has not yet been done. In addition, the models used to design FG implants with porous materials do not include the inherent manufacturing irregularities.

Therefore, this paper aims at designing additively manufactured hip stems with optimized shape and FG material properties in order to minimize bone resorption and optimize the interfacial stress distribution. First, the shape and E distribution of the hip stems are optimized at the macroscale. Second, the additively manufactured porous material is tailored

at the mesoscale to obtain the optimized non-homogeneous E distribution from the first step. For this purpose, a previously developed FE model for lattice materials that includes manufacturing irregularities (Quevedo González and Nuño 2016) is employed.

5.3 Materials and Methods

5.3.1 Optimization strategy

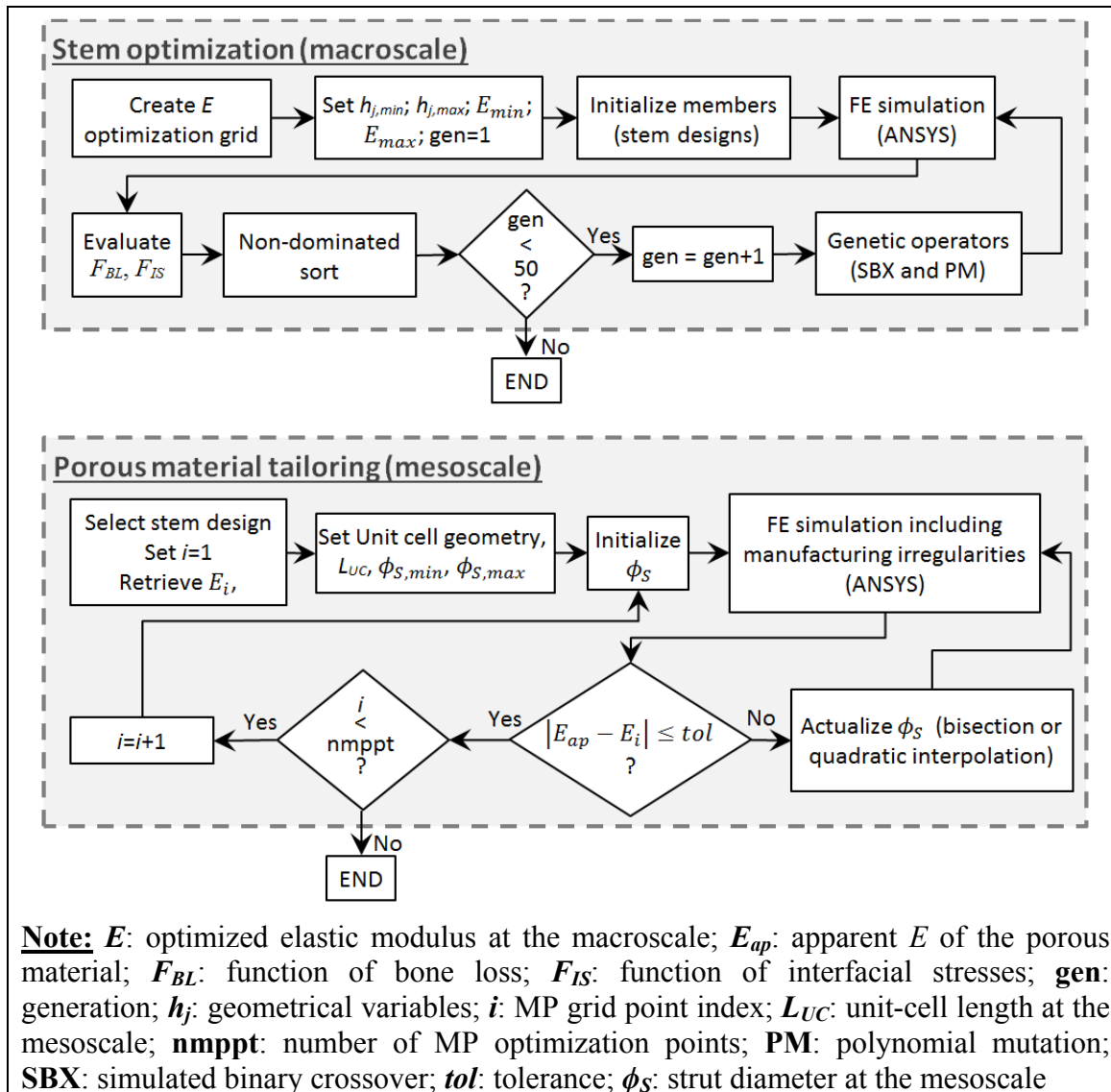


Figure 5.1 General schema for the functionally graded stem optimization.

The two-step approach proposed for the design of functionally graded hip stem is shown in Figure 5.1. First, the shape and material properties distribution (i.e. the elastic modulus, E) of the stems is optimized at the macroscale to minimize a function of the bone loss (F_{BL}) and a function of the interfacial stresses (F_{IS}). In an independent second step, the porous material is tailored at the mesoscale to match the E distribution computed in the first step.

5.3.1.1 Stem optimization at the macroscale

The multi-objective problem of stem optimization at the macroscale is described by Eqs. (5.1)-(5.7). A simplified model was considered for the stem, where the details of the porous material are omitted. The problem comprises 61 optimization variables: 8 shape variables (h_j) and the elastic modulus (E_i) at each of the 53 MP optimization points of the stem (Figure 5.2). The optimization problem was solved using the genetic algorithm NSGA-II (Deb, et al. 2002), with a population of 590 real-coded members and 50 generations (30090 function evaluations). The genetic operators simulated binary crossover with a probability of 0.9 and distribution index of 10, and polynomial mutation with a probability of 0.05 and distribution index of 5 were considered (Deb and Agrawal, 1999).

$$\mathbf{minimize:} \quad F_{BL}; F_{IS} \quad (5.1)$$

Subject to:

$$E_i \in [E_{min}, E_{max}] \quad (5.2)$$

$$h_j \in [h_{min}, h_{max}] \quad (5.3)$$

$$h_2 \cdot \cos \alpha_2 - h_1 \cdot \cos \alpha_1 \leq 0 \quad (5.4)$$

$$h_4 - (\min[h_3, h_5]) \cdot \cos \alpha_3 \leq 0 \quad (5.5)$$

$$h_5 \cdot \cos \alpha_3 - h_6 \cdot \cos \alpha_2 \leq 0 \quad (5.6)$$

$$\left| \frac{h_1 \cdot \cos \alpha_1 - h_2 \cdot \cos \alpha_2}{h_2 \cdot \sin \alpha_2 - h_1 \cdot \sin \alpha_1} - \frac{h_1 \cdot \cos \alpha_1 - h_3 \cdot \cos \alpha_3}{h_3 \cdot \sin \alpha_3 - h_1 \cdot \sin \alpha_1} \right| + 0.01 \leq 0 \quad (5.7)$$

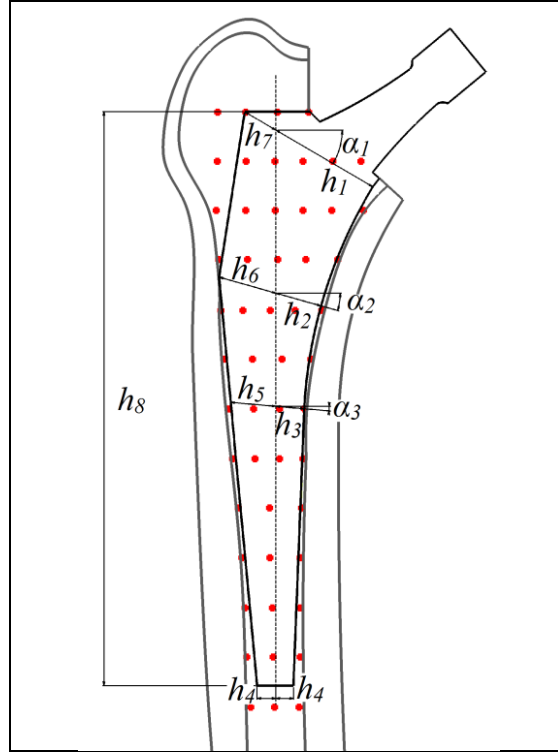


Figure 5.2 Geometrical variables (h_i) for the stem shape and grid (red dots) for the optimization of material properties. The angles $\alpha_1=29.79^\circ$, $\alpha_2=15.8^\circ$, $\alpha_3=4.88^\circ$ have fixed values

The function of bone loss F_{BL} (Eq. (5.8)), accounted for the bone loss due to stress-shielding (Kuiper and Huiskes 1992), and the bone loss due to the stem size ($m_{loss,stem}$). This two-term formulation emphasizes short stems over large stems that would greatly diminish the bone stock.

$$F_{BL} = \frac{1}{M} \left(m_{loss,stem} + \int_{V_{bone}} g(S_{en}) \cdot \rho(x,y) \cdot dV_{bone} \right) \quad (5.8)$$

where M is the total bone mass, $\rho(x,y)$ is the bone density and $g(S_{en})$ is the resorption function: $g(S_{en})=1$, if $S_{en} < (1 - sd) \cdot S_{en,ref}$, being S_{en} and $S_{en,ref}$ the strain energies per unit of bone mass after and before implantation, respectively. The dead zone (sd) reflects the changes in S_{en} that do not carry variations in the bone density.

The function of interfacial stresses F_{IS} (Eq. (5.9)), was based on the interfacial failure index $f_{IS}(\tau) = (\tau/S_S)^2$ (Kuiper and Huiskes 1992, Arabnejad Khanoki and Pasini 2013), being $S_S = 21.6\rho^{1.65}$ the interfacial strength (Stone, et al. 1983) and τ the interfacial shear stress. The proposed function accounted for the homogeneity of τ distribution, penalizing stems with large τ and/or larger zone without contact (i.e. longer tip).

$$F_{IS} = \frac{(\max\{f_{IS}(\tau)\})^2}{\frac{1}{A_{stem}} \int_{A_{stem}} f_{IS}(\tau) \cdot dA_{stem}} \quad (5.9)$$

where A_{stem} is the stem interfacial area.

Table 5.1 shows the original, minimum and maximum values for the shape variables. The original stem shape corresponded to a straight tapered Profemur-TL stem (Wright Medical Technology, Arlington, TX, USA). The variables h_2 and h_6 were fixed to guarantee contact between the stem and the cortical bone. For the rest of the variables, maximum values were chosen to avoid intersecting the cortical bone, whereas minimum values were selected as small as possible to keep proper stem shape. The geometrical constraints (Eqs. (5.4)-(5.7)) assured appropriate shape for the stem.

Table 5.1 Initial, minimum and maximum values for the 8 shape variables

Shape variable	h (mm)		
	Original	Minimum	Maximum
h_1	28.0	28.2	28.4
h_2	11.8	11.8	11.8
h_3	7.1	6.5	7.4
h_4	4.5	1.1	6
h_5	11.3	2.8	11.5
h_6	14.5	14.5	14.5
h_7	8.9	0.5	16.5
h_8	141.9	73.2	146.3

The stem E lower bound $E_{min}=2\text{GPa}$ was chosen to ensure the structural integrity of the lattice material, based on previous experiences (Barraud 2015); while the upper bound $E_{max}=110\text{ GPa}$ corresponded to solid Ti6Al4V. The stem neck and a layer of 1.5 mm thickness around the stem (to provide a continuous surface for the contact) were kept as solid material.

5.3.1.2 Porous material tailoring at the mesoscale

A separate step was performed to tailor the porous material at the mesoscale in order to obtain the optimized E distribution obtained from the stem optimization step at the macroscale. A previously developed FE model of the porous material that includes the manufacturing irregularities (Quevedo González and Nuño 2016) was employed.

The shape of the unit cell was set to simple-cubic, while its size (L_{UC}) was fixed to 1.5 mm. Therefore, the problem consisted in a set of linearly independent problems (as many as MP optimization points), where the strut diameter (ϕ_S) of the porous material is the only variable. These were formulated as the root finding problems shown in Eqs. (5.10)-(5.11), and was solved with the Brent's algorithm for root finding, which combines bisection and quadratic interpolation (Press, et al. 1992).

$$\text{Find } \phi_S, \text{ so that: } \quad |E_{ap} - E_i| = 0 \quad (5.10)$$

$$\text{With: } \quad \phi_S \in [\phi_{S,min}, \phi_{S,max}] \quad (5.11)$$

The lower bound $\phi_{S,min}=L_{UC}/3=0.5\text{ mm}$ was chosen to guarantee structural integrity, based on previous experiences (Vanderesse, et al. 2016); whereas the upper bound $\phi_{S,max} = L_{UC}\sqrt{2} = 2.12\text{ mm}$ is the maximum theoretical value that can be fitted in the unit-cell.

5.3.2 Finite element modeling

5.3.2.1 Stem and bone at the macroscale

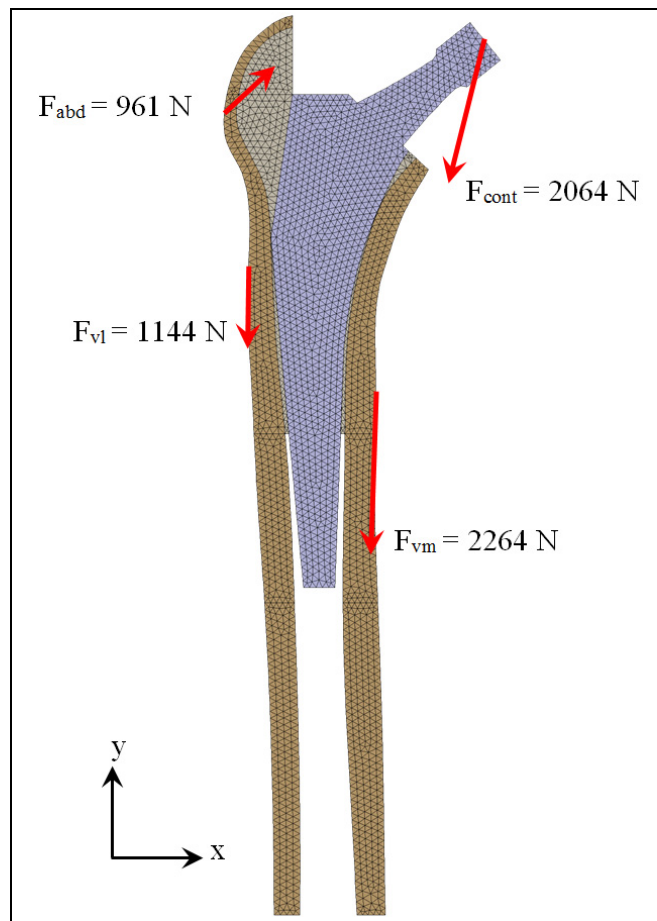


Figure 5.3 Meshing and loading of the stem and bone model

A 2D FE model of an implanted proximal femur (Figure 5.3) with a side-plate that accounts for the 3D effects was considered. Meshing and simulation were done in ANSYS Mechanical v14.5. The mesh consisted in 6-node plane-stress triangle elements with an element size of 1.5 mm. A 12 mm constant thickness was considered for the cortical bone elements. The cancellous bone, stem and side-plate elements had variable thickness, derived from the original 3D model to match the inertia with respect to the out-of-plane axis. In total, approximately 17382 finite elements were generated: 7900 for the stem and bone and 9482

for the side-plate. Loading was derived from Heller et al. (2005), and comprised the hip contact force (2064 N), the abductor (961 N), vastus medialis (2264 N) and vastus lateralis (1144 N) muscles for a bodyweight of 847 N (Figure 5.3). All distal nodes of the cortical were fixed and bonded contact was assumed between stem and bone, corresponding to a situation where fixation by bone ingrowth has been achieved.

Materials were considered as linear elastic and isotropic. The elastic modulus of the bone was set to $E_{canc}=345$ MPa for the cancellous and $E_{cort}=12$ GPa for the cortical bones (Reimeringer, et al. 2013). For the stem, E was allowed to vary between $E_{min}=2$ GPa, and $E_{max}=110$ GPa, as described in the previous section.

5.3.2.2 Porous material at the mesoscale

A finite size beam FE model with 8x8x8 unit-cells is considered for the porous material (Figure 5.4- a). This is the cost-effective sample size that provides similar results to the infinite media approach (Quevedo González and Nuño 2015). Meshing consisted in 3888 Timoshenko beam elements. Strut inclination and diameter variation manufacturing irregularities were included in the FE model (Figure 5.4 - b). Based on previous studies (Quevedo González and Nuño 2016, Vanderesse, et al. 2016), both manufacturing irregularities were assumed to follow normal distributions, with the characteristic values shown in Table 5.2.

Table 5.2 Values for the distributions of manufacturing irregularities

	average	standard deviation	min/max
Strut diameter (mm)	ϕ_s	0.1	$\phi_s \pm 0.25$
Strut inclination (°)	0	7.3	± 45

This detailed model was combined with a more precise elastic-plastic bilinear model for Ti6Al4V material, derived from in-house experimental testing on additively manufactured samples, and defined by the elastic modulus $E=111.2$ GPa, the tangent modulus $K=5.7$ GPa,

the yield strength $S_Y=1145$ MPa and the Poisson's ratio $\nu=0.3$. A non-linear uniaxial compression simulation, considering large deformations, allowed computing the apparent elastic modulus (E_{ap}) of the lattice material as the slope of the apparent linear zone of the apparent stress-strain ($\sigma_{ap}-\varepsilon$) curve.

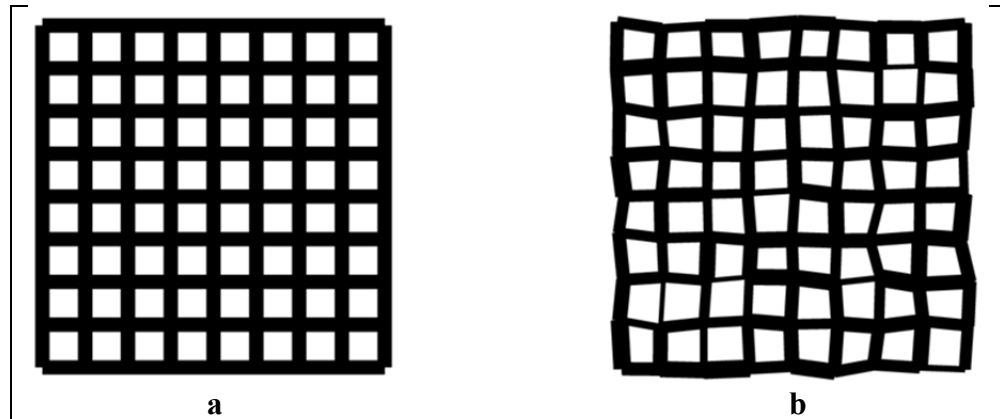


Figure 5.4 Porous material model at the mesoscale: a - idealized; b - with manufacturing irregularities. Beam elements have been thickened to show the ϕ_S variation

5.4 Results

First, optimization results are presented in terms of the objective functions of bone loss (F_{BL}) and interfacial stresses (F_{IS}) and compared to the performance of the original (Profemur) stem design. Then, the shape at the macroscale and porous material tailoring at the mesoscale for 4 selected optimized stems is shown. The performance of these stems is compared with the original design in terms of the resorbed bone (m_r) and interfacial stresses (τ). Finally, the accuracy of the porous material tailoring is presented by comparing the obtained apparent elastic modulus (E_{ap}) with the prescribed elastic modulus (E).

The four plots in Figure 5.5 show the performance in terms of F_{BL} and F_{IS} of the 590 members (stem designs) after 50 optimization generations (30090 function evaluations), with diamond markers indicating the members of the first non-dominated front (100 members). The color coding in each plot shows respectively the influence of bone resorption, stem size

(i.e. the total area of the stem), average stem stiffness (E_{avg}) and stem length (i.e. variable h_8 in Figure 5.2). The four representative stem designs chosen for the second step are circled and marked b-e.

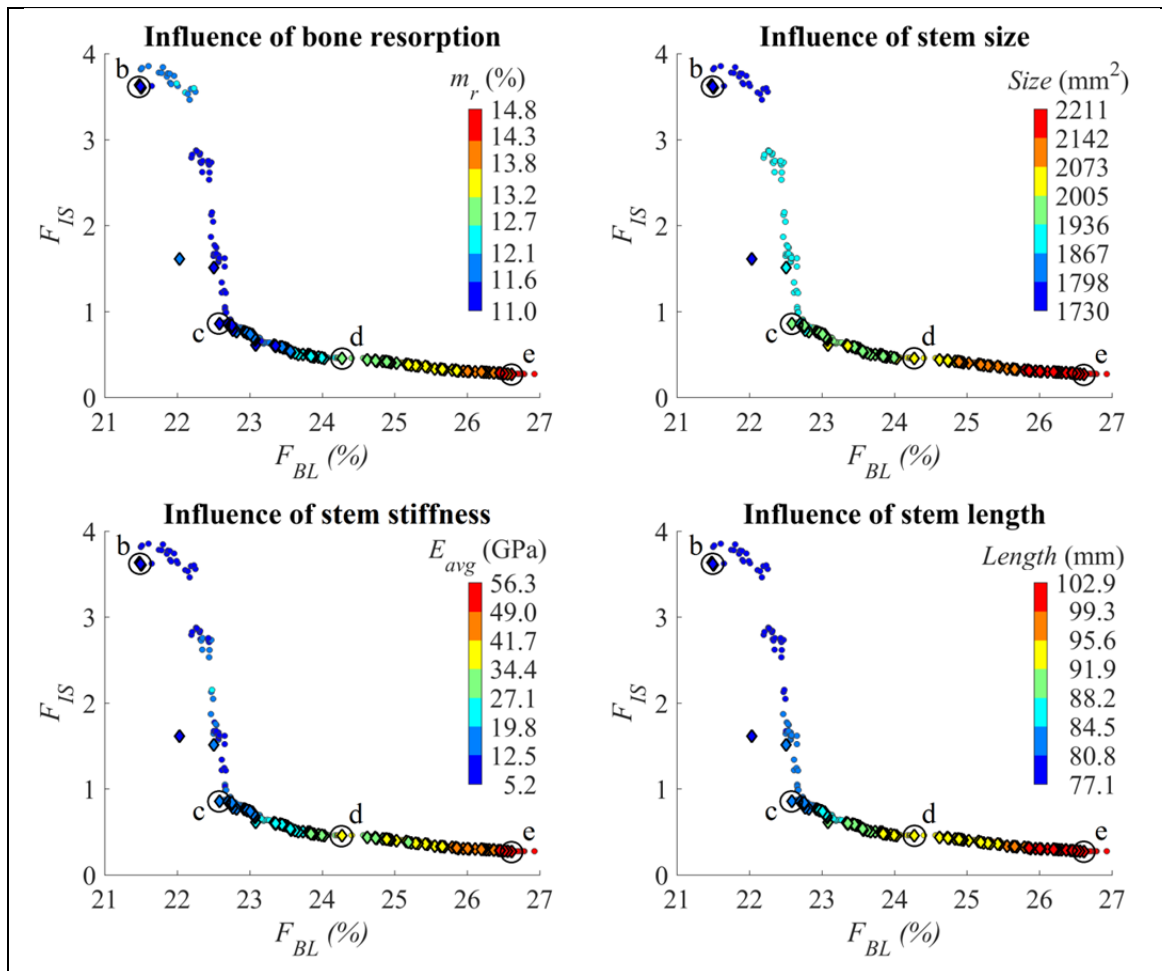


Figure 5.5 590 optimized stems after 50 generations (30090 function evaluations). Diamond markers: first non-dominated front. The different plots show the influence of bone resorption, stem size, stiffness and length in the interfacial failure index (F_{IS}) and bone loss index (F_{BL}). Representative selected stem designs b-e are circled

Solutions align into a Pareto front where lower F_{BL} comes at the cost of worse F_{IS} . All optimized designs show $F_{BL}=21.5\text{-}26.6\%$ and $F_{IS}=0.27\text{-}3.64$; whereas the original stem design shows $F_{BL}=35.4\%$ and $F_{IS}=10.20$. Additionally, optimized stems show lower bone resorption ($m_r=11.0\%\text{-}14.8\%$), smaller sizes ($1730\text{-}2211 \text{ mm}^2$), less stiffness ($E_{avg}=5.2\text{-}56.3$ GPa) and smaller length ($77.1\text{-}102.9$ mm), than the original stem design ($m_r=23.9\%$,

$size=2851 \text{ mm}^2$, $E_{avg}=110 \text{ GPa}$, $length=141.9 \text{ mm}$). In general, larger F_{BL} and lower F_{IS} correspond to larger m_r , size, stiffness and length of the stems. Nevertheless, in some cases, equivalent solutions in terms of F_{BL} and F_{IS} are obtained with different combinations of the aforementioned factors.

Figure 5.6 shows the distributions of m_r and τ for the original stem and the selected representative designs (b - e in Figure 5.5). The porous structure is shown, with the color coding representing the strut thickness and the corresponding E_{ap} computed in the second step of porous material tailoring at the mesoscale. For clarity, one scale is used for members b-c, and a different one for members d-e. The original stem design presents extensive bone resorption ($m_r=23.9\%$) affecting almost completely the medial and lateral proximal cortices, and τ increases from proximal to distal with peaks around 4.5 MPa in the mid-lateral and distal-medial zones. In contrast, bone resorption for optimized stems is concentrated mainly in the proximal cortex. Stems with lower F_{IS} (d, e) show more bone resorption in the medial cortex, while m_r trends to shift towards the lateral cortex for stems with lower F_{BL} . The τ distribution of the optimized stems is more homogeneous, with increased proximal values and decreased distal peak. The τ values range from 0 to approximately 3.4 MPa; and in the best case (design e with the lowest F_{IS}) the maximum τ is smaller than 1.9 MPa.

All optimized stems are shorter than the original stem and present thin distal tip. Longer stems and more pronounced proximal-lateral shoulder decrease F_{IS} however increase F_{BL} (from designs b to e). Similarly, stiffer stems decrease F_{IS} and increase F_{BL} (from designs b to e).

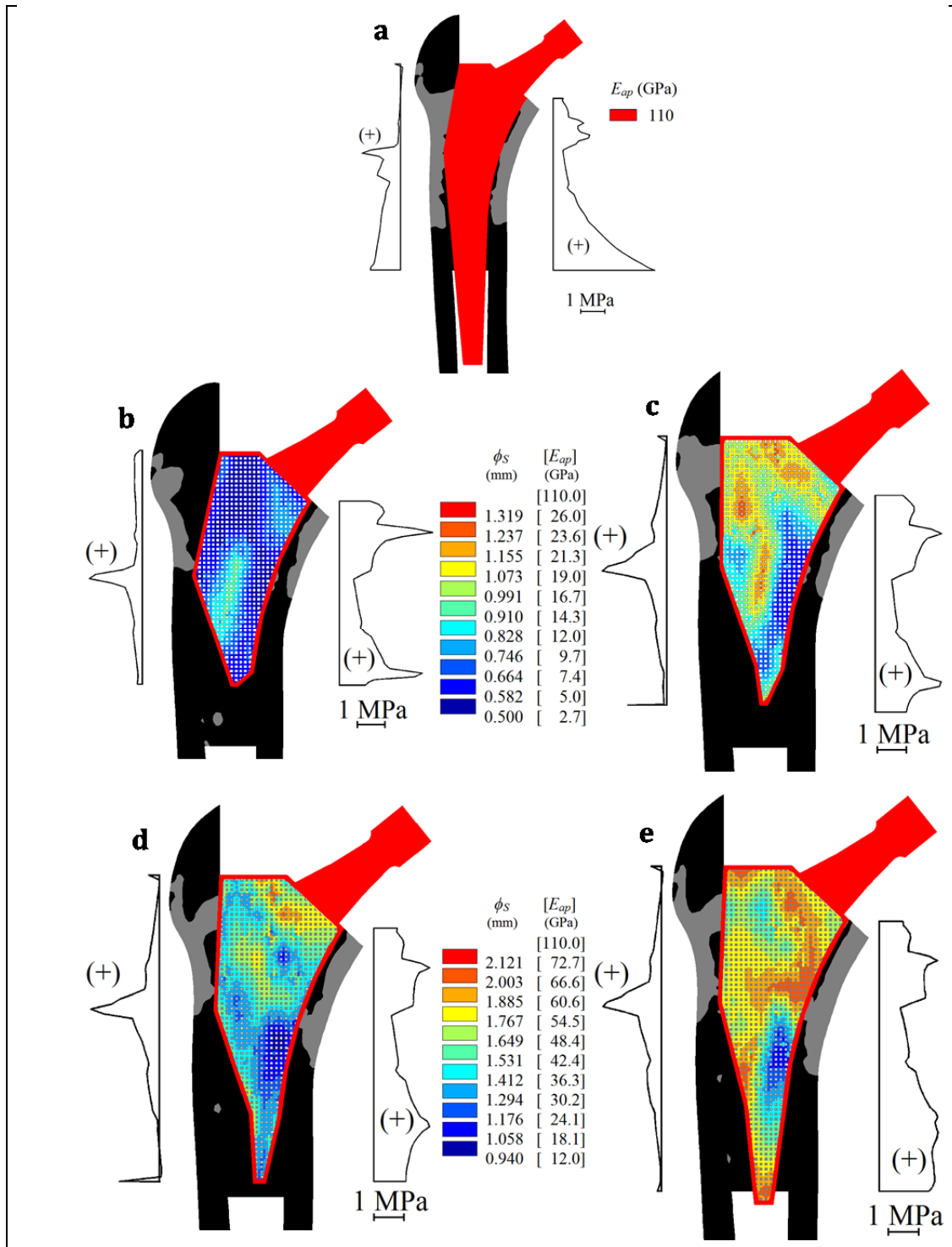


Figure 5.6 Distribution of resorbed bone (grey) and non-resorbed bone (black) and interfacial shear stresses (in MPa) for a) the original stem design; b)-e) the selected (optimized) stem designs of Figure 5.5. The color maps represent the strut thickness (ϕ_s in mm) and the corresponding apparent elastic modulus (E_{ap} , in GPa) as computed in the porous material tailoring at the mesoscale step

As shown in Figure 5.6, the ranges for the strut diameter (ϕ_S) of the porous material of the stems (as computed in the second step of porous material tailoring) are $\phi_S=0.5$ -0.969 mm for stem b, $\phi_S=0.581$ -1.319 mm for stem c, and $\phi_S=0.94$ -2.12 mm for stems d and e. For all stems, ϕ_S is smaller at the mid-medial level, and this small ϕ_S zone extends laterally for less rigid stems (b, c). Such ϕ_S distribution yields a coherent E_{ap} distribution that results in small differences (in %) with the optimized E at the macroscale during the first step (as shown in Figure 5.7). Most differences between E_{ap} and E are within the range $\pm 0.9\%$. This observation is supported by small values of the root mean square differences (RMSD): 0.19 MPa for stems b and c, 3.89 MPa for stem d, and 5.22 for stem e. Nevertheless, large differences up to around 32% arise in localized zones for all stems except for stem c. Indeed, for the established limits of ϕ_S , the porous material model as it was defined did not succeed in computing E_{ap} outside the range 2.7-72.7 GPa. Therefore large differences occur where the optimized E at the macroscale was not within $E=2.7$ -72.7 GPa (all E values of stem c are within these limits).

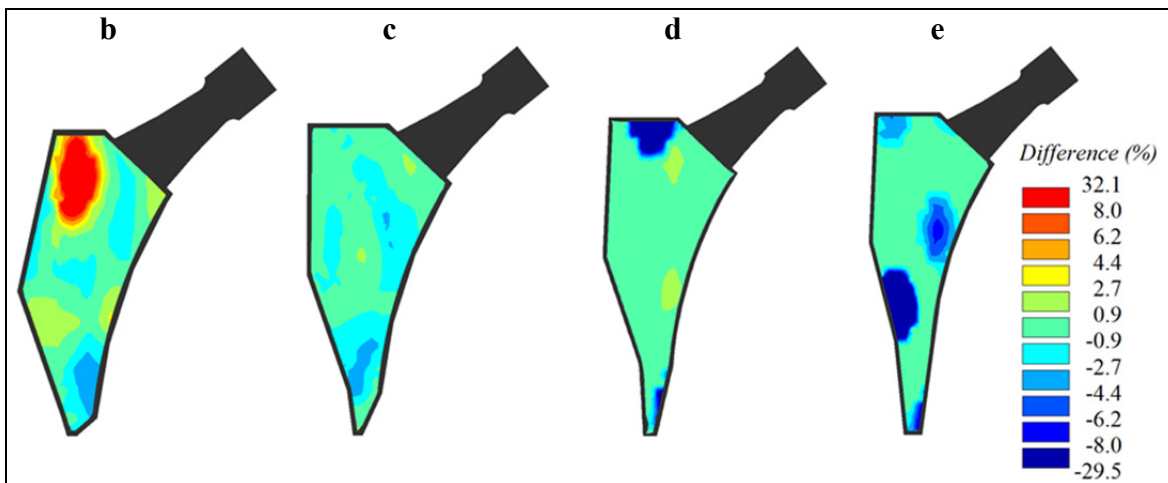


Figure 5.7 Differences (in %) between E_{ap} and the prescribed E for the selected stem designs b – e of Figure 5.5.

5.5 Discussion

In this work, a two-step approach for the optimization of additively manufactured hip stems has been proposed. The first step dealt with the optimization of shape and E distribution of

the stem at the macroscale in order to decrease the bone loss and generate adequate interfacial stresses. In a second step, the porous material was tailored at the mesoscale to match the optimized E for 4 selected stem designs using a previously developed FE model that includes the manufacturing irregularities inherent to porous materials.

In terms of the stem optimization at the macroscale, this study presented the novelty of simultaneously optimizing the stem shape and E distribution. The proposed objective functions of bone loss (F_{BL}) and interfacial stresses (F_{IS}) had contradictory effects: lower F_{BL} came at the cost of more critical F_{IS} . When compared to the original (Profemur) stem, optimized stems yielded a total 25-39% F_{BL} reduction due to the combination of 38-54% decrease of bone resorption (m_r) and the need for less bone resection for stem insertion (due to smaller sizes). In addition, optimized stems increased the proximal interfacial stresses (τ) from approximately 1.5 MPa to 1.9-3.4 MPa and reduced the distal peak from approximately 4.2 MPa to 3-1.9 MPa, resulting in a more homogeneous τ distribution that reduced F_{IS} by 64%-97% compared to the original stem. This was achieved with stem designs having thin distal tip and being 22-39% smaller, 49-95% less rigid and 27-46% shorter than the original (Profemur) stem. In general, stiffer, longer and larger stems decreased F_{IS} and increased F_{BL} .

The results of the present study are in agreement with the literature. The computed m_r distribution and the corresponding $m_r=23.9\%$ was similar to $m_r=23\%$ computed by Huiskes et al. (1992) for titanium stems. For the optimized stems, m_r range was 11-14.8%, being slightly lower than $m_r=14-22\%$ reported by Arabnejad Khanoki and Pasini (2012) for stem material optimization; and $m_r=24-27\%$ reported by Chanda et al. (2015) for stem shape optimization. In addition, the τ distributions follow the same trend found by Kuiper and Huiskes (1992) and Arabnejad Khanoki and Pasini (2012): the original stem shows a smaller proximal-medial peak and larger distal-medial peak, whereas optimized stems result in more homogeneous τ distribution with increased proximal τ . Furthermore, the maximum τ computed in the present work (4.5 MPa for the original stem and 1.6-3.5 MPa for the optimized designs) are similar to the maximum values 2.15 MPa and 2.8 MPa reported by

Arabnejad Khanoki and Pasini (2012) for stem material optimization, and Kowalczyk et al. (2001) for stem shape optimization.

Concerning the second step of tailoring the porous material at the mesoscale, the main contribution of the present work is to take into account the effects of the inherent manufacturing irregularities. This has been shown to result in closer predictions for the apparent elastic modulus (E_{ap}) of the porous material (Campoli, et al. 2013, Quevedo González and Nuño 2016). Furthermore, since similar E_{ap} (0.5-12 GPa) have been obtained with simple cubic (Parthasarathy, et al. 2010), diamond (Herrera, et al. 2014) and dodecahedron (Amin Yavari, et al. 2013) unit cells, the two-step approach presented in this paper, allows for changes of the unit cell geometry and/or size without affecting the results from the step of stem optimization at the macroscale.

The employed method for determining the strut diameter (ϕ_s) to match a given E (Brent's algorithm) showed relatively fast convergence, requiring fewer than 15 iterations and achieving, in general, small differences between E and E_{ap} (root mean square differences between 0.19 MPa and 5.22 MPa). Large localized differences arised due to the mismatch between the limit values allowed for $E=2-110$ GPa and the limit $E_{ap}=2.7-72.7$ GPa that the porous material model was able to compute with the imposed constraints for ϕ_s (0.5-2.1 mm). Two factors may contribute to this limitation: 1) the variation of manufacturing irregularities with the strut diameter was not taken into account and 2) the strut-to-strut contact was not considered. In this way, thicker struts may show different values for the manufacturing irregularities than slenderer struts and are more likely to come into contact, resulting in a stiffer response of the lattice material. In the future, these features should be included in the model.

In future studies, it would be interesting to : 1) investigate the optimization for an immediate post-operative situation, where frictional contact between stem and bone exists, with the objective of improving the primary stability (i.e. minimize interfacial displacements); 2) use patient specific data (i.e. bone geometry and density), which can be included in the present

approach in a straight-forward manner; 3) generalize to a 3D model, where shape and material properties optimization is also performed along the third spatial direction; 4) consider the unit cell geometry and size as optimization variables; 5) evaluate the long-term behavior of the stem in terms of fatigue life and bone remodeling.

5.6 Conclusion

This study has shown that optimizing simultaneously the shape and the material properties of hip stems may greatly improve their outcomes in terms of interfacial stresses and bone preservation. The proposed two-step allows changes in the porous material unit cell geometry and size at the mesoscale, without affecting the optimized shape or material properties distribution at the macroscale. In addition, to tailor the porous material, the manufacturing irregularities, which are determinant in the FE-experimental results correspondence, were taken into account.

5.7 Acknowledgements

This study was supported by the Individual Discovery Grant Program from the Natural Sciences and Engineering Research Council of Canada (NSERC).

CHAPTER 6

GENERAL DISCUSSION

The main objective of the present thesis was to design hip implants with optimized shape and functionally graded material properties in order to improve their mechanical compatibility with the bone. This was done by addressing two antagonistic problems: reduce stress shielding and generate adequate interfacial stresses. The proposed approach was developed having additive manufacturing capabilities in mind, in such a way that a functional gradation of the material properties (i.e. elastic modulus) of the stem was obtained using porous materials having well-controlled structure at the mesoscale.

This was achieved by means of three specific objectives, namely:

- 1) *To investigate different finite element modeling approaches to simulate porous materials.*
- 2) *To evaluate the effects of manufacturing irregularities of porous materials in the accuracy of computational models compared to experimental data.*
- 3) *To develop an optimization approach for hip stems having functionally graded material properties through porous materials.*

Each specific objective was addressed, respectively, by one journal article presented in this thesis. A *synthesis of the articles* is presented in the following section, with special emphasis in the bonding link between the articles. Then, the *limitations* and *recommendations* as well as *future work* are discussed.

6.1 Synthesis of the articles

The first two objectives and their corresponding articles dealt with the FE modeling of porous materials produced by additive manufacturing to predict their mechanical behavior. In this way, two questions were addressed: 1) which is the most suitable FE modeling approach? And 2) how can the numerical results be closer to experimental data?

The first article showed that both solid (continuum) and beam finite element models of porous materials yield similar results, and differences between both approaches are dependent on the slenderness ratio of the struts. The influence of the sample size (i.e. number of pores) in the model was revealed. As the sample size increased, the boundary conditions had less influence and both models tended to converge to the results provided by the infinite media approach (which is not affected by the boundary conditions). The differences between the finite size models and the infinite media approach were under 8.4% for samples larger than 8 pores. This was defined as the cost-effective sample size for future analyses. In a second part of the article, it was shown that diamond unit cell shows more homogeneous stress distribution within the struts and more similar bending and compressive behavior, which might be desirable in hip prosthesis applications.

In the second article, the manufacturing irregularities were identified and characterized. This was done considering simple cubic unit cells due to the simplicity of the characterization and the availability of experimental data. It was shown that manufacturing irregularities of porous materials play a crucial role on their mechanical response. The strut inclination and fractured struts were the manufacturing irregularities that most influenced the apparent elastic modulus (E_{ap}) and the apparent yield strength ($S_{Y,ap}$), with reductions of 76% and 37%, respectively, compared to the idealized model. When these two manufacturing irregularities and the strut diameter variation were combined together, the closest results to the experimental data were obtained: E_{ap} decreased from 35 GPa to 5.41 GPa (experimental value was 2.82 GPa), and $S_{Y,ap}$ decreased from 263 MPa to 157 MPa (experimental value was 164 MPa).

In the third article, a methodology for the optimization of hip stems was proposed. This considered the stem shape optimization, along with the functional gradation of the material properties of the stem, which was obtained by means of well-ordered porous materials. The porous material model with manufacturing irregularities (developed in the second article) was employed to tailor the porous material in order to achieve the functional gradation of material properties within the hip stem. Furthermore, to reduce computational costs, the beam model with cost effective sample size of 8 pores (as determined in the first article) was employed in the porous material model. Several trade-off stem designs were presented, which reduced the resorbed bone mass between 38% and 54%, while the maximum interfacial stresses were decreased between 22% and 64%. The optimized functional gradation of the elastic modulus was successfully obtained with a tailored porous material, with most differences between the optimized elastic modulus and the apparent elastic modulus obtained with the porous material being within $\pm 0.9\%$.

6.2 Limitations

Some of the limitations of the present thesis are shown in the next paragraphs. These are divided in limitations related to the *porous material model* and limitations related to the *optimization of the hip stem*.

6.2.1 Limitations related to the porous material model

Three kind of limitations fall under this category, relative to: the unit-cell geometry, the beam model, and the manufacturing irregularities.

6.2.1.1 Unit cell geometry

Most of the work presented in this thesis is focused on the simple cubic unit cell geometry. It was shown in the first article that when static load conditions are considered, simple cubic unit cell may not be the best choice for implant applications since the load is not

homogeneously distributed within the struts and the direction of loading affects more the mechanical response. On the other hand, studies have shown that simple cubic unit cell has better fatigue behavior than diamond or other unit cells (Amin Yavari, et al. 2015). Therefore the choice of the unit cell geometry for implant applications is not clear yet.

This lack of diversity in terms of the studied unit cell types is one of the limitations of the present work. The finite element model presented here needs to be adapted to other unit cells and their correspondence with experimental data will need to be addressed. Then, the models can be used to evaluate the different unit cells under a variety of loading conditions in order to determine the best suited for each implant.

6.2.1.2 Beam model

In this thesis it was shown that the beam model yields similar results to the continuum (solid) approach, requiring fewer modeling efforts (especially for including the manufacturing irregularities) with less computational cost. This was crucial for the porous material tailoring performed in the third article, where large number of simulations was required. However, the beam model is limited in terms of the available information of the mechanical behavior at the mesoscale (i.e. stresses and strains in the struts). To overcome this limitation, a submodeling approach may be employed, where the macroscopic behavior of the porous material is computed with the beam model and a continuum model is used to simulate in more detail selected struts.

In addition, the strut-to-strut contact has not been included in the finite element models. It was shown in the third article that this limits the applicability of the model to porous material with high porosity (i.e. low apparent elastic modulus). Indeed, for denser porous materials, the struts are close to or already in contact which causes a stiffening of the mechanical response that is not captured with the present model. This feature needs thus to be considered in order to have a more general model that can be applied to wider ranges of porosity of the porous materials.

6.2.1.3 Manufacturing irregularities

The second article revealed that including the manufacturing irregularities (and in particular the ones considered in this work) in the finite element models, greatly improves the correspondence of the computational results with experimental data. Nevertheless, some assumptions were made (i.e. maximum strut diameter variation) and a detailed characterization was not performed. As a consequence, the predictions of the elastic modulus (5.41 GPa) were almost the double than experimental data (2.82 GPa). Motivated by these results, Vanderesse et al (2016) developed a methodology for more accurately characterizing the manufacturing irregularities of porous materials based on microscopic images and image treatment. The manufacturing irregularities as measured by Vanderesse et al (2016) thus need to be included in the FE models and the improvement in terms of the correspondence with experimental data has to be evaluated.

In addition, the manufacturing irregularities were assumed to have constant values, independent on the geometrical dimensions of the porous materials (i.e. strut, pore and unit cell sizes). This may have also contributed to the limitation shown in the third article for the stiffest zones of the implants. It is thus necessary to study the evolution of the values of the manufacturing irregularities with the geometrical dimensions. Such evolution needs then to be considered in the finite element models in order to improve their correspondence with experimental data for a variety of geometrical dimensions.

6.2.2 Limitations related to the optimization of the hip stem

Four limitations fall under this category: 1) the dimensionality of the bone-implant model, 2) the interfacial conditions, 3) the evaluation of implant performance, and 3) the tailoring of the porous material.

6.2.2.1 Dimensionality of the bone-implant model

To perform the optimization of the hip stems presented in the third article of this thesis, a 2D model was considered. Such model took into account the 3D effects by considering variable thickness for the finite elements and with additional layer of elements connecting both cortexes, the side plate. This approach has shown good correspondence with 3D models for hip stems (Quevedo González et al., 2016). Nevertheless, such correspondence may be compromised for other implants and in different loading scenarios (e.g. higher torsional component). On the other hand, this approach does not consider the optimization of the stem shape and material properties distribution in the out-of-plane direction. Therefore, the optimization approach should be generalized to 3D in order to be applicable to other implants and to consider a more complete optimization of the stem. To counteract the increase in computational cost that arises from having more degrees of freedom in the finite element model and more optimization variables, efficient simulation and optimization strategies should be considered.

6.2.2.2 Interfacial conditions

In this thesis, bonded contact between bone and implant was considered. This corresponds to a long-term scenario where secondary fixation by bone ingrowth has been achieved. Therefore the hip stems have only been optimized for such situation. Nevertheless, to assure good long-term outcomes, the stems also need to have good primary stability, which is represented by reduced micro movements at the bone-implant interface (Reimeringer, et al. 2013). In this way, the minimization of such micro movements under frictional bone-implant interfacial conditions need to be included in the optimization procedure in order to improve the performance of the stems throughout their lifetime.

6.2.2.3 Evaluation of implant performance

The implant performance was assessed by means of the bone resorption and the interfacial failure. On the one hand, the bone resorption was assumed to be proportional to the resorption stimuli and the evolution of bone remodeling was not taken into account, which can alter the amount of resorbed bone mass. In addition, only the interfacial failure due to shear stresses was considered. Therefore, in the future, the bone remodeling should be evaluated, at least for optimized stems in order to quantify more precisely the bone loss. In terms of the interfacial failure, the outcomes of the proposed approach and considering the interfacial failure based on shear and normal stresses would need to be compared.

6.2.2.4 Tailoring of the porous material

Considering the unit cell geometry and length of the porous material as fixed parameters allowed reducing the problem to a set of linearly independent problems. In order to have a more general procedure for the tailoring of porous materials for implant applications, the unit cell geometry and/or length need to be considered as optimization variables. This turns the problem into a multivariable optimization and new rules need to be considered to determine the optimality of the unit cell geometry and size.

In addition, the local stress state and the specific boundary conditions of the stem were not taken into account in the material tailoring, and the material was only tailored under static load conditions not considering fatigue behavior. In a more general procedure, the local stress state should be considered in such a way that the unit cells can be oriented to minimize undesired loading conditions such as shear. Furthermore, the optimal unit cell geometry can be determined according to such stress state. On the other hand, specific boundary conditions derived from the implant may be employed to tailor the porous material, so that the effect of the actual boundary conditions that the material will face is taken into account. Finally, the fatigue behavior of the porous material needs to be assessed to guarantee the structural integrity of the implant in the long-term scenario.

6.3 Future work

The future work that derives from the previous limitations can be summarized as:

- *Porous material model*
 - Generalize the FE model of the porous material to include other unit cell geometries and compare results to experimental data under different load conditions (e.g. bending, torsion and shear).
 - Include the beam-to-beam contact in the FE model.
 - Consider the results from the more precise characterization of manufacturing irregularities done by Vanderesse et al. (2016) in the FE model.
 - Evaluate the variation of manufacturing irregularities with the geometrical parameters of the unit cell and incorporate them in the FE model.
- *Optimization of the hip stem*
 - Generalize the 2D model to a 3D model.
 - Consider initial stability for the optimization of hip stems.
 - Consider the effects of bone remodeling and determine the effect of different approaches to evaluate the interfacial failure on the optimized stems.
 - Consider the unit cell shape and length as variables for the porous material tailoring.

- Consider the local stress state and specific boundary conditions in the tailoring of the porous material.
- Evaluate the implant behavior under fatigue.

Other future work may be considered to take the present work to a next level. This includes investigating how the distribution of manufacturing irregularities within the porous material affects its mechanical behavior, consider patient-specific data (e.g. geometry and bone mechanical properties) to design implants adapted to the specific patient, and extend the proposed methodology to other implants that may have worse outcomes and thus, larger room for improvement. In addition, selected stem designs need to be manufactured and tested considering *in vitro* conditions (e.g. mechanical tests) and *in vivo* conditions (e.g. using animal models).

CONCLUSION

Stress shielding and high bone-implant interfacial stresses may lead to bone resorption and interfacial failure, respectively, affecting the survivorship of hip implants. These phenomena have mechanical origin and they can be mitigated by optimizing the shape and creating a functional gradation of the material properties of the stems. To this end, the geometry at the mesoscale of porous materials can be designed and produced by additive manufacturing to tailor their mechanical properties in order to generate the aforementioned non-homogeneous mechanical properties distribution within the stem. For this purpose computational (finite element, FE) methods are required to simulate the mechanical behavior of such materials, to evaluate the performance of hip stems and to perform the optimization of hip stems, including the tailoring of the porous material.

One of the main decisions that need to be made when simulating porous materials is the choice of the FE approach: beam vs continuum elements and finite vs infinite model size. Each approach has its advantages and drawbacks and one of the contributions of this thesis was to provide a detailed study and comparison between them. In a context of porous material tailoring, where large number of simulations is required, the computational cost needs to be reduced. In this way, beam models were shown to produce similar results to continuum models, with a fraction of the computational cost. On the other hand, due to the sizes of the implant, the infinite media approach may yield wrong results. Results showed that 8 unit cells may be considered as a cost-effective sample size for determining the effective mechanical behavior of the porous material. For this size, the differences between continuum and beam models stabilize and the results for the finite media approach are close to those obtained with an infinite media.

In the second part of this thesis, it was revealed that because of the sizes to be produced compared to the accuracy of the additive manufacturing process, the porous materials show irregularities in the form of inclined struts, strut diameter variation and, in some cases, broken struts. It was shown that the presence of these manufacturing irregularities may

explain the large differences between experimental and numerical results obtained with idealized computational models of the porous material. In this way, by using a simple characterization of manufacturing irregularities and including them in a beam FE model, the correspondence between numerical results and experimental data was greatly improved. These results have motivated an additional line of research derived from the present thesis that aims at developing a methodology for the more precise characterization of the irregularities present in additively manufactured porous materials. This has resulted in another publication by Vanderesse et al (2016).

The third part of this thesis was focused on the optimization of functionally graded hip stems in order to decrease the effects of stress shielding and critical interfacial stresses. In the literature, authors had followed two separate approaches: 1) optimize the shape of the implant and 2) optimize the functional gradation of the mechanical properties of the implant. Nowadays, additive manufacturing allows for the production of implants having both, optimized shape and functional gradation of their mechanical properties. This thesis showed that it is possible to ameliorate the stress shielding and the distribution of interfacial stresses by considering hip stems that combine an optimized shape with a functional gradation of mechanical properties. To this end, in the proposed approach the optimization of the stem was done separately from the tailoring of the porous material, allowing for changes in this latter stage without affecting the results from the former. The finite size beam model having 8 unit cells as developed in the first part of the thesis was considered. Furthermore, the manufacturing irregularities of porous materials were taken into account, resulting in predictions for the mechanical behavior that are close to the experimental data.

As a conclusion, the present thesis has established essential bases in terms of the FE simulation of porous materials taking into account the manufacturing irregularities and for the optimization of a new hip implant generation with optimized shape and functional gradation of material properties, produced by additive manufacturing technologies.

APPENDIX I

EXPERIMENTAL TESTS OF POROUS MATERIALS

Table AI.1 Mechanical properties of experimental testing of porous materials

Author	Test	Unit cell	ϕ_S (mm)	ϕ_P (mm)	L_{UC} (mm)	$P\%$	ρ_{rel}	$\frac{L_{UC}}{\phi_S}$	E_{ap} (GPa)	$S_{Y,ap}$ (MPa)	S_{max} (MPa)	
Ahmadi et al. (2014)	Comp	D	-	-	-	-	0.105 - 0.36	$\frac{1.67}{5}$	$\frac{0.37}{4.24}$	$\frac{8.2}{99.64}$	-	
Cansizoglu et al. (2008)	Comp	D	0.7*	-	4 - 6*	-	0.053 - 0.112	-	0.026 - 0.211	-	2.21 - 8.78	
	3PB						0.032 - 0.071		0.061 - 0.337		-	
Cheng et al. (2012)	Comp	DO	0.72 - 1.08	1.24 - 3.13	-	62.08 - 86	0.14 - 0.38	-	$\frac{0.54}{6.34}$	-	$\frac{12.4}{112.8}$	
Harrysson et al. (2008)	Comp (par)	DO	0.7*	-	3 - 12*	-	0.04 - 0.41*	-	0.012 - 0.06	-	0.82 - 91.3	
	Comp (per)				3 - 10*		0.05 - 0.41*		0.023 - 0.079		0.85 - 94.9	
	3PB				3 - 8*		0.073 - 0.4*		0.047 - 12.8		-	
Heinl et al. (2008b)	Comp (par)	SC	-	0.45	-	59.5	-	-	12.9 ± 0.9	107.5 ± 3.6	148.4 ± 3.5	
	Comp (per)								3.9 ± 2.1	49.6 ± 20.6	127.1 ± 29.2	
	Comp (par)	D		1.23					81.1	1.6 ± 0.3	22 ± 1.1	29.3 ± 0.8
	Comp (per)								80.8	0.9 ± 0.1	16.1 ± 0.4	21 ± 0.7

Note: 3PB/4PB: 3/4 point-bending, **Comp:** compression, **D:** diamond, **DO:** dodecahedron, **DT:** dode-thin, **GY:** gyroid, **HC:** honeycomb, **par:** parallel to manufacturing direction, **per:** perpendicular to manufacturing direction, **SC:** simple cubic. Theoretical or design values indicated by *

Table AI.1 Mechanical properties of experimental testing of porous materials (Cont)

Author	Test	Unit cell	ϕ_S (mm)	ϕ_P (mm)	L_{UC} (mm)	$P\%$	ρ_{rel}	$\frac{L_{UC}}{\phi_S}$	E_{ap} (GPa)	$S_{Y,ap}$ (MPa)	S_{max} (MPa)
Heinl et al. (2008)	Comp	D	0.42 - 0.54	0.67 - 1.82	0.9 - 1.5*	-	0.13 - 0.36	-	0.4 - 6.5	11.4 - 99.7	16.3 - 118.8
Herrera et al. (2014)	Comp	D	0.5-1*	-	1.5 - 4*	-		2.14 - 5.71*	0.48- 12.2	-	-
Horn et al. (2014)	4PB	D	0.454 - 2.096* (0.559 - 1.959)	-	3 - 9*	-	0.2 - 0.4* (0.114 - 0.291)	-	1.71 - 14.05	-	21.75 - 131.6
Li et al. (2009)	Comp	HC	0.5* (0.75 ± 0.036)	1.5* (1.108 ± 0.048)	-	66.3 ± 2.1	-	-	2.5 ± 0.5	73 ± 8	116 ± 10
Marin et al. (2010)	Comp	D	0.7	0.64 - 1.43	-	62 - 72.55	-	-	1 - 2.6	-	23 - 60
Murr et al. (2011)	Comp	DT	-	-	-	-	0.13 - 0.36	-	0.48 - 6.15	-	-
Parthasarathy et al. (2010, 2011)	Comp	SC	0.45 - 0.8* (0.466 - 0.941)	1 - 2.04* (0.765 - 1.96)	-	60.91 - 75.83* (49.75 - 70.32)	-	-	0.57 - 2.92	-	7.28 - 163.02
Yan et al. (2015)	Comp	D	-	0.48 - 1.45	3 - 7*	80 - 95*	0.992 - 0.996	-	0.12 - 1.25	-	-
	Comp	GY		0.56 - 1.6			0.992 - 0.995		0.13 - 1.25		

Note: 3PB/4PB: 3/4 point-bending, **Comp:** compression, **D:** diamond, **DO:** dodecahedron, **DT:** dode-thin, **GY:** gyroid, **HC:** honeycomb, **par:** parallel to manufacturing direction, **per:** perpendicular to manufacturing direction, **SC:** simple cubic. Theoretical or design values indicated by *

APPENDIX II

BRENT'S METHOD FOR ROOT FINDING

In the present thesis, the Brent's method was employed to perform the tailoring of the porous material. In that context, the variables of the method were the strut diameter, whereas the function to be evaluated was the difference between the apparent elastic modulus of the porous material and the optimized elastic modulus of the stem.

This method belongs to the bracketing techniques, which aim at finding the zero of a function within a given interval. The method is recommended for one-dimensional root finding problems where the derivative of the function is not available (Press, et al. 1992). At each iteration, the method uses three points a , b , and c , with function values f_a , f_b , and f_c , to find a new estimate of the zero of the function. These are the previous best guess, the current best guess and the opposite interval bound to b , respectively. The method then attempts an inverse quadratic interpolation and, according to some pre-established rules, it accepts the interpolation or performs a bisection. The algorithm may be summarized as (Press, et al. 1992, Scott 2013)

if a equals c , compute

$$S = f_b / f_a$$

$$P = S(c - b)$$

$$Q = 1 - S$$

else, compute

$$R = f_b / f_c; S = f_b / f_a; T = f_a / f_c$$

$$P = S[T(R - T)(c - b) - (1 - R)(b - a)]$$

$$Q = (T - 1)(R - 1)(S - 1)$$

if *cond 1* and *cond 2* and *cond 3* and adequate rate of bounds decrease, accept interpolation

$$P/Q = P/Q$$

else, bisection:

$$P/Q = (c-b)/2$$

$$b = b + P/Q$$

evaluate fb

(k-1) → interpolation (k-1) → bisection

$$\text{cond 1} \quad \left| \frac{P}{Q} \right| \geq \frac{3}{4} |c - b|$$

$$\text{cond 2} \quad \left| \frac{P}{Q} \right| < \frac{1}{2} \left| \frac{P}{Q} \right|_{k-2} \quad \left| \frac{P}{Q} \right| < \frac{1}{2} \left| \frac{P}{Q} \right|_{k-1}$$

$$\text{cond 3} \quad \left| \frac{P}{Q} \right|_{k-2} > \frac{1}{2} \text{toler} \quad \left| \frac{P}{Q} \right|_{k-1} > \frac{1}{2} \text{toler}$$

where δ is the allowed tolerance

APPENDIX III

NSGA-II GENETIC ALGORITHM, SIMULATED BINARY CROSSOVER AND POLYNOMIAL MUTATION

In the context of this thesis, the genetic algorithm NSGA-II was employed to perform the optimization of the geometry and material properties of the stem. In that context, the optimization variables were a set of 8 shape variables plus the elastic modulus at 53 material optimization points. A multiobjective optimization problem was therefore formulated where the objective functions of the bone loss and of the interfacial stresses were simultaneously minimized. Such multiobjective problem does not have a single optimal solution, but a set of “equally optimal” or “trade-off” solutions, known as the “Pareto front”. The rest of solutions are said to be dominated (i.e. they are worse in all the objective functions) by at least one Pareto solution.

Genetic algorithms belong to the heuristic optimization methods, which aim at finding an approximate of the optimum by exhaustive search of the design space. In this way, genetic algorithms allow for the determination of the Pareto front (and subsequent non-dominated fronts) of a multiobjective problem by following a natural evolution strategy. For this purpose, a population is formed by a certain number of members (i.e. stem designs), which are defined by their “chromosome”; this is the combination of values of the optimization variables. This population evolves during a given number of generations (i.e. iterations) in which new members (designs) are created from the members of the previous generation by a set of genetic operators namely: mutation and crossover. Deb et al. (2002) proposed the Non Dominated Sorting Genetic Algorithm NSGA-II, where dominating members and members that are far from others are privileged in the evolution process. The basics of this algorithm are described next.

AIII.1 The evolution process

At each generation, union of the offspring population (new members of the present generation) with the parent population (members of the previous generation) gives place to the “combined population” (double-sized population) as shown in Figure AII.1. This combined population is sorted in non-dominated fronts (F_1 to F_5 in Figure AII.1), where each successive front is dominated by at least one solution of the previous front and no solution is dominated by any of the solutions of the same front. Within each front, members are sorted according to their crowding distance. This is calculated, for each member, by a cuboid between the members with closest values for the objective functions. More information about the sorting algorithm and the crowding distance computation can be found in (Deb, et al. 2002). The new parent population is filled with the different fronts in ascending order and, if the last front is larger than there are positions in the new parent population, members are chosen according to their crowding distance (Figure AII.1).

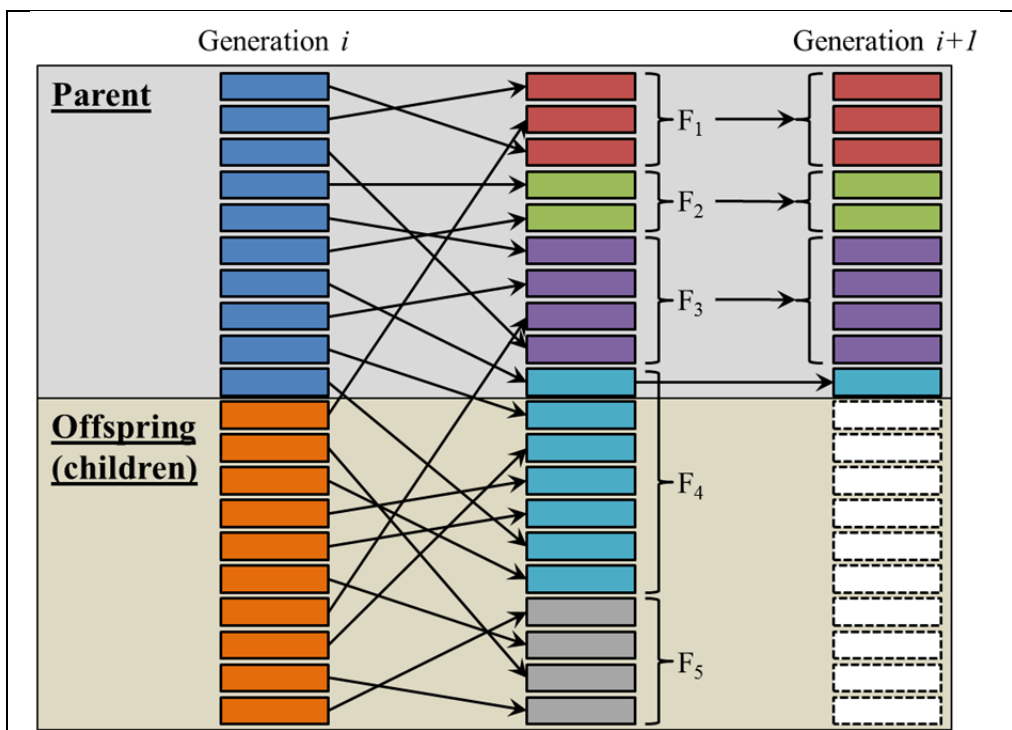


Figure AII.1 Sorting of the current population and creation of the parent population for the next generation in NSGA-II.

Adapted from (Deb, et al. 2002)

AIII.2 Tournament selection

In order to generate the new offspring population, a subset of parents is selected from the main population, creating the pool population, with smaller size. For this purpose, a common approach is to use a tournament selection, where two parents are randomly selected and compared, to select the parent with smaller non-dominated front (closer to the Pareto solution) and with higher crowding distance (i.e. from a less crowded area). Then two parents are selected randomly from the pool population and genetic operators are used to generate two children. This point is repeated until there are no more positions to fill in the offspring population

AIII.3 Genetic operators

Since in this problem real-valued variables were considered, it is necessary to use adapted genetic operators to this kind of variables. For this purpose, the simulated binary crossover (SBX) developed by (Deb and Agrawal 1995) and the polynomial mutation (PM), developed by (Deb and Goyal 1996) can be considered to replace the traditional crossover and mutation operators, respectively.

AIII.3.1 Simulated binary crossover

In real-coded genetic algorithms the children are generated from the parents by selecting a point where the binary chains that define the variable value are broken and recombined. Simulated binary crossover, as proposed by Deb and Agrawal (1995) aims at generating the real values of each variable (y) that are equivalent to those generated by a real-coded algorithm. In order to take into account given boundaries for the variable, such that $y \in [y_{low}, y_{up}]$, Deb and Agrawal (1999) proposed a modification to the original algorithm, where the first step is to compute

$$\omega = 2 - \chi^{-(\eta_c+1)}$$

With

$$\chi = 1 + \frac{(2 \cdot \min[(y_1 - y_{low}), (y_{up} - y_2)])}{(y_2 - y_1)}$$

Where η_c is the probability distribution index, which controls how far are the children from the parents (the smaller the η_c , the further the children), and y_1, y_2 are the values of the variables for the parents, being $y_2 > y_1$. Then, a random number γ is first generated with a uniform probability distribution, and the parameter β is computed according to (Deb and Agrawal, 1999)

$$\beta = \begin{cases} (2\gamma\omega)^{1/\eta_c+1} & , \text{if } \gamma \leq 1/\omega \\ \left(\frac{1}{2-\gamma\omega}\right)^{1/\eta_c+1} & \text{otherwise} \end{cases}$$

Finally, the value of the variable for each children (ch_1, ch_2) are computed as (Deb and Goyal 1996)

$$\begin{aligned} ch_1 &= 0.5[(1 + \beta)y_1 + (1 - \beta)y_2] \\ ch_2 &= 0.5[(1 - \beta)y_1 + (1 + \beta)y_2] \end{aligned}$$

AIII.3.2 Polynomial mutation

Similarly polynomial mutation aims at performing a mutation on a real-coded variable that is equivalent to the mutation that one would obtain with binary-coded variables. For this purpose, (Deb and Goyal 1996) proposed a similar approach where a random number γ is first generated with a uniform probability distribution. To take into account the boundaries of the variable, the parameter δ is computed as (Deb and Agrawal, 1999)

$$\delta = \begin{cases} [2\gamma + (1 - 2\gamma)(1 - \lambda)^{\eta_{m+1}}]^{1/\eta_{m+1}} - 1 & , \text{if } \gamma \leq 0.5 \\ 1 - [2(1 - \gamma) + 2(\gamma - 0.5)(1 - \lambda)^{\eta_{m+1}}]^{1/\eta_{m+1}} & \text{otherwise} \end{cases}$$

Where η_m is the probability distribution index for polynomial mutation, and

$$\lambda = \frac{\min[(y - y_{low}), (y_{up} - y)]}{(y_{up} - y_{low})}$$

Then, the mutated value for the children (ch) is computed from the parent as (Deb and Agrawal, 1999)

$$ch = y + \delta(y_{up} - y_{low})$$

LIST OF REFERENCES

- Adjari, A., H. Nayeb-Hashemi, P. Canavan and G. Warner, 2008. "Effect of defects on elastic-plastic behavior of cellular materials". *Materials Science and Engineering A*, vol. 487, n° 1-2, p. 558-567.
- Ahmadi, S. M., G. Campoli, S. Amin Yavari, B. Sajadi, R. Wauthle, J. Schrooten, H. Weinans, A. A. Zadpoor, 2014. "Mechanical behavior of regular open-cell porous biomaterials made of diamond lattice unit cells". *Journal of the Mechanical Behavior of Biomedical Materials*, vol. 34, p. 106-115.
- Alkhader, M., and M. Vural, 2008. "Mechanical response of cellular solids: Role of cellular topology and microstructural irregularity". *International Journal of Engineering Science*, vol. 46, n° 10, p. 1035-1051.
- Amin Yavari, S., R. Wauthle, J. van der Stok, A. A. Zadpoor, 2013. "Fatigue behavior of porous biomaterials manufactured using selective laser melting". *Materials Science and Engineering C*, vol. 33, n° 8, p. 4849-4858.
- Amin Yavari, S., S. M. Ahmadi, R. Wauthle, B. Pouran, J. Schrooten, H. Weinans, A. A. Zadpoor, 2015. "Relationship between unit cell type and porosity and the fatigue behavior of selective laser melted meta-biomaterials". *Journal of the Mechanical Behavior of Biomedical Materials*, vol. 43, p. 91-100.
- Arabnejad Khanoki, S. and D. Pasini, 2012. "Multiscale design and multiobjective optimization of orthopedic hip implants with functionally graded cellular material". *Journal of Biomechanical Engineering*, vol. 134, n° 3, 10 p.
- Arabnejad Khanoki, S., and D. Pasini, 2013. "Mechanical properties of lattice materials via asymptotic homogenization and comparison with alternative homogenization methods". *International Journal of Mechanical Sciences*, Issue 77, p. 249-262.
- Arabnejad Khanoki, S., and D. Pasini, 2013b. "The fatigue design of a bone preserving hip implant with functionally graded cellular material". *Journal of Medical Devices*, vol. 7, n° 2, ID 020907, 2 p.
- Arabnejad Khanoki, S. and D. Pasini, 2013c. "Fatigue design of a mechanically biocompatible lattice for a proof-of-concept femoral stem". *Journal of the Mechanical Behavior of Biomedical Materials*, vol. 22, p. 65-83.
- ARCAM AB, n.d. "A1 brochure". Available at: <http://www.arcam.com/wp-content/uploads/Arcam-A1.pdf>. Accessed March 2, 2016. Mölndal: ARCAM.

- ARCAM AB, n.d. “Q10 brochure”. Available at: <http://www.arcam.com/wp-content/uploads/Arcam-Q10.pdf>. Accessed March 2, 2016. Mölndal: ARCAM.
- ARCAM AB, n.d. “Ti6Al4V ELI Titanium Alloy brochure”. Available at: <http://www.arcam.com/wp-content/uploads/Arcam-Ti6Al4V-ELI-Titanium-Alloy.pdf>. Accessed March 2, 2016. Mölndal: ARCAM.
- Ashby, M. F., 2006. “The properties of foams and lattices”. *Philosophical Transactions of the Royal Society A*, vol. 364, n° 1838, p. 15-30.
- Babaei, S., B. H. Jahromi, A. Adjari, H. Nayeb-Hashemi, A. Vaziri, 2012. “Mechanical properties of open-cell rhombic dodecahedron cellular structures”. *Acta Materialia*, vol. 60, n° 6-7, p. 2873-2885.
- Barraud, A., 2015. “Évaluation des nouvelles technologies de fabrication additive dans le développement d’implants orthopédiques”. MSc Thesis, Montréal, École de technologie supérieure, 105 p.
- Barbas, A., A. A. Bonnet, P. Lipinski, R. Peci, G. Dubois, 2012. “Development and mechanical characterization of porous titanium bone substitutes”. *Journal of the Mechanical Behavior of Biomedical Materials*, vol. 9, p. 34-44.
- Bergmann, G., G. Deuretzbacher, M. Heller, F. Graichen, A. Rohlmann, J. Strauss, G. N. Duda, 2001. “Hip contact forces and gait patterns from routine activities”. *Journal of Biomechanics*, vol. 34, n° 7, p. 859-871.
- Berry, D. J., and K. J. Bozic, 2010. “Current practice patterns in primary hip and knee arthroplasty among members of the American Association of Hip and Knee Surgeons”. *The Journal of Arthroplasty*, vol. 25, n° 6 (Suppl.1), p. 2-4.
- Campoli, G., M. S. Borleffs, S. Amin Yavari, R. Wauthle, H. Weinans, A. A. Zadpoor, 2013. “Mechanical properties of open-cell metallic biomaterials manufactured using additive manufacturing”. *Materials and Design*, vol. 49, p. 957-965.
- Canadian Institute for Health Information, 2015. *Hip and Knee Replacements in Canada: Canadian Joint Replacement Registry 2015 Annual Report*. Ottawa: CIHI, 63 p.
- Cansizoglu, O., O. Harrysson, D. Cormier, H. West, T. Mahale, 2008. “Properties of Ti-6Al-4V non-stochastic lattice structures fabricated via electron beam melting”. *Materials Science and Engineering A*, vol. 492, n° 1-2, p. 468-474.
- Carter, D. and W. C. Hayes, 1977. “The compressive behavior of bone as a two-phase porous structure”. *Journal of Bone and Joint Surgery*, 59, n° 7, p. 954-962.

- Chanda, S., S. Gupta, and D. K. Pratihari, 2015. "A genetic algorithm based multi-objective shape optimization scheme for cementless femoral implant". *Journal of Biomechanical Engineering*, vol. 137, n° 3, ID 034502, 12 p.
- Chen, C., T. J. Lu, and N. A. Fleck, 1999. "Effect of imperfections on the yielding of two-dimensional foams". *Journal of the Mechanics and Physics of Solids*, vol. 47, n° 11, p. 2235-2272.
- Cheng, X., S. J. Li, L. E. Murr, Z. B. Zhang, Y. L. Hao, R. Yang, F. Medina, R. B. Wicker, 2012. "Compression deformation behavior of Ti-6Al-4V alloy with cellular structures fabricated by electron beam melting". *Journal of the Mechanical Behavior of Biomedical Materials*, vol. 16, p. 153-162.
- Coelho, P. G., L. D. Amiano, J. M. Guedes, and H. C. Rodrigues, 2015. "Scale-size effects analysis of optimal periodic material microstructures designed by the inverse homogenization method". *Computers and Structures*, in Press.
- Currey, J. D., 2002. *Bones. Structure and Mechanics*. 2nd ed. New Jersey: Princeton University Press, 436 p.
- Dai, G., and W. Zhang, 2009. "Size effects of effective Young's modulus for periodic cellular materials". *Science in China Series G: Physics, Mechanics & Astronomy*, vol. 52, n° 8, p. 1262-1270.
- Deb, K., A. Pratap, S. Agarwal, and T. Meyarivan, 2002. "A fast and elitist multiobjective genetic algorithm: NSGA-II". *IEEE Transactions on Evolutionary Computation*, vol. 6, n° 2, p. 182-198.
- Deb, K., and M Goyal, 1996. "A combined genetic adaptive search (GeneAS) for engineering design". *Computer Science and Informatics*, vol. 26, p. 30-45.
- Deb, K., and S. Agrawal, 1995. "Simulated binary crossover for continuous search space". *Complex Systems*, vol. 9, p. 115-148.
- Deb, K., and S. Agrawal, 1999. "A niched-penalty approach for constraint handling in genetic algorithms". In *Artificial Neural Nets and Genetic Algorithms*, Dobnikar, A., N. C. Steele, D. W. Pearson, and R. F. Albrecht, (Eds.), p.235-243. Wien: Springer-Verlag
- Delaunay, C. P., F. Bonnomet, P. Clavert, P. Laffargue, H. Migaud, 2008. "THA Using Metal-on-Metal articulation in active patients younger than 50 years". *Clinical Orthopaedics and Related Research*, vol. 466, n° 2, p. 340-346.

- El Ghezal, M. I., Y. Maalej, and I. Doghri, 2013. "Micromechanical models for porous and cellular materials in linear elasticity and viscoelasticity". *Computational Materials Science*, vol. 70, p. 51-70.
- EOS, n.d. "EOSINT M270 brochure". Available at: http://dmlstechnology.com/images/pdf/EOSINT_M_270.pdf, Accessed March 2, 2016. Munich: EOS.
- EOS, n.d. "Titanium Ti64ELI brochure". Available at: https://scrivito-public-cdn.s3-eu-west-1.amazonaws.com/eos/fe8d0271508e1e03/d6e4d305e880/EOS_Titanium_Ti64_en.pdf. Accessed March 2, 2016. Munich: EOS.
- Evert Smith, 2007-2008. "Innovations in total hip replacement". Retrieved from <http://evertsmith.com/innovations/>. Accessed February 25, 2016.
- Fernandes, P. R., J. Folgado, and R. B. Ruben, 2004. "Shape optimization of a cementless hip stem for a minimum of interface stress and displacement". *Computer Methods in Biomechanics and Biomedical Engineering*, vol. 7, n° 1, p. 51-61.
- Fraldi, M., L. Esposito, G. Perrella, A. Cutolo, S. C. Cowin, 2010. "Topological optimization in hip prosthesis design". *Biomechanics and Modeling in Mechanobiology*, vol. 9, n° 4, p. 389-402.
- García, J. M., M. Doblaré, and J. Cegoñino, 2002. "Bone remodelling simulation: a tool for implant design". *Computational Materials Science*, vol. 25, n° 1-2, p. 100-114.
- Gibson, L. J., 2005. "Biomechanics of cellular solids". *Journal of Biomechanics*, vol. 38, n° 3, p. 377-399.
- Gibson, L. J., and M. F. Ashby, 1999. *Cellular Solids: Structure and Properties*. 2nd ed. Cambridge, United Kingdom: Cambridge University Press, 532 p.
- Gümrük, R., and R. W. Mines, 2013. "Compressive behaviour of stainless steel micro-lattice structures". *International Journal of Mechanical Sciences*, vol. 68, p. 125-139.
- Harrigan, J., S. Reida, and S. Yaghoubib, 2010. "The correct analysis of shocks in a cellular material". *International Journal of Impact Engineering*, vol. 37, n° 8, p. 918-927.
- Harrysson, O. L., O. Cansizoglu, D. J. Marcellin-Little, D. R. Cormier, H. A. West II, 2008. "Direct metal fabrication of titanium implants with tailored materials and mechanical properties using electron beam melting technology". *Materials Science and Engineering C*, vol. 28, n° 3, p. 366-373.

- Hazlehurst, K. B., C. J. Wang, and M. Stanford, 2014. "A numerical investigation into the influence of the properties of cobalt chrome cellular structures on the load transfer to the periprosthetic femur following total hip arthroplasty". *Medical Engineering and Physics*, vol. 36, n° 4, p. 458-466.
- Hazlehurst, K. B., C. J. Wang, and M. Stanford, 2013. "Evaluation of the stiffness characteristics of square pore CoCrMo cellular structures manufactured using laser melting technology for potential orthopaedic applications". *Materials and Design*, vol. 51, p. 949-955.
- Hedia, H. S., M. A. Shabara, T. T. El-Midany, and N. Fouda, 2006. "Improved design of cementless hip stems using two-dimensional functionally graded materials". *Journal of Biomedical Materials B: Applied Biomaterials*, vol. 79, n° 1, p. 42-49.
- Heinl, P., A. Rottmair, C. Körner, and R. F. Singer, 2007. "Cellular titanium by selective electron beam melting". *Advanced Engineering Materials*, vol. 9, n° 5, p. 360-364.
- Heinl, P., C. Körner, and R. F. Singer, 2008. "Selective electron beam melting of cellular titanium: mechanical properties". *Advanced Engineering Materials*, vol. 10, n° 9, p. 882-888.
- Heinl, P., L. Müller, C. Körner, R. F. Singer, F. A. Müller, 2008b. "Cellular Ti-6Al-4V structures with interconnected macro porosity for bone implants fabricated by selective electron beam melting". *Acta Biomaterialia*, vol. 4, n° 5, p. 1536-1544.
- Heller, M. O., G. Bergmann, J. P. Kassi, L. Claes, N. P. Haas, G. N. Duda, 2005. "Determination of muscle loading at the hip joint for use in pre-clinical testing". *Journal of Biomechanics*, vol. 38, n° 5, p. 1155-1163.
- Heo, H., J. Ju, D. M. Kim, 2013. "Compliant cellular structures: Application to a passive morphing airfoil". *Composite Structures*, vol. 106, p. 560-569.
- Herrera, A., A. Yáñez, O. Martel, H. Afonso, D. Monopoli, 2014. "Computational study and experimental validation of porous structures fabricated by electron beam melting: A challenge to avoid stress shielding". *Materials Science and Engineering C*, vol. 45, n° 1, p. 89-93.
- Horn, T. J., O. L. A. Harrysson, D. J. Marcellin-Little, H. A. West, B. Duncan, X. Lascelles, R. Aman, 2014. "Flexural properties of Ti6Al4V rhombic dodecahedron open cellular structures fabricated with electron beam melting". *Additive Manufacturing*, vol. 1-4, p. 2-11.
- Hrabe, N. W., P. Heinl, B. Flinn, C. Körner, R. K. Bordia, 2011. "Compression-compression fatigue of selective electron beam melted cellular titanium (Ti-6Al-4V)". *Journal of Biomedical Materials Research B: Applied Biomaterials*, vol. 99, n° 2, p. 313-320.

- Huiskes, R., H. Weinans, H. J. Grootenboer, M. Dalstra, B. Fudala, T. J. Slooff, 1987. "Adaptive bone-remodeling theory applied to prosthetic-design analysis". *Journal of Biomechanics*, vol. 20, n° 11-12, p. 1135-1150.
- Huiskes, R., H. Weinans, and B. Van Rietbergen, 1992. "The Relationship Between Stress Shielding and Bone Resorption Around Total Hip stems and the Effects of Flexible Materials". *Clinical Orthopaedics and related Research*, vol. 274, p. 124-134.
- Huiskes, R., and R. Boeklagen, 1988. "The application of numerical shape optimization to artificial-joint design". *Computational Methods in Bioengineering*, vol. 9, p. 185-197.
- Huiskes, R., and R. Boeklagen, 1989. "Mathematical shape optimization of hip prosthesis design". *Journal of Biomechanics*, vol. 22, n° 8-9, p. 793-804.
- Kaplan, S. J., W. C. Hayes, J. L. Stone, and G. S. Beaupré, 1985. "Tensile strength of bovine trabecular bone". *Journal of Biomechanics*, vol. 18, n° 9, p. 723-727.
- Karamooz Ravari, M., and M. Kadkhodaei, 2015. "A computationally efficient modeling approach for predicting mechanical behavior of cellular lattice structures". *Journal of Materials Engineering and Performance*, vol. 24, n° 1, p. 245-252.
- Katoozian, H., and D. T. Davy, 2000. "Effects of loading conditions and objective function on three-dimensional shape optimization of femoral components of hip endoprostheses". *Medical Engineering and Physics*, vol. 22, n° 4, p. 243-251.
- Keller, T. S., 1994. "Predicting the compressive mechanical behavior of bone". *Journal of Biomechanics*, vol. 27, n° 9, p. 1159-1168.
- Keyak, J. H., and Y. Falkinstein, 2003. "Comparison of in situ and in vitro CT scan-based finite element model predictions of proximal femoral fracture load". *Medical Engineering and Physics*, vol. 25, n° 9, p. 781-787.
- Khanuja, H. S., J. J. Vakil, M. S. Goddard, and M. A. Mont, 2011. "Cementless femoral fixation in total hip arthroplasty". *Journal of Bone and Joint Surgery*, vol. 93, p. 500-509.
- Koike, M., P. Greer, K. Owen, G. Lilly, L. E. Murr, S. M. Gaytan, E. Martinez, T. Okabe, 2011. "Evaluation of titanium alloys fabricated using rapid prototyping technologies - electron beam melting and laser beam melting". *Materials*, vol. 4, n° 10, p. 1776-1792.
- Kouznetsova, V. G., 2002. "Computational homogenization for the multi-scale analysis of multi-phase materials". Thesis dissertation, Eindhoven, TU Eindhoven, 120p.
- Kowalczyk, P., 2001. "Design optimization of cementless femoral hip prostheses using finite element analysis". *Journal of Biomechanical Engineering*, vol. 123, n° 5, p. 396-402.

- Kuiper, J. H., and R. Huiskes, 1992. "Numerical optimization of hip-prosthetic stem material". In *Recent Advances in Computer Methods in Biomechanics and Biomedical Engineering*, Middleton, J., G. N. Pande, and K. R. Williams (Eds.), p. 76-84. Swansea: Books and Journals International.
- Kuiper, J. H., and R. Huiskes, 1997. "Mathematical optimization of elastic properties: application to cementless hip stem design". *Journal of Biomechanical Engineering*, vol. 119, n° 2, p. 166-174.
- Kumar, V., G. Manogharan, and D. R. Cormier, 2009. "Design of periodic cellular structures for heat exchanger applications". In *Solid Freeform Fabrication Symposium Proceedings* (Texas, Aug. 3-5 2009), p. 738-748.
- Kurtz, S. M. et al., 2009. "Future young patient demand for primary and revision joint replacement: national projections from 2010 to 2030". *Clinical Orthopaedic and Related Research*, vol. 467, n° 10, p. 2606-2612.
- Learmonth, I. D., C. Young, and C. Rorabeck, 2007. "The operation of the century: total hip replacement". *Lancet*, vol. 370, n° 9597, p. 1508-1519.
- Li, X., C. Wang, W. Zhang, and Y. Li, 2009. "Fabrication and characterization of porous Ti6Al4V parts for biomedical applications using electron beam melting process". *Materials Letters*, vol. 63, n° 3-4, p. 403-405.
- Luxner, M. H., A. Woesz, J. Stampfl, P. Fratzl, H. E. Pettermann, 2009. "A finite element study on the effects of disorder in cellular structures". *Acta Biomaterialia*, vol. 5, n° 1, p. 381-390.
- Luxner, M., and H. E. Pettermann, 2009. "Modeling and simulation of highly porous open cell structures: elasto-plasticity and localization versus disorder and defects". In *Proceedings of the IUTAM Symposium on Mechanical Properties of Cellular Materials*. (Cachan, Sept. 17-20 2007), p. 125-134. Springer Science and Business Media.
- Luxner, M. H., J. Stampfl, and H. E. Pettermann, 2005. "Finite element modeling concepts and linear analyses of 3D regular open cell structures". *Journal of Materials Science*, vol. 40, n° 22, p. 5859-5866.
- Luxner, M. H., J. Stampfl, and H. E. Pettermann, 2007. "Numerical simulations of 3D open cell structures - influence of structural irregularities on elasto-plasticity and deformation localization". *International Journal of Solids and Structures*, vol. 44, n° 9, p. 2990-3003.

- Luxner, M. H., J. Stampfl, and H. E. Pettermann, 2009. "Nonlinear simulations on the interaction of disorder and defects in open cell structures". *Computational Material Science*, vol. 47, n° 2, p. 418-428.
- Maalej, Y., M. I. El Ghezal, and I. Doghri, 2013. "Micromechanical approach for the behaviour of open cell foams". *European Journal of Computational Mechanics*, vol. 22, n° 2-4, p. 198-208.
- Mai, K. T., C. A. Verioti, K. Casey, Y. Slesarenko, L. Romeo, C. W. Colwell Jr., 2010. "Cementless femoral fixation in total hip arthroplasty". *The American Journal of Orthopedics*, vol. 39, n° 3, p. 126-130.
- Maloney, K. J., K. D. Fink, T. A. Schaedler, J. A. Kolodziejska, A. J. Jacobsen, C. S. Roper, 2012. "Multifunctional heat exchangers derived from three-dimensional micro-lattice structures". *International Journal of Heat and Mass Transfer*, vol. 55, n° 9-10, p. 2486-2493.
- Marieb, E. N., 1999. *Anatomie et Physiologie Humaines*. 2nd ed. version française. The Benjamin-Cummings Publishing Company, Inc.
- Marin, E., S. Fusi, M. Pressacco, L. Paussa, L. Fedrizzi, 2010. "Characterization of cellular solids in Ti6Al4V for orthopaedic implant applications: trabecular titanium". *Journal of the Mechanical Behavior of Biomedical Materials*, vol. 3, n° 5, p. 373-381.
- Murr, L., K. N. Amato, S. J. Li, Y. X. Tian, X. Y. Cheng, S. M. Gaytan, E. Martinez, P. W. Shindo, F. Medina, R. B. Wicker, 2011. "Microstructure and mechanical properties of open-cellular biomaterials prototypes for total knee replacement implants fabricated by electron beam melting". *Journal of the Mechanical Behavior of Biomedical Materials*, vol. 4, n° 7, p. 1396-1411.
- Murr, L. E., S. M. Gaytan, E. Martinez, F. Medina, R. B. Wicker, 2012. "Next generation orthopaedic implants by additive manufacturing using electron beam melting". *International Journal of Biomaterials*, vol. 2012, ID 245727, p. 1-14.
- Onck, P. R., E. W. Andrews, and L. J. Gibson, 2001. "Size effects in ductile cellular solids. Part I: modeling". *International Journal of Mechanical Sciences*, vol. 43, n° 3, p. 681-699.
- Pal, B., S. Gupta, and A. M. New, 2009. "A numerical study of failure mechanisms in the cemented resurfaced femur: effects of interface characteristics and bone remodeling". *Proceedings of the Institution of Mechanical Engineers H: Journal of Engineering in Medicine*, vol. 223, n° 4, p. 471-484.

- Parthasarathy, J., B. Starly, and S. Raman, 2011. "A design for the additive manufacture of functionally graded porous structures with tailored mechanical properties for biomedical applications". *Journal of Manufacturing Processes*, vol. 13, n° 2, p. 160-170.
- Parthasarathy, J., B. Starly, S. Raman, and A. Christensen, 2010. "Mechanical evaluation of porous titanium (Ti6Al4V) structures with electron beam melting (EBM)". *Journal of the Mechanical Behavior of Biomedical Materials*, vol. 3, n° 3, p. 249-259.
- Petrović, V., J. R. Blasco, L. Portolés, I. Morales, V. Primo, C. Atienza, V. Belloch, 2012. "A study of mechanical and biological behavior of porous Ti6Al4V fabricated on EBM". In *Innovative Developments in Virtual and Physical Prototyping*, Bártolo, P. J., A. C. Soares de Lemos, A. P. Oliveira Tojeira, A. M. Henriques Pereira, A. J. Matheus, A. L. Avelar Mendes, C. dos Santos, D. M. Fernandes Freitas, H. M. Bártolo, H. de Amorim Almeida, I. Marques dos Reis, J. R. Dias, M. A. Neves Domingos, N. M. Fernandes Alves, R. F. Brás Pereira, T. M. Fernandes Patricio, T. M. Dias Ferreira (Eds.), p. 115-120. London: Taylor and Francis Group.
- Pivec, R., A. J. Johnson, S. C. Mears, and M. A. Mont, 2013. "Reprint of "hip arthroplasty"". *International Journal of Orthopaedic and Trauma Nursing*, vol. 17, n° 2, p. 65-78.
- Press, W. H., B. P. Flannery, S. A. Teukolsky, and W. T. Vetterling, 1992. *Numerical Recipes in Fortran 77: The Art of Scientific Computing*, 2nd Ed. New York: Cambridge University Press, 993p
- Queheillalt, D. T., and H. N. G. Wadley, 2005. "Cellular metal lattices with hollow trusses". *Acta Materialia*, vol. 53, n° 2, p. 303-313.
- Quevedo González, F. J., and N. Nuño, 2015. "Finite element modelling approaches for well-ordered porous metallic materials for orthopaedic applications: cost effectiveness and geometrical considerations". *Computer Methods in Biomechanics and Biomedical Engineering*, vol. 19, n° 8, p. 845-854.
- Quevedo González, F. J., and N. Nuño, 2016. "Finite element modeling of manufacturing irregularities of porous materials". *Biomaterials and Biomechanics in Engineering*, vol. 3, n° 1, p. 1-14.
- Quevedo González, F. J., M. Reimeringer, and N. Nuño, 2016. "On the 2D simplification of a 3D bone-femoral cementless hip stem system". *Journal of Biomechanical Engineering*, Accepted for publication: March 26th 2016.
- Rehme, O., and C. Emmelmann, 2006. "Rapid manufacturing of lattice structures with selective laser melting". In *Laser-based Micropackaging*, Bachmann, F. G., W. Hoving, L. Yongfeng, K. Washio (Eds.), p. 192-203. San Jose: SPIE Digital Library.

- Reimeringer, M., and N. Nuño, 2014. "Effect of femoral mechanical properties on primary stability of cementless total hip arthroplasty: a finite element analysis". *Advances in Biomechanics and Applications*, vol. 1, n° 3, p. 187-210.
- Reimeringer, M., N. Nuño, C. Desmarais-Trépanier, M. Lavigne, P. A. Vendittoli, 2013. "The influence of uncemented femoral stem length and design on its primary stability: a finite element analysis". *Computer Methods in Biomechanics and Biomedical Engineering*, vol. 16, n° 11, p. 1221-1231.
- Ruben, R. B., J. Folgado, and P. R. Fernandes, 2007. "Three-dimensional shape optimization of hip prostheses using a multicriteria formulation". *Structural and Multidisciplinary Optimization*, vol. 34, n° 3, p. 261-275.
- Ruben, R. B., P. R. Fernandes, and J. Folgado, 2012. "On the optimal shape of hip implants". *Journal of Biomechanics*, vol. 45, n° 2, p. 239-246.
- Scott, P., 2013. PHYS 606: *Practical numerical methods in physics and astronomy – Lecture 3: root finding*. Available at <http://www.physics.mcgill.ca/~patscott>. Montreal: McGill University. 52 p.
- Sikavitsas, V. I., J. S. Temenoff, and A. G. Mikos, 2001. "Biomaterials and bone mechanotransduction". *Biomaterials*, vol. 22, n° 19, p. 2581-2593.
- Simões, J. A. O., M. Taylor, A. T. Marques, and G. Jeronimidis, 1998. "Preliminary investigation of a novel controlled stiffness proximal femoral prosthesis". *Proceedings of the Institution of Mechanical Engineers H: Journal of Engineering in Medicine*, vol. 212, n° 3, p. 165-175.
- Siopack, J., and H. Jergesen, 1995. "Total hip arthroplasty". *Western Journal of Medicine*, vol. 162, n° 3, p. 243-249.
- Smith, M., Z. Guan, and W. J. Cantwell, 2013. "Finite element modelling of the compressive response of lattice structures manufactured using the selective laser melting technique". *International Journal of Mechanical Sciences*, vol. 67, p. 28-41.
- Spadoni, A., and M. Ruzzene, 2007. "Static Aeroelastic Response of Chiral-core Airfoils". *Journal of Intelligent Material Systems and Structures*, vol. 18, n° 10, p. 1067-1075.
- Stone, J. L., G. S. Beaupre, and W. C. Hayes, 1983. "Multiaxial strength characteristics of trabecular bone". *Journal of Biomechanics*, vol. 16, n° 9, p. 743-752.
- Swedish Hip Arthroplasty Register, 2013. *Swedish Hip Arthroplasty Register Annual Report*. Gothenburg: Swedish Hip Arthroplasty Register, 184 p.

- Tomaszewski, P. K., N. Verdonchot, S. K. Bulstra, and G. J. Verkerke, 2010. “A comparative finite-element analysis of bone failure and load transfer of osseointegrated prostheses fixations”. *Annals of Biomedical Engineering*, vol. 38, n° 7, p. 2418-2427.
- Tortora, G. D. B., 2012. *Principles of Anatomy and Physiology*. 13th Ed. Hoboken: John Wiley and Sons, Inc., 1344 p.
- UK National Joint Registry, 2015. *National Joint Registry 12th Annual Report*, Hemel Hempstead: National Joint Registry for England, Wales, Northern Ireland and the Isle of Man, 183 p.
- van der Sluis, O., P. Schreurs, W. Brekelmans, and H. Meijer, 2000. “Overall behaviour of heterogeneous elastoviscoplastic materials: effect of microstructural modelling”. *Mechanics of Materials*, vol. 32, n° 8, p. 449-462.
- Vanderesse, N., I. Ky, F. Quevedo González, N. Nuño, and P. Bocher, 2016. “Image analysis characterization of periodic porous materials produced by additive manufacturing”. *Materials and Design*, vol. 92, p. 767-778.
- Vigliotti, A., and D. Pasini, 2012. “Linear multiscale analysis and finite element validation of stretching and bending dominated lattice materials”. *Mechanics of Materials*, vol. 46, p. 57-68.
- Wang, A. J., and D. L. McDowell, 2004. “In-Plane Stiffness and Yield Strength of Periodic Metal Honeycombs”. *Journal of Engineering Materials and Technology*, vol. 126, n° 2, p. 137-156.
- Weinans, H., R. Huiskes, and H. J. Grootenboer, 1992. “Effects of material properties of femoral hip components on bone remodeling”. *Journal of Orthopaedic Research*, 10, n° 6, p. 845-853.
- Wieding, J., A. Wold, and R. Bader, 2014. “Numerical optimization of open-porous bone scaffold structure to match the elastic properties of human cortical bone”. *Journal of the Mechanical Behavior of Biomedical Materials*, vol. 37, p. 56-68.
- Willems, N. M., G. E. Langenbach, V. Everts, and A. Zentner, A., 2014. “The microstructural and biomechanical development of the condylar bone: a review”. *European Journal of Orthodontics*, vol. 36, n° 4, p. 479-485.
- Xiao, D., Y. Yang, X. Su, D. Wang, J. Sun 2013. “An integrated approach of topology optimized design and selective laser melting process for titanium implant materials”. *Bio-medical Materials and Engineering*, vol. 23, n° 5, p. 433-445.

- Yan, C., L. Hao, A. Hussein, and P. Young, 2015. "Ti-6Al-4V triply periodic minimal surface structures for bone implants fabricated via selective laser melting". *Journal of the Mechanical Behavior of Biomedical Materials*, vol. 51, p. 61-73.
- Zhu, H. X., J. R. Hobdell, and A. H. Windle, 2001. "Effects of cell irregularity on the elastic properties of 2D Voronoi honeycombs". *Journal of the Mechanics and Physics of Solids*, vol. 49, n° 4, p. 857-870.